OPERATIONAL CHARACTERISTICS OF AN ULTRA COMPACT COMBUSTOR

THESIS

Christopher J. Damele, Captain, USAF

AFIT-ENY-14-M-13

DEPARTMENT OF THE AIR FORCE
AIR UNIVERSITY

AIR FORCE INSTITUTE OF TECHNOLOGY

Wright-Patterson Air Force Base, Ohio

AFIT-ENY-14-M-13

OPERATIONAL CHARACTERISTICS OF AN ULTRA COMPACT COMBUSTOR

THESIS

Presented to the Faculty

Department of Aeronautics and Astronautics

Graduate School of Engineering and Management

Air Force Institute of Technology

Air University

Air Education and Training Command

In Partial Fulfillment of the Requirements for the

Degree of Master of Science in Aeronautical Engineering

Christopher J. Damele, BS

Captain, USAF

March 2014

AFIT-ENY-14-M-13

OPERATIONAL CHARACTERISTICS OF AN ULTRA COMPACT COMBUSTOR

Christopher J. Damele, BS

Captain, USAF

Approved:

//signed//   13 Mar 2014

_____   _____

Marc D. Polanka, PhD (Chairman)   Date

//signed//   13 Mar 2014

_____   _____

Mark F. Reeder, PhD (Member)   Date

//signed//   13 Mar 2014

_____   _____

James L. Rutledge, Maj, USAF, PhD (Member)   Date

AFIT-ENY-14-M-13

Abstract

In continuing the effort to push the limitations of modern gas turbine engines, Ultra Compact Combustors offer unique solutions to minimize engine size and weight. They accomplish this by reducing the number of components in the engine core and perform the combustion in a circumferential cavity that encircles the core flow. Within this cavity, the fuel is injected rich. Burning continues to occur in the vane passage beneath the circumferential cavity which must be completed in a controlled manner prior to the inlet plane of the turbine rotor. Furthermore, the temperature distribution at the exit of the vane passage must be controlled to generate high work extraction from the turbine. This research shall vary the cavity equivalence ratio, g-loading, bulk flow rate, and mass flow ratio with the core flow to characterize the impact of each of these parameters on the exit conditions. The primary metrics for comparison are the exit temperature and pressure profiles, the emissions characteristics, and the overall system losses. Overall, the goal of this research effort was to establish a set of criteria that produced an exit flow condition similar to that created by a traditional axial combustion system, thus realizing the weight savings offered by the ultra compact design. Results will show the shapes and magnitudes of the exit temperature and pressure profiles, quantify the emissions species across the exit plane, and establish a benchmark for the overall system losses as a function of the cavity parameters.

Acknowledgments

Table of Contents

List of Figures

Nomenclature

AFRL = Air Force Research Lab

AFIT = Air Force Institute of Technology

F_B = Buoyant forces

CCW = Counter-clockwise cavity swirl direction

CFD = Computational Fluid Dynamics

COAL = Combustion Optimization and Analysis Laser

CW = Clockwise cavity swirl direction

EGV = Exit guide vanes (compressor)

FT = Fischer-Tropsch (fuel)

G = Gravitational load

g_c = 9.8 m/s^2, Gravitational constant for Earth

HSV = High speed video

ID = Inner diameter

IGV = Inlet guide vanes (turbine)

ITB = Inter Turbine Burner

LBO = Lean Blow Out

LLCB = Low Loss centerbody

M = Mach number

MFC = Mass flow controller

MFR = Mass flow ratio (between the cavity and core)

OD = Outer diameter

R = Radius

RNG = Renormalization Group method

RVC = Radial vane cavity

T = Temperature

TCB = Tapered center body

TSFC = Thrust Specific Fuel Consupmtion

UCC = Ultra Compact Combustor

V_{tan} = Tangential velocity

$\theta_{pattern}$= Temperature pattern factor

$\theta_{profile}$= Temperature profile factor

$\Phi_{pattern}$= Pressure pattern factor

$\Phi_{profile}$= Pressure profile factor

$$\varphi_{cav} = \frac{\left(\dot{m}_{air}/\dot{m}_{fuel}\right)_{stoich}}{\left(\dot{m}_{air}/\dot{m}_{fuel}\right)_{cav}} \text{ , Cavity equivalence ratio}$$

$$\varphi_{UCC} = \frac{\left(\dot{m}_{air}/\dot{m}_{fuel}\right)_{stoich}}{\left(\dot{m}_{air}/\dot{m}_{fuel}\right)_{UCC}} \text{ , UCC equivalence ratio}$$

γ = $\frac{c_p}{c_v}$, Ratio of specific heats

I. Introduction

At its core, the fundamental purpose of the jet engine combustor is heat release and the conversion of thermal energy into mechanical energy. The exothermic reaction that occurs with the break-up of fuel based hydrocarbons describes this heat release. The channeling of this release into an ingested volume of air increases the thermal energy of that air volume which is then converted into mechanical energy via the engine turbine section. Good combustor design is a balancing act between promoting the complete combustion of fuel, minimizing axial total pressure loss, the stability of good combustion processes, proper temperature and pressure distributions at the exit plane, and adherence to common environmental standards and regulations [1].

The thermal environment is of key importance to allow a fuel/air mixture to burn to completion. This involves supplying the proper amount of activation energy to maintain the reactions involved with the breakdown of hydrocarbon bonds. Without this necessary activation energy, the reactions are quenched and the breakdown of hydrocarbons can no longer proceed. A minimal degree of total pressure loss is necessary to drive the flow through the combustor section. An unfavorable pressure gradient generated at the combustor exit may force hot combustion gas to stay resident in the combustor and discourage the translation of thermal energy into mechanical energy as hot gas passes through the turbine section. A stable combustion process describes the balancing of the right fuel/air mixture so as to prevent a combustor flame out. This involves supplying both fuel in air via the correct mass flow rates, pressures and temperatures. The exiting thermal and pressure profile shapes must be optimized to warrant the maximum transfer of thermal to mechanical energy. The flow of hot gas over

turbine blades creates powerful moments that induce the spinning of turbine rotors which provide the necessary shaft torque to spin the engine's compressor rotors. If these hot gas streams are not placed correctly, the survivability of key components becomes of issue. Lastly, the adherence to common environmental standards and regulations pushes combustor designs to the limit. The chemical mechanisms for the production of combustion byproducts such as CO_2 and NO_x require specific activation energies. The control and implementation of cooling schemes and recirculation zones within the combustor control the formation of hot spots that support these activation energies.

Traditional axial combustors maintain two independent streams of air as shown in Figure 1.1. The primary air is generally one half of the total combustor air volume and is determined by the air mass needed to balance the correct fuel/air mixture necessary for combustion to occur. Secondary air is used for a variety of functions, mainly as a cooling source to prevent the combustor wall from forming hot spots [2].
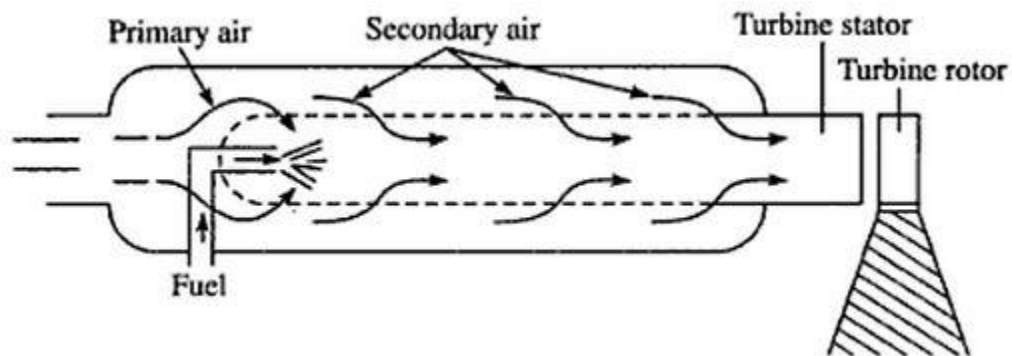
Figure 1.1. Axial length combustor system [2].

Today's high thrust producing engines require significantly larger turbine inlet temperatures ($T_{t,4}$) which drive the need for high strength nickel-alloy and matrix

composite turbine blade designs to withstand the harsh thermal environment. These high strength materials increase costs and depend upon quality combustor designs to deliver uniform thermal and pressure profiles so as to increase their rate of survival. Turbine blades utilize film cooling techniques to form protective barriers against unwanted hot spots generated from non-uniformities in combustor exit flow. To mitigate the effect of these hot spots, conventional axial combustors are designed to burn fuel lean and prevent the continuation of burning downstream of the combustor section. A significant axial length is required to completely house the lean combustion process. This axial length increases the combustor weight and is a detriment to the aircraft's overall thrust to weight ratio. Any aircraft weight savings cause immediate improvements in thrust to weight ratios. A combustor design that alleviates the weight and length requirements necessary for complete combustion would offer significant benefits to an aircraft's overall performance.

1.1   Ultra Compact Combustor

As an alternative to the traditional axial length combustor, the Air Force Research Laboratory (AFRL) and the Air Force Institute of Technology (AFIT) have modeled, built and tested Ultra Compact Combustor (UCC) designs. The advent of the UCC is rooted in the desire to build a combustor system that limits the weight and length of the combustor section by housing the combustion process in a circumferential cavity that encompasses the axial flow path of a jet engine. By inducing a g-load (centripetal acceleration) within the circumferential cavity, heavier unburned fuel/air mixtures are forced to stay resident within the cavity. As the fuel/air is burned, the lighter combustion

products are forced out of the cavity due to buoyancy effects. Because the combustion process occurs in the plane perpendicular to the ingested air stream, the combustor length is significantly reduced.

Savings in weight, in addition to the decreased combustor length, are realized in the reduction of turbomachinery components needed to slow, turn, and accelerate the axial flow. The UCC boasts the ability to perform the functions of a compressor exit guide vane (EGV) and a turbine inlet guide vane (IGV). The EGV and IGV are traditionally needed to straighten the flow exiting the engine compressor and passing to the combustor then turn the flow so that it may be passed onto turbine rotor blades while exiting the combustor. Within the UCC application, a hybrid vane performs the tasks of both components and allows for weight savings of approximately 66% [3].

Figure 1.2 mirrors a conventional engine design with an axial length combustor against a UCC implemented engine. The goal of UCC implementation is to make a seamless transition between combustor types allowing the engine turbine section to remain blind in regards to where high thermal energy flow is generated.
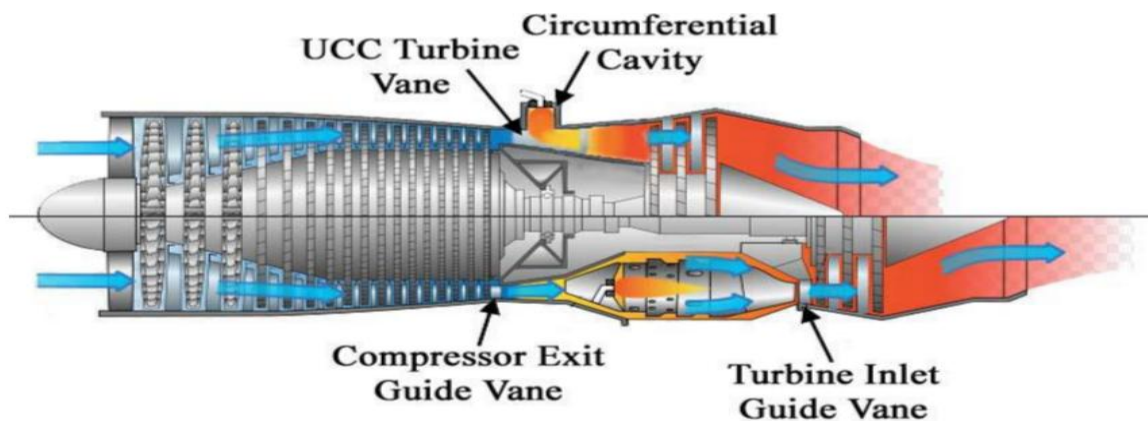
Figure 1.2. Conventional jet engine with axial length combustor mirrored against an UCC [4].

4

1.2   UCC Test Rig

The work done at both AFRL and AFIT has contributed greatly to the understanding of combustion in a swirling circumferential cavity. At its beginning, research was focused on only sectional models at AFIT to understand the migration of flame fronts about an annulus. Over time, the research required full-annular models to better understand the entrainment of hot combustion products into larger core axial flows.

At AFIT, Wilson [5] designed, built, and tested the Institute's first full-annular UCC. The UCC was extremely modular in design allowing for the implementation of different temperature and pressure instrumentation configurations, optical cavity access for capturing high speed video (HSV), independent controls for core and cavity flows, and interchangeable hardware pieces for inducing different cavity swirl directions and magnitudes. Between the interchangeable hardware and multiple methods for capturing the UCC's operational performance, the AFIT UCC is suited for the study of multiple research objectives aimed at the eventual integration of a UCC into full-scale jet engines.

1.3   Research Objectives

In continuing to understand the AFIT UCC's full operational capabilities and performance in hopes of creating a seamless transition from axial length combustor to UCC, three main research objectives were outlined for this effort. The objectives are primarily based on the identification and characterization of the AFIT UCC's performance with secondary objectives involving the optimization of those performance factors.

The first research objective was to understand the factors that impact the thermal and pressure exit profiles of the AFIT UCC. It is imperative to the application of the UCC to be able to accept the flow conditions emanating from the compressor and deliver a flow to the turbine consistent with an axial combustor. These profiles contribute greatly to the overall engine performance and this objective aims to establish the benchmark for the naturally occurring profiles of the AFIT UCC. Thermal and pressure profiles play a significant role in turbine output power generation as well as the survivability of vital turbine section components. Therefore, identification of which operating parameters influence the shape and magnitude of these profiles was sought. Theses influences will assist future research in the design of hardware necessary to create the most optimal profiles. Without this research, the transition from axial combustor to UCC will have minimal benefit. High thermal energy flow must pass from the combustor section to the turbine section in a manner favorable to the turbine.

The second objective focuses on the identification of the overall UCC system pressure losses. This objective encompasses establishing the benchmark for pressure losses within the flow path from hardware component to hardware component. Although some total pressure loss is required to drive the flow from inlet to exit, too much may induce unfavorable total pressure gradients impeding the flow of hot combustion products and reduce the overall work that the turbine can perform. This issue is of primary concern in implementing the UCC into an axial jet engine scheme. If the upstream ingested air source can't induce a cavity swirl after being injected into the cavity, combustion will not occur. In addition, total pressure loss due to heat addition at high Mach number is known as Rayleigh loss. Because the UCC will operate at higher

6

inlet Mach numbers in its core than traditional axial combustors, it is more susceptible to Rayleigh loss. The challenge of this research is to create Mach numbers representative of axial combustors and quantify those Rayleigh losses in a realistic fashion.

Finally, the third objective is the identification of emissions species emitted at the UCC exit plane. The emissions analysis is vital in understanding the combustion efficiency of the UCC. The locations where combustion is incomplete in regards to the resulting thermal and pressure exit profiles are indicative of areas of poor heat release and the formation of undesired species with regards to emissions standards and regulations. The tradeoffs among specific species are desired to show the UCC is providing the correct amount of activation energy in the form of heat to continue combustion within the circumferential cavity. These tradeoffs lead to the understanding of the UCC combustion efficiency at specific flow conditions indicating where the UCC is susceptible to flame out. Again, an understanding of which operating parameters best promote good combustion efficiency will aid future research.

These research objectives were accomplished experimentally with the use of the AFIT UCC and analytical tools to make conclusions and recommendations with respect to the results. Before conducting any experiments, a study of the fundamental principles involved with each research objective was performed to understand previous research and the relevant issues of concern. This allowed for the development of research objectives that would contribute to the understanding of UCC behaviors not previously understood. Testing was accomplished in a fashion consistent with previous research in hopes of continuing the push for the implementation of an UCC.

<center>**II. Literature Review**</center>

In continuing the effort to push the limitations of modern gas turbine engines, UCCs offer unique solutions to minimize engine size and weight. They accomplish this by reducing the number of components in the combustor section coupled with injecting fuel in a circumferential cavity that encircles the core flow. Within this cavity, the local equivalence ratio is above stoichiometric which results in additional complications when integrating this component to the turbine rotor. Burning continues to occur in the vane passage beneath the circumferential cavity which must be completed in a controlled manner to achieve complete combustion prior to the inlet plane of the rotor while also achieving a temperature profile consistent with high work extraction from the turbine. The heat release further results in high Rayleigh losses as the core flow operates at higher Mach numbers than typical axial combustors. The primary areas of study are the exit temperature and pressure profiles, the overall system losses, and the emissions characteristics.

2.1   Combustion and G-Loading

The growing demand for more powerful, efficient propulsion systems brings numerous challenges for reducing engine weight, engine fuel burn efficiencies, and emissions. The combustor section design is critical in tackling each of these challenges. Traditional combustor sections maintain an axial design allowing adequate length for the optimization of mixing and burning of fuel. Recent improvements in turbine design and cooling schemes are supporting higher combustor exit temperatures pushing combustors to operate closer to stoichiometric. With higher exit temperatures, propulsive efficiencies

<center>8</center>

are improved permitting the turbine to extract more power from the flow. However, traditional combustors require long axial length designs to complete the combustion process. This length is longer the closer to stoichiometric one operates. This places lowering engine weight and reducing emissions in opposition.

To begin deriving a combustor design solution aimed at solving this dichotomy of engine design principles, a look into some of the associated combustion physics will help to build a foundation for understanding the motivation behind current designs. One such design is the UCC born from the novel concept of swirling flow combustion studied by Lewis et al. [6] in 1977. This research was based off the effect of g-loading (G) and the resulting effects on forces due to buoyancy. Lewis argues that combustion can be enhanced and controlled by these buoyant forces (F_B) given a significant amount of g-loading by way of:

$$F_B = \rho_a g_c \left[1 - \rho_f / \rho_a\right] \qquad \text{Equation 2.1}$$

Here ρ_a and ρ_f are the ambient air density and the fuel density respectively. The driving g-load is dependent upon tangential velocity, V_{tan} about some radius, r and the Earth's gravitational constant, g_c.

$$G = \frac{V_{tan}^2}{r g_c} \qquad \text{Equation 2.2}$$

Using a combustion centrifuge, Lewis explored the effects of g-loading on flame speed. The results of the experiment showed that flame bubbles (burned gas products) in a 500g or greater environment and sitting in a fuel rich environment will propagate faster than turbulent flame fronts. In other words, the fuel rich environment generates a strong buoyant force that pushes combustion products ahead of the turbulent flame front.
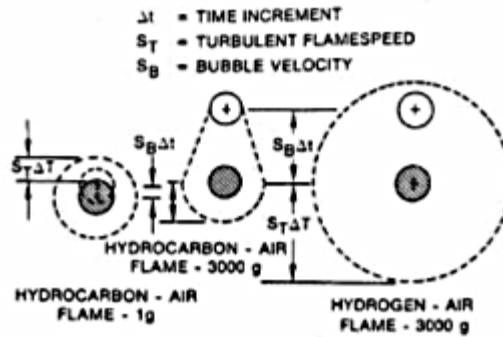
Figure 2.1. Propagation of flame bubbles [6].

Figure 2.1 shows this effect in the middle depiction as the cross hatched molecule

is forced out beyond the turbulent molecule by a distance $S_b\Delta_T$ where S_b is the bubble

velocity and Δ_T is some increment of time. The example on the left of Figure 1 shows

the case by which the bubble velocity is negligible and the flame bubble propagates with

the turbulent flame front. The right hand side depiction describes a situation where the

bubble velocity is significant however, the turbulent flame speed is faster. Lewis et al.

also saw a reversal of this trend when g loading was increased above 3500g. This was

explained by a phenomenon known as "heat stretch" where the flame speed increased to a

point where conduction with the ambient air generated enough heat loss to keep the

combustion reaction from propagating. Hence, with these bounds of 500g to 3500g

established as the parameters for housing productive swirl combustion, future

experiments would look to exploit the benefits of these increased buoyancy forces due to

centrifugal force.

In 1990, Yonezawa et al. [7] applied this concept of high-g swirl combustion

using a jet-swirled combustor which consisted of a traditional axial combustor with fuel

and air jets oriented both axially and circumferentially to impart swirl upon the

combustor flow. The design was capable of sustaining high g-loads and proved more efficient than a traditional axial flow combustor at the same loading condition.

This demonstration proved that the swirl imparted on the flow allowed for increased flame residence times as burning continued not only axially but circumferentially as well. The centrifugal acceleration of the rapidly rotating flow generated improved mixing and transport of hot gases. This multi-directional combustion allowed for more complete combustion and hence better efficiency. Overall, the jet-swirled combustor maintained better efficiencies at lengths approximately 33% less than the traditional axial combustor.

2.2   Ultra Compact Combustor Development

The immediate advantage of a jet-swirled combustor design would involve obtaining higher thrust to weight ratios with improved or constant efficiencies in a shorter axial length. One application proposed to exploit this advantage in a traditional gas turbine engine was the idea of an Inter Turbine Burner (ITB) by Sirignano et al. [8] in 1997. This proposal suggests the removal of the engine augmentation system with replacement by an ITB. The analysis shows that significant gains in specific thrust, weight reduction, and thrust specific fuel consumption (TSFC) reduction are achievable. The major challenge of the ITB system identified by the research is the development of a system that creates enough residence time to allow for complete combustion in a shorter span without continuing to burn in later turbine stages.

Hence, to answer the ITB challenge, in 2001 Anthenien et al. [9] developed an UCC design to serve as a main combustor or as an ITB replacing a traditional

augmentation system. The main principle behind the design was to house combustion in

a fuel rich annular cavity with a main core flow source passing through the center of the

annular cavity. Inside the hollow center lies a centerbody used to control the effects of

the core flow moving axially through the center of annulus. The blue air jets in Figure

2.2a induce a tangential velocity upon the air/fuel mixture generating a g-load about the

annular cavity. This environment supports combustion in the same chemical residence

times in a reduced axial length. In this case however, a circumference is used to support

the necessary residence length. Flame stabilization is achieved as the combustion

products are circulated around the full annulus. Complete combustion products are then

entrained into the main core flow by way of the buoyant forces induced by centrifugal

forces as described by Lewis [6].

(a)   (b)
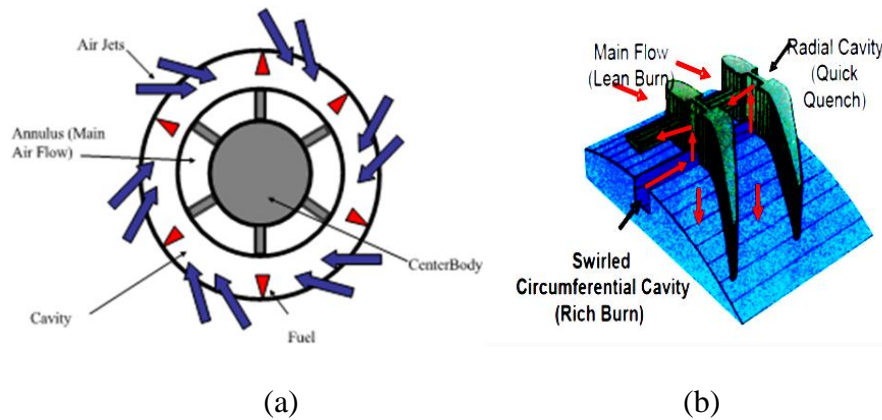
Figure 2.2. a) Blue air jets inducing swirling flow about annular cavity and b) extraction
by centerbody vanes into core flow for quick quench lean burn process [9].

Because chemical residence times are short and the residence times of combustion

products is long within the cavity due to the circulatory nature of the design, a quick

quench, lean burn process is possible. Hot combustion products, once entrained into the

main core flow from the fuel rich cavity, are then quenched quickly. Figure 2.2b depicts

12

this quick quench lean burn process allowing hot combustion products escaping the circumferential cavity to avoid burning in the main core flow at stoichiometirc conditions. Stoichiometric burning in the core flow would lead to higher core flow temperatures and improved emissions.

The stability of the designed UCC combustor rig was tested using an ethanol based fuel and JP-8 by Anthenien [9]. Lean blowout (LBO) was achieved in the main burning cavity at equivalence ratio of 0.5 and 0.7 for ethanol and JP-8 respectively. This demonstrated that the circumferential combustion in the UCC was similar to previous pre-mixed results for both fuels [9]. Overall, the combustor sustained operation with core flows ranging from 3.4 to 9 kg/min while feeding the air injectors with flows ranging from 0.7 to 2.3 kg/min. The overall combustor equivalence ratios ranged from 0.1 to 0.6. The overall combustor equivalence ratio is lower due to fuel in the cavity being introduced to the larger presence of air in the core flow relative to just the amount of air present in the cavity when calculating cavity equivalence ratio.

Using Anthenien's experimental set-up, Zelina et al. [10] continued the study of UCC operations. This study focused on the hot flow escaping the circumferential cavity into the core flow via the radial vanes upon the UCC centerbody shown in Figure 2.3.
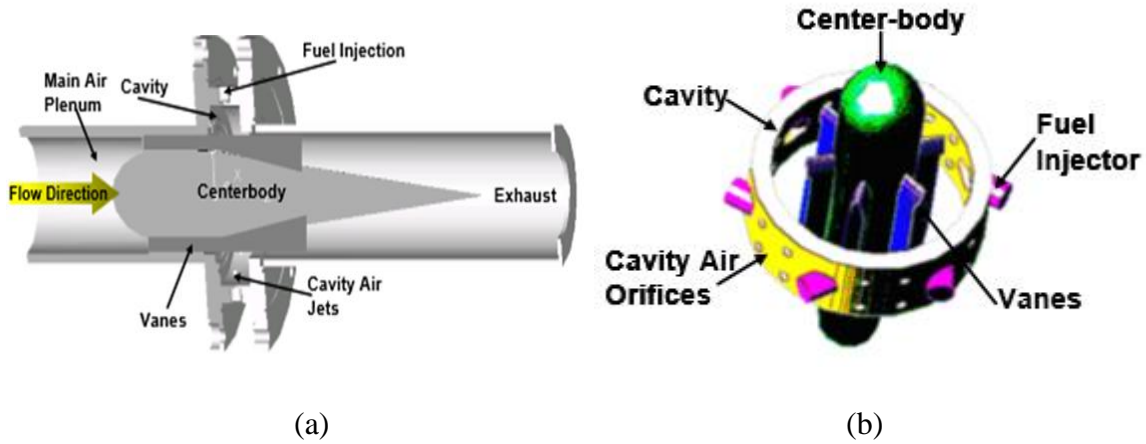
Figure 2.3. a) Center body housed in UCC experimental setup and b) detailed center body description showing radial vane interaction with fuel injector and air injector orifice [10].

The study consisted of four configurations using both a straight radial vane and a straight radial vane notched with a Radial Vane Cavity (RVC) to promote the transport of mixture out of the circumferential cavity and into the main core flow. A photograph showing the exit span of the UCC and the location of the radial vanes is shown in Figure 2.4a. Figure 2.4b shows the radial vane and the notch machined out to support radial transport. The notch when housed inside the UCC is oriented so that it faces the circumferential cavity.

Figure 2.4. a) Photograph of radial vanes housed in UCC and b) Radial Vane Cavity machined out of straight vane [10].

Overall, the performance of the RVC demonstrated a tradeoff exists between the cavity transport through the vane cavities and the manner by which fuel is injected into

14

the circumferential cavity. This tradeoff has significant impacts upon LBO performance, emissions performance and temperature distribution throughout the rig. The LBO performance of the rig was characterized at g-loads ranging from 200g to 2000 g. It was discovered that the UCC operated on a stability curve slope (cavity equivalence ratio as a function of g-load) similar to that of a conventional type of combustor.   G-load was calculated using Equation 3 and is largely a function of the tangential velocity calculated via Equation 2.2. Emissions performance will be discussed in Section 2.4.

$$V_{tan} = \frac{W_{a_{cav}}}{\rho_{cav} a_{ex}} \frac{1}{tan\beta}$$
<div align="right">Equation 2.3</div>

The mass flow of air into the cavity is represented by $W_{a_{cav}}$, the density of cavity air by ρ_{cav}, cavity exit area by a_{ex} and the fuel injection angle β. Zelina et al. [10] noted significant drops in combustion efficiency with the RVCs installed at g-loads around 550g and 1250g for different configurations. This drop in efficiency is attributed to low cavity equivalence ratios where reactions rates are low due to the poor mixing associated with a low g environment. The RVCs allowed for premature extraction at these low g-loads. As g-load increased, the heavier unburned mixture particles were thrown to the cavity outer diameter as a result of the centrifugal force induced by the increased g-load. Hence the RVCs induced a minimum combustion efficiency of 60% at the 1200 g-load condition.

To better understand this impact of RVCs upon efficiencies, a number of studies were performed using Computational Fluid Dynamics (CFD). Starting with Greenwood [11] in 2005, using the commercial software FLUENT and flow turbulence models, implicit flow solvers were developed for the UCC cavity. Greenwood was responsible

15

for the development of proper fuel injection models as well as models for the unique

modes of heat transfer occurring with an UCC sectional model. The sectional model

outlined only one-sixth of a full annular rig so as to keep the models simplistic.

In 2006, Anisko [12] carried Greenwood's research a step further by formulating

better cavity boundary models. These improvements used periodic boundaries to study

differences in the cavity geometry in hopes to better understand if the baseline boundary

was too large. Using a shorter cavity model, Anisko could better analyze hot areas of the

combustor removing colder flows that were present in larger boundaries.

Following Anisko, Moenter [13] used a different approach with a statistical model

known as Renomalization Group Theory (RNG) to represent the turbulence field. Using

RNG coupled with numerical models for pressure and mass flow rate, a two-dimensional

sixty degree sectional UCC model was formulated. Using fixed locations along the span,

Moenter quantitatively examined the flow path for temperature and velocity

considerations as well as others. From this pre-defined quantitative approach

quantifications of temperature distributions, emissions, efficiencies and pressure losses

were made. Figure 2.5 shows a temperature distribution (Kelvin) in his sectional model

analyzing a RVC with cavity flow moving clockwise and the main core flowing out of

the page towards the reader.
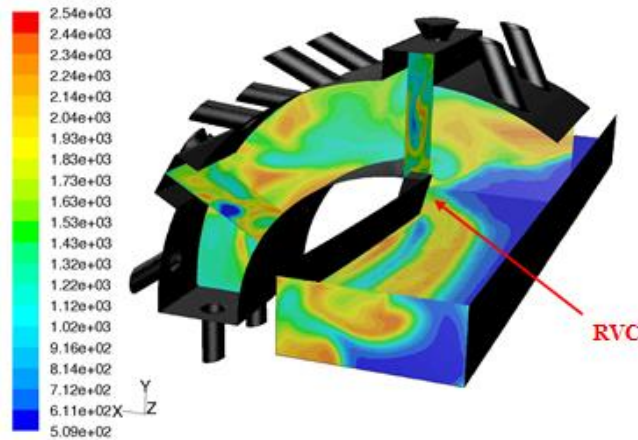
Figure 2.5. CFD generated temperature distribution (Kelvin) of 120 degree UCC sectional model [13].

The interaction among the RVC and the wake generated by flow passing over the RVC from the circumferential cavity into the core flow is of particular interest. Full annular, 360 degree, models such as those used by Anthenien [9] and Zelina [10] provided poor optical access to this region of interest. Moenter's [13] 120 degree model shown Figure 2.5 contains two fuel injection ports and additional air injection ports to account for the air mass flow that would exist in a full 360 degree annular model. This combination of injection ports for both fuel and air assured the correct equivalence ratio that would normally be seen in the full annular model.

This geometry established by Moenter [13] was used as the premise for a physical sectional UCC model developed by Anderson [14] in 2007. The modular type 316 stainless steel (SS) model held the capability to run both flat and curved cavity configurations. Figure 2.6 shows the flat cavity installed perpendicular to the main cavity as well as the modular curved 120 degree section on the right and its relation to the main cavity when installed.

17
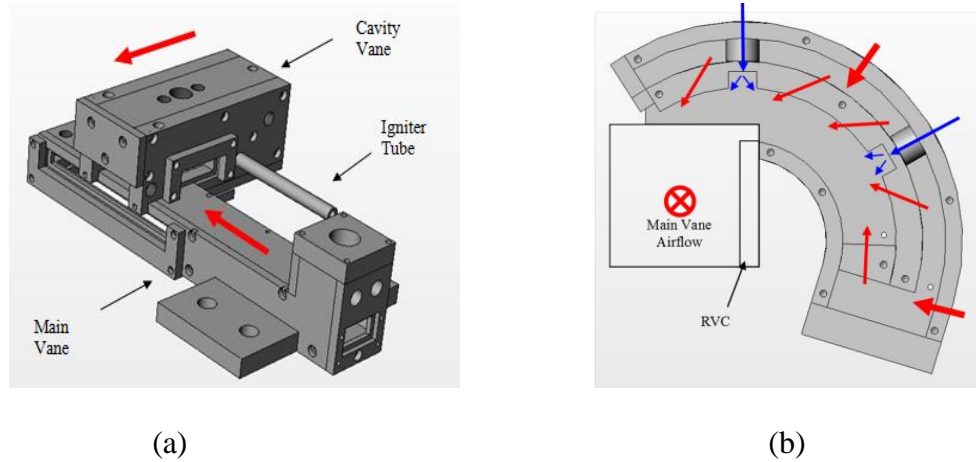
Figure 2.6. a) Straight and b) Curved Sectional pieces of UCC with red arrows indicating air flow and blue arrows indicating fuel flow [14].

The highly modular design was outfitted with numerous quartz windows to allow optical access for laser diagnostic equipment. One set of windows was located on the main vane cavity entrance and exit of the straight sectional piece. The exit window was located in the exhaust vent at the exit of the main vane which is open to atmosphere. The other set of windows existed on the flat cavity oriented across from each other at the RVC intersection. The curved sectional model contained no windows. The two piece sectional section model and surrounding laboratory allowed for main cavity air to be delivered up to 530K at 0.12 kg/s at atmospheric pressure.

Using the sectional UCC model developed by Anderson, Lebay [15] used the flat and curved sectional models to study UCC exit temperature profiles with variations in vane height, g-load and, mass flux ratio (MFR). Research showed that exit temperature profiles were most sensitive to MFR as shown in Figure 2.7. Changes in MFR were accomplished by varying core flow rates while at the same g-load. LeBay [15] studied four MFRs from 0.05 to 0.30. Increased MFR led to increases in the flame injection angle forcing flames to penetrate deeper into the ID wall as seen in Figure 2.7. Control

18

of this flame angle into the core flow along the vane span would allow for control over the exit temperature profile. Results showed that MFR = 0.3 produced excess amounts of hot flow being impinged on the ID wall while MFR = 0.2 did impinge on the ID wall but, improved the temperature profile. One of the obstacles for implementing an UCC is the ability to control this temperature profile to the turbine. A thermally non-uniform flow can create problems with power extraction and heat loading within turbine blades. Should all the flow's energy focus at the inner radius of the turbine, the power capable of being extracted would be less if that energy were directed across a longer radius away from the turbine ID. Turbine blades will consequently fatigue more rapidly at the hub than with a more evenly distributed temperature profile.

(a)   (b)
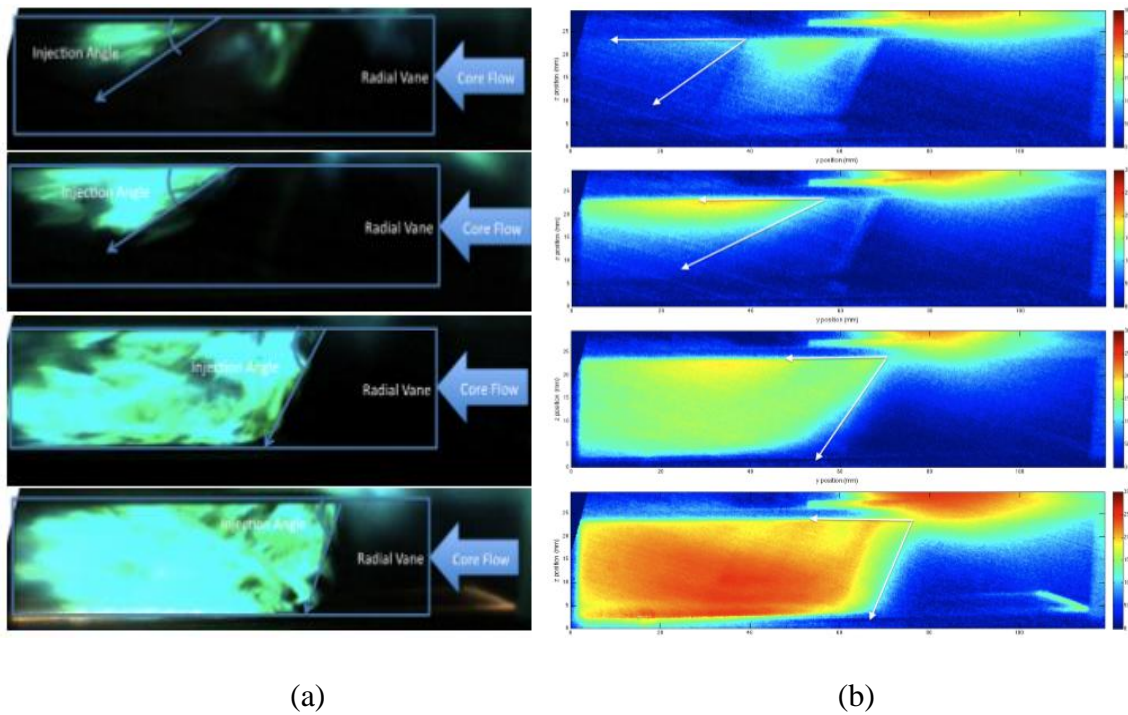
Figure 2.7. a) High-speed video image and b) time averaged high speed video from 28 mm vane, 1000g, cavity equivalence ratio = 2.0 at MFR=0.05 (top), 0.1 (middle top), 0.2 (middle bottom), and 0.3 (bottom) [15].

While the sectional model proved its benefits from being highly modular and offered a variety of optical access for laser diagnostics as well as video and camera work, Lebay [15] noted several limitations in comparing the UCC sectional design to the full annular design. First, the concept of mass migration out of the UCC cavity into the core flow is different for the sectional model. Because the sectional model has only one passage of escape by way of the core flow, the amount of migration at the core flow/cavity flow intersection is much greater than in a full annular UCC where flow migration from the cavity to core may occur at any circumferential distance along the centerbody. Secondly, when considering the vane housing the RVC used in the sectional model, the linear nature of the vane made it not a true airfoil and there was no true pressure side or suction side. Hence, there was no true pressure gradient across the vane passage.

Addressing the shortcomings of the sectional model outlined by Lebay [15], Bohan and Polanka [4] in 2011 conducted CFD research on how to integrate a full annular 'hybrid' vane ring into the axial flow path. The UCC hybrid vane design integrated the last compressor vane with the first turbine vane while delivering the same flow turning effects for the core flow. Together, the circumferential combustor and the hybrid vane provided for a substantial savings in engine weight. As shown by Blunck [16], a savings of 0.16%/ 1 cm of engine length can be achieved. For a typical turbofan / turbojet, this can result in a 2.4% weights savings for the engine.

Hence, the motivation of developing a hybrid vane is mainly two-fold: reduce engine weight by way of integrating the compressor exit vane and turbine inlet and control the direction of flow traveling from compressor to turbine. The term 'hybrid' is

20

utilized to describe this multi-purpose role of a single vane row within a UCC section.

Traditional gas turbine engines contain hardware to control the flow in and out of the

combustor section. To straighten compressor exit flow to the axial direction, an exit

guide vane is required. Likewise, turbine inlet guide vanes are necessary to turn flow

exiting the combustor and orient hot gases to the proper inlet angle for the turbine blades.

The UCC hybrid vane design and typical vane design used in this study are shown in

Figure 2.8b. As flow moves from left to right in Figure 2.8a, the core flow is taken off

the last compressor rotor where it enters the UCC hybrid vane passages. Swirling

combustion flows from the UCC cavity are then entrained into the core flow as buoyant

effects force the flow from the cavity into the hybrid vane passages. Finally, the

combined core and cavity flows pass through the exit of the combustor to the first turbine

rotor stage.
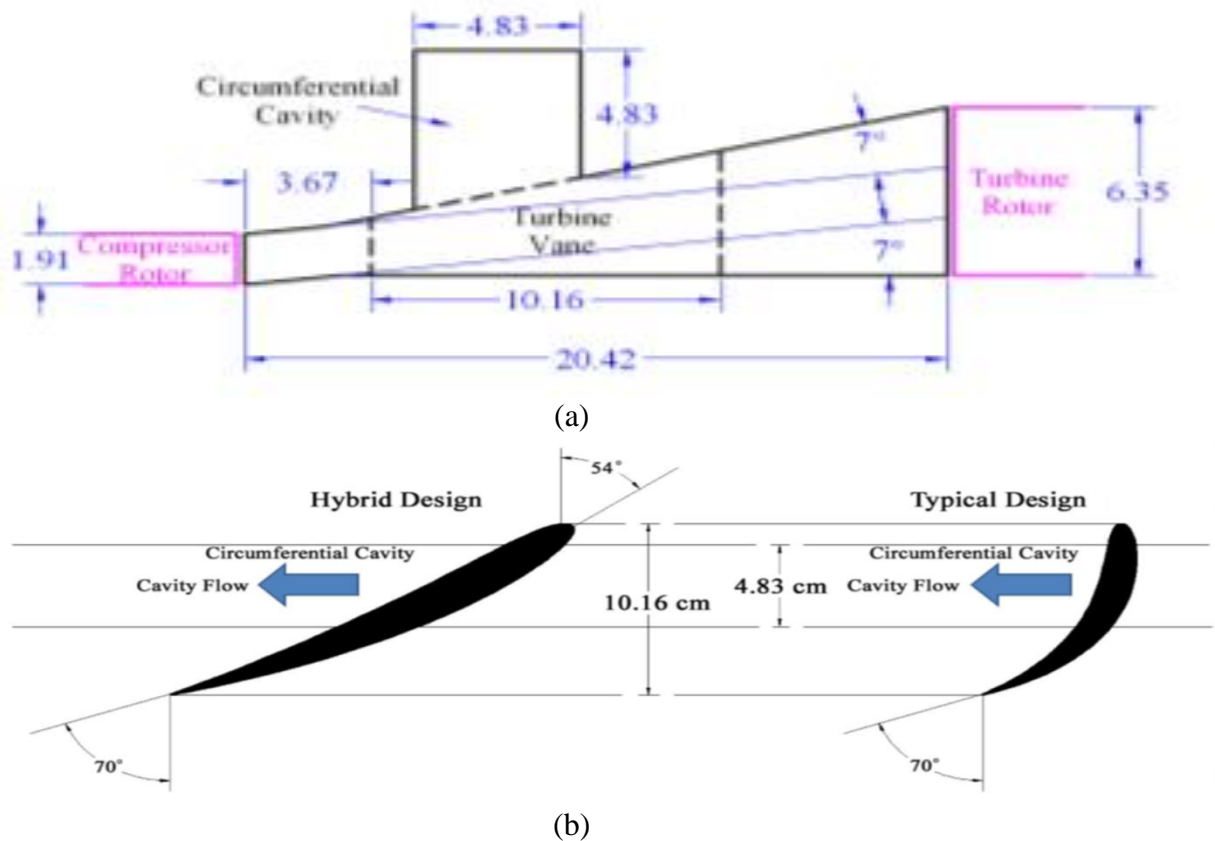
Figure 2.8: a) UCC axial scheme and b) hybrid vs. typical vanes used in CFD model [4].

The resulting differences in the UCC exit temperature profiles shown in Figure

2.9 created the need to better understand the transition of UCC cavity air into the core

flow along the vane sidewalls. Bohan and Polanka's [4] CFD results comparing the

typical vane and hybrid vane showed differing results with respect to temperature profile.

The typical vane design produced the highest temperatures near the ID wall with a

relatively constant temperature distribution occurring from the OD to the midspan. With

the hybrid vane however, the temperature profile decreased dramatically in comparison to

the typical vane near the OD. Bohan and Polanka's [4] hybrid vane was therefore

unexpectedly effective at moving hot gas across the vane to the ID.

22

This difference in profiles can be attributed to the differences in flow dissipation from cavity to core. The hybrid vane allowed cavity flow to exit at a further radial inward distance than flow exiting along the typical vane. This allowed the hybrid OD wall to remain much cooler as seen in Figure 2.9. Additionally, the differences in fluid momentum along the vanes attributed to the different profiles. Shown in Figure 2.8b, the typical vane stood more perpendicular to the swirling cavity exit flow thus causing the fluid to slow before turning to the axial direction. The hybrid vane's increased angle at the bow welcomed flow exiting the swirling cavity and formed less of a wall for the flow to turn about. Thus, the fluid exiting along the typical vane tended to stay closer to the OD as it was met by the perpendicular wall of the typical vane resulting in higher average temperatures.
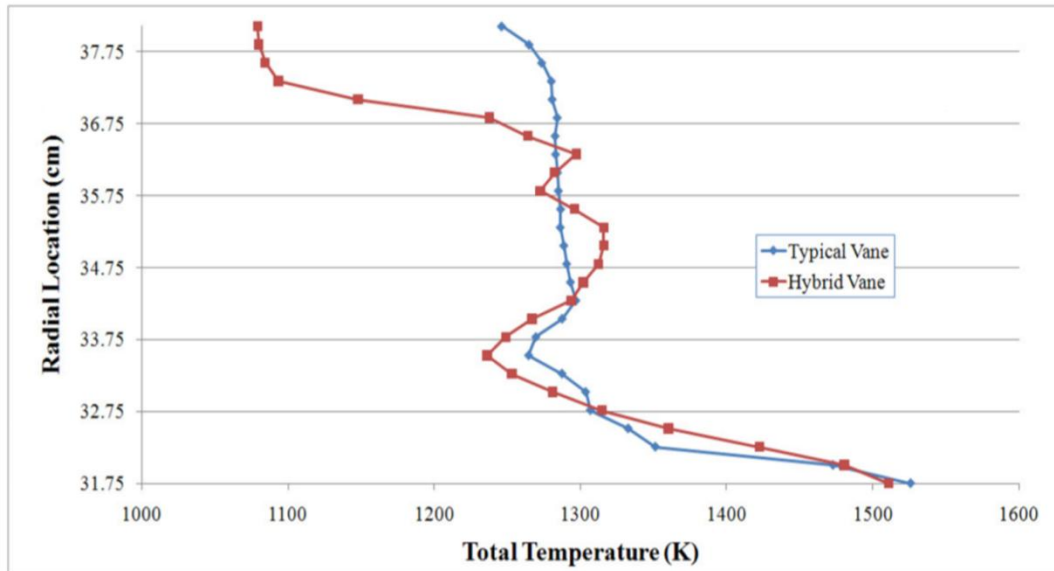
Figure 2.9. Circumferentially averaged exit temperature profiles for typical and hybrid vanes [4].

Parks [17] in 2012 investigated ways to improve the temperature profiles discovered in the research done by Lebay [15], and Bohan and Polanka [4] by developing vane sidewall schemes to control the angle at which hot flow was injected into core flow.

23

This would inherently change the angle at which the flow would be impinged upon the ID wall thus resulting in better temperature profiles across the exit span of the UCC. Thus, the motivation for Park's [17] vane design was to desensitize the shape and intensity of the hot combustion products to changes in operating parameters such as MFR and injection angle. Parks' [17] vane sidewall design is known as the "Tiger Claw" and consists of three channels directing the flow from the radial to axial direction at the intersection of the UCC's circumferential burning cavity and the main core flow.

Figure 2.10. Tiger claw vane sidewall design [17].

The Tiger Claw sidewall was studied in the same UCC sectional model as Lebay [15] and was successful in distributing the hot combustion products more uniformly across the span of the core flow versus concentrating the hot products on the ID wall as shown in Figure 2.11. Although more uniform, the temperature distribution was skewed toward the core section OD despite changes in MFR. These results are positive showing that the injection angle of hot gases into the core section can be controlled independently of MFR.
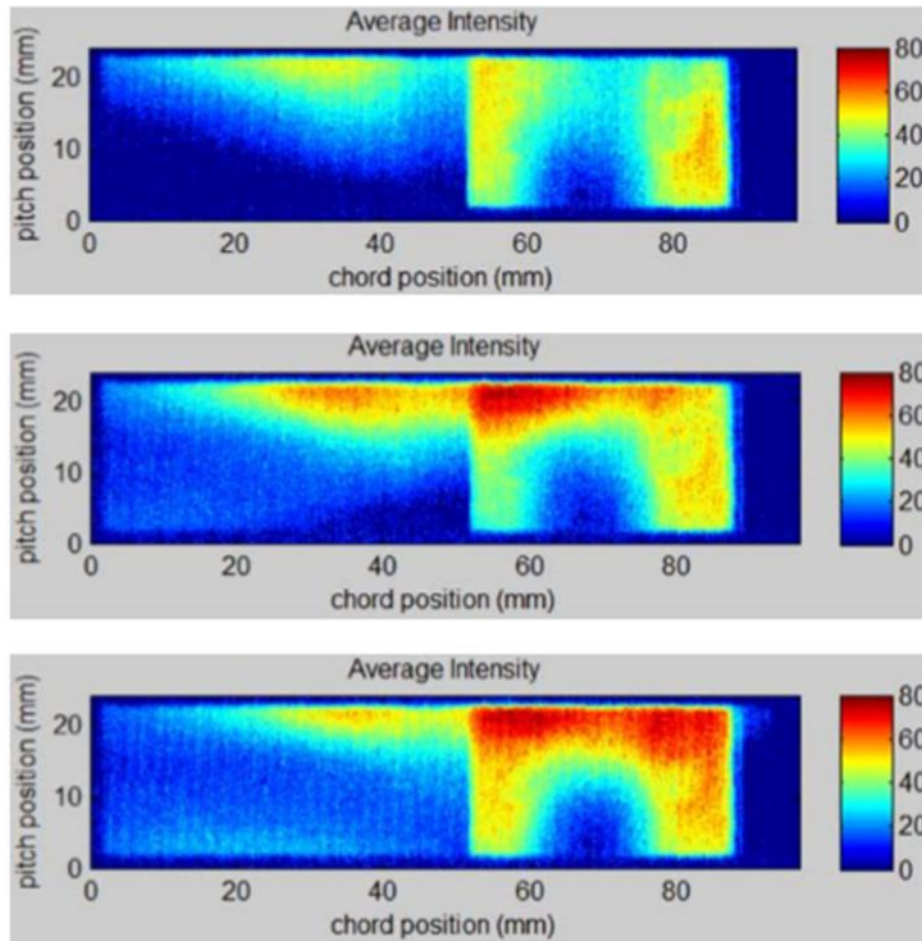
Figure 2.11. Time averaged high speed video showing side view of UCC exit plane flame intensity at MFRs of 0.1 (top), 0.2 (middle), and 0.3 (bottom) [17].

Thus, the impetus for integrating a hybrid vane inside a full annular UCC was born and in 2013 Wilson [5] designed and tested a full annular UCC at AFIT. Wilson's [5] highly modular design shown in figure 2.12 allowed for unique hybrid vane and UCC cavity air/fuel injection combinations to be studied. The sector rig designed by Anderson [14] and studied by both LeBay [15] and Parks [17] lacked the ability to capture the full annular mass flow extraction process from cavity to core. With a full annular design, more realistic engine conditions could be represented and studied all while having the ability to manipulate the cavity g-load. The design point was based off of realistic engine

25

flow conditions to include inlet flows at Mach 0.35 and 35° swirl and exit flows from

Mach 0.7 to 0.8 at 70° swirl. The core air design point was 0.45 kg/s given the current

COAL Lab capability and the desire to support a 70/30 core to cavity air flow split. Core

and cavity air flows were independently controlled to manipulate mass flow splits.

Finally, the full annular set-up would allow for increased optical access and

instrumentation about the UCC cavity in order to fully characterize UCC operation.
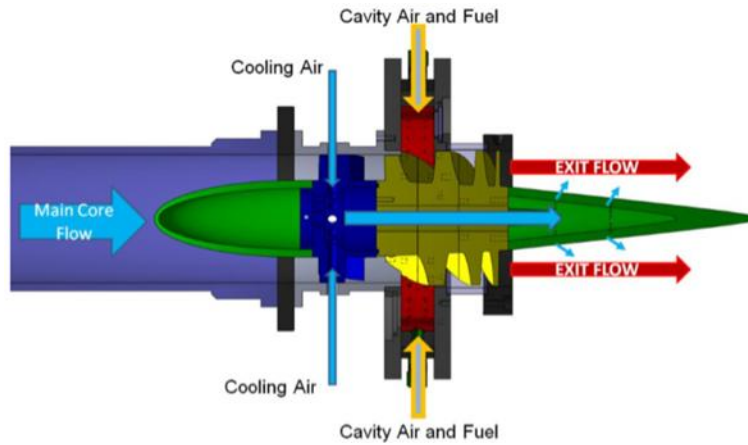
Figure 2.12. AFIT full annular UCC [5].

Wilson [5] developed a unique centerbody housing Bohan and Polanka's [4]

hybrid vane design. Flow over the hybrid vanes was manipulated using air injection

rings capable of swirling flow in both the clockwise (CW) and counter clockwise (CCW)

directions exploring different hybrid vanes and the impact of the swirl direction through

the vanes. The test rig could be configured to impart flow on either the suction side of

pressure side of the hybrid vanes by imparting flow in either the clockwise or counter

clockwise direction respectively as seen in Figure 2.13.

26

(a)   (b)
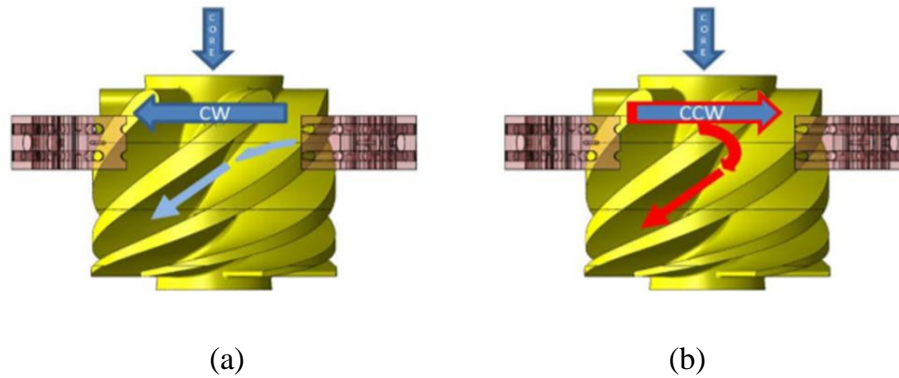
Figure 2.13. Hybrid vanes enclosed by air injection rings imparting a) clockwise or b) counter clockwise flows within the AFIT full annular UCC [5].

Wilson et al. [18] learned that swirl direction greatly varied the flame intensity within the UCC cavity. Using a 0.45cm air jet diameter injection ring and a high speed video camera, CW (pressure side impact) flow provided a much more uniform flame pattern inside the cavity while the CCW (suction side impact) flow flame pattern showed significant non-uniformity. The gap in flame seen on the bottom of figure 2.14 suggests that the CCW flow condition did not allow for proper migration of combustion products in the radial direction. Wilson et al. [18] attribute this to the flow having to turn 135° across the hybrid vane to exit into the core flow along the suction side of the vane. This significant amount of turning is not seen in the CW flow scenario as the suction side of the hybrid vane is already aligned with the CW flow. The turning of the flow in the CCW scenario caused disruptions in the overall cavity flow path thus reducing the achievable g-load and its benefits of increased air/fuel mixing.
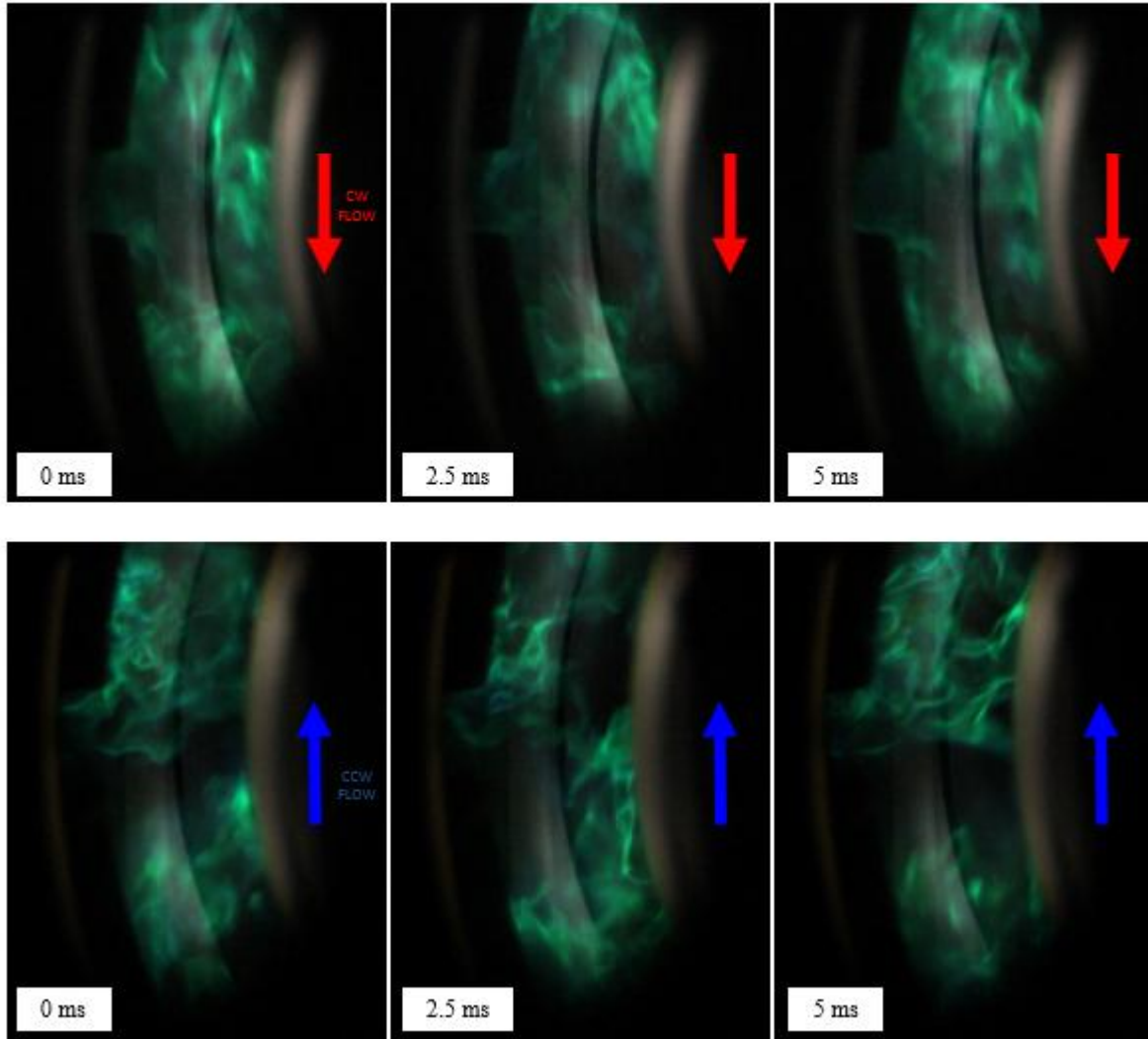
Figure 2.14. Flame intensities for CW and CCW flows in UCC cavity [18].

2.3 Ultra Compact Combustor System Losses

One goal in implementing a UCC is to be able to handle the upstream flow

conditions from the compressor and provide a flow stream to the turbine that looks like a

standard axial combustor. Accomplishing this goal requires several parameters to be

matched. One of these is the total pressure drop across the combustor. The target total

pressure losses across a conventional axial engine are approximately 10% [5].   While

minimizing losses is typically the objective for most systems, some of these losses are

necessary to maintain the flow through the compressor without back pressuring it and to maintain a positive pressure balance for the turbine cooling flow. The typical losses for each engine component are outlined in Table 2.1. These losses have been optimized given constraints to combustor sizing and overall aerodynamic losses.

Table 2.1. Component by component combustor pressure drop [5].

Component	Conventional Pressure Drop
Compressor EGV	1%
Compressor Exit Diffuser	3%
Combustor	4%
HPT Vane	2%
Total	10%

Pressure loss across the combustor system is necessary in maintaining the axial movement of flow within the combustor. The losses experienced within the turbine result from the amount of power extracted from the flow via the turbine rotor blades. Although these losses are necessary and cannot be completely averted, an optimized UCC design will match the pressure losses experienced in conventional axial combustors. Hence, the performance of turbine section should be completely blind to the type of combustor system used upstream.

One of the significant components to the combustor loss is Rayleigh losses. The addition of heat to subsonic flow forces a loss in total pressure at the exit of the combustor known as Rayleigh loss. Saad [19] provides an equation explaining the change in Mach number due to heat addition.

$$\frac{dM}{M} = \frac{1+\frac{\gamma-1}{2}M^2}{M^2-1}\frac{dA}{A} - \frac{(\gamma M^2+1)(1+\frac{\gamma-1}{2}M^2)}{2(M^2-1)}\frac{dT_t}{T_t} \qquad \text{Equation 2.4}$$

For the subsonic UCC flow, as heat is added, the Mach number moves up the upper half of the Rayleigh Curve shown in Figure 2.15. Rayleigh Theory, which assumes flow

29

through a constant volume, will continue to move to the right on the Rayleigh curve until the choke point at Mach 1 where any further increase in heat is not possible without adjustment to the upstream conditions. Thus, the flow characteristics are similar to that of flow behind a shock wave where total pressure is decreased [20].
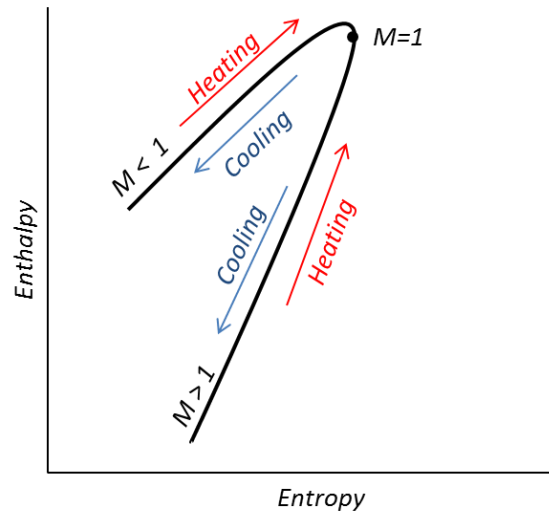
Figure 2.15. Rayleigh curve.

In a traditional combustor, these losses are minimized by diffusing the flow from the compressor so that the Mach number within the combustor is less than 0.1. Typical axial combustors, therefore, burn at low Mach number [1]. However, Rayleigh pressure losses are a significant concern in the development of the UCC as heat addition occurs at higher Mach numbers in this design compared to traditional axial combustors. This is attributed to the desire to take the air directly off the last compressor rotor where the Mach number is still upwards of Mach = 0.3. Furthermore, the integration with the downstream first turbine vane requires that the hot gases must leave the UCC combustor at a Mach number closer to 0.8. So, ideally, one would merely accelerate the flow from

Mach 0.3 to 0.8 through the UCC. However, doing so will generate excessively high Rayleigh losses.

At AFIT, Wilson's [5] use of two different center body designs effectively changed the Mach number of the flow as it moves through the core. The two designs included a tapered centerbody (TCB) generating a Mach distribution of 0.3 to 0.5 and a low loss centerbody (LLCB) with a Mach distribution of 0.2 to 0.5. Figure 2.16 shows the two center body designs and their difference in radial profile along the ID compared to the outer radius (OR). Both centerbodies were designed to accommodate the same inlet Mach number with differences only in profile shape. The profile shapes control the amount of heat released within the vane passages and therefore generate different exit Mach number distributions.
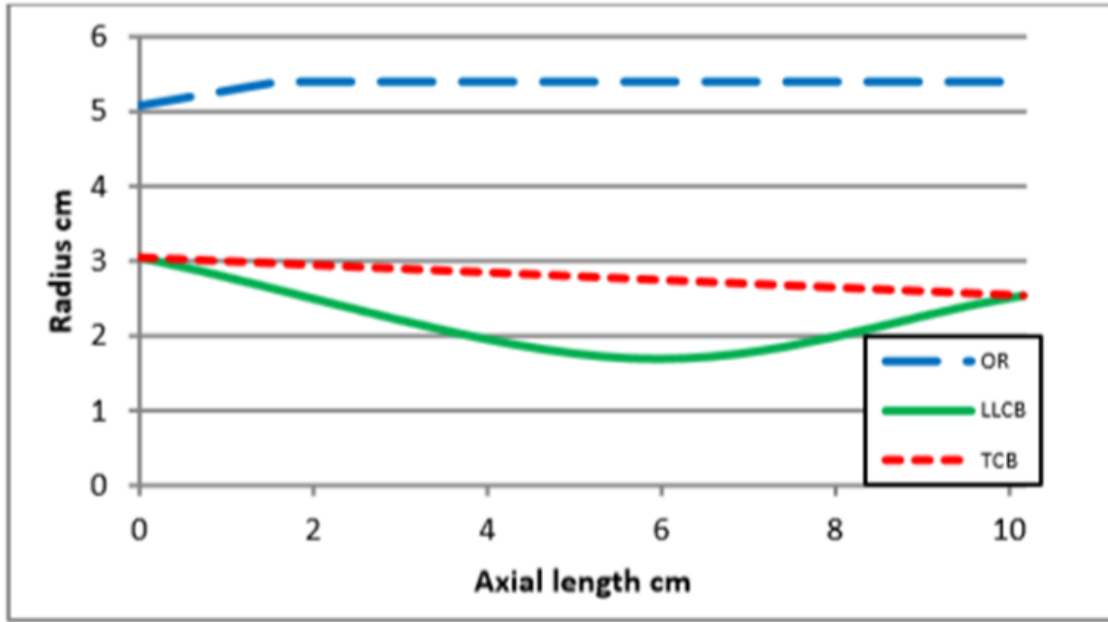
(a)
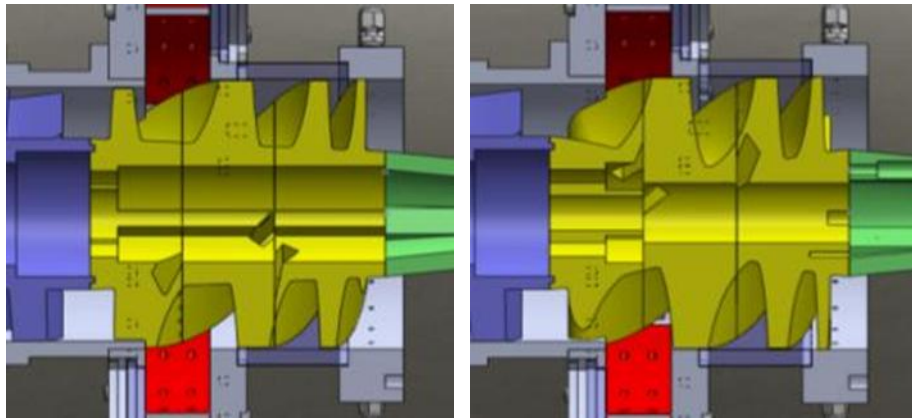
(b)   (c)

Figure 2.16. a) Center body radial profiles, b) TCB location in UCC and c) LLCB location in UCC [5].

These Mach distributions were determined from a MATLAB simulation aimed at balancing Rayleigh losses with desirable flow aerodynamics. An exit Mach number of 0.5 versus the traditional 0.8 is the highest achievable given the AFIT UCC's geometry limitations. Wilson et al. [21] concluded that an acceptable loss of 5.2% at a burning

Mach number of 0.2 to be optimal. This optimization balances the best achievable Rayleigh loss while minimizing aerodynamic losses. Further increases in Mach number would force boundary layers to form and eventually create regions of separated flow furthering the amount of aerodynamic loss.

Wilson [5] also correlated the UCC cavity equivalence ratio to the amount of Rayleigh loss highlighting the relationship between additional heat due to higher fuel flows and pressure loss as seen in Figure 2.17. The experiments were conducted at core/cavity flow splits of 85/15, 80/20, and 75/25. The highest exit Mach number achieved was 0.310 at a core/cavity flow split of 80/20. Wilson [5] asserts that because only 20% of the total air flow is attributed to the core and the resulting overall equivalence ratio is low (0.39) for the 80/20 case, more cavity air is needed to support higher exit temperatures and thus higher exit Mach numbers. Therefore, Wilson [5] attempted to produce results for a 70/30 flow split yet was unable to produce high enough cavity equivalence ratios given the limitations to fuel flow capability of the AFIT UCC. All in all, Wilson [5] achieved only a 0.07% pressure recovery moving from the TCB to the LLCB at a cavity equivalence ratio of 1.82. Higher losses could be captured with improvements to the rig's fuel flow capability running at a 70/30 flow split to achieve higher exit Mach numbers.
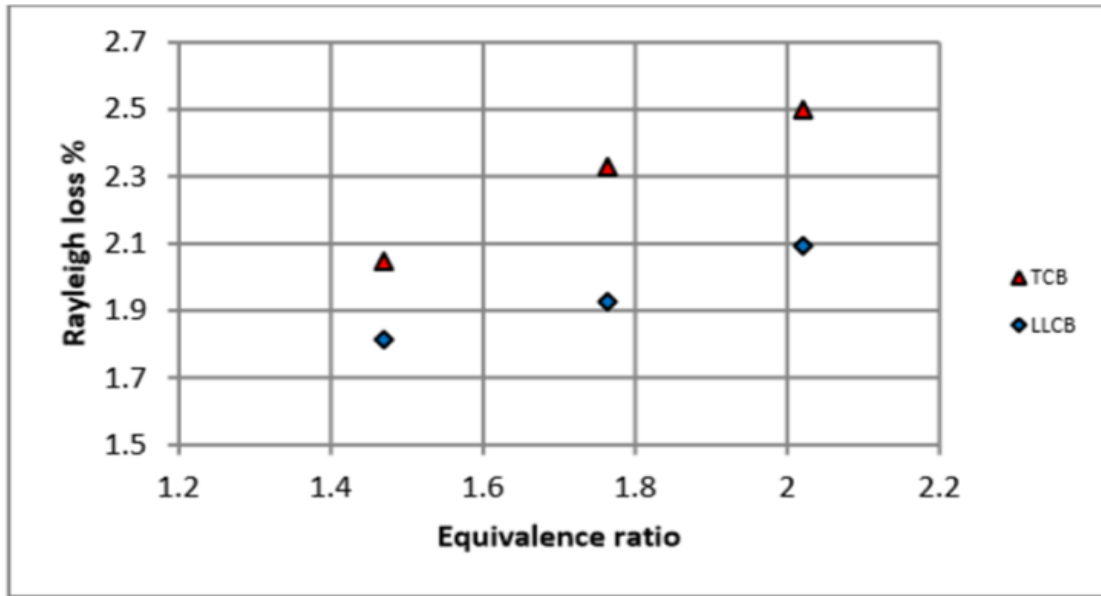
Figure 2.17. Rayleigh loss percentage as function of UCC cavity equivalence ratio [5].

Higher exit Mach numbers are a result, in general, of UCC operation caused by the UCC itself acting as a nozzle. This decrease in area was quantified by Radtke [22] at 47% for the AFRL UCC and causes an axial acceleration of the flow through the UCC. The UCC does not maintain a constant mass flow from entry to exit due to the additional air and fuel mass entrained by the core flow from the circumferential cavity. The increased mass flow results in higher Mach numbers through the UCC. This results in lower work potential for the engine as Mach numbers are already elevated.

Radtke [22] quantified total Rayleigh losses with the AFRL UCC by subtracting the cold flow pressure loss from the hot flow pressure loss. The same mass flows were run with both non-reacting and reacting flows and the increased pressure drop due to heat addition was recorded as the resulting Rayleigh loss. Cold flow pressure losses were measured between 1.5% and 2% and hot flow pressure losses were found to be between 0.779% and 1.738%. Experimental results yielded lower exit Mach numbers at

approximately 0.23 to 0.31 which are 10% to 40% lower than predicted by Rayleigh theory respectively.

One way to describe the difference between theory and experiment is by the constant area with heat addition assumption. Radtke [22] notes that his UCC configuration did not maintain a constant area as his UCC effective area decreases 47% from entrance to exit. With the addition of heat, this area is decreased another 4% from the resulting displacement boundary layer. Furthermore, the Rayleigh losses were relatively low for this experiment. This result was linked to the low core Mach numbers run in this experiment. To properly match the core flow Mach, the core mass flow would have to be increased up to 40% to match expected theoretical values. Therefore, Radtke [22] achieved significantly lower additional pressure losses than expected from the heat addition.

In 2012, Johnson [23] performed CFD research to better understand the UCC sizing needed to generate the pressure losses similar to that of a conventional type combustor. Using the same CFD model as Bohan and Polanka [4], Johnson [23] determined that this 76.2 cm diameter full annular model generated pressure losses up to 12%. Of note is the fact that the Bohan and Polanaka's [4] model was not optimized to produce a realistic combustor exit Mach number of 0.8 and was used primarily to study the interaction among core and cavity flows with an exit Mach number of 0.3. Although the model maintained good aerodynamic performance, the resulting pressure loss was not ideal.

Therefore, when Johnson [23] added heat to Mach 0.3 flow, the pressure losses grew more so than with cold flows. The challenge was now to find a hypothetical UCC

geometry that would generate a more realistic UCC exit Mach number (M = 0.8) while

minimizing Rayleigh pressure losses as much as possible. The geometry was constrained

to the same UCC cavity size and axial length used by Bohan and Polanka [4] with

changes only to the sizing of the hybrid vanes in between where burning continued once

cavity flow was entrained into core flow. The best performing Rayleigh loss geometry

generated losses at 1% and is shown in Figure 2.18. Johnson's [23] simulation utilized

20 vanes each with a height of 18 cm and an axial length of 4.83 cm. Although highly

effective in mitigating pressure loss, the increased hybrid vane size forced the flow to

separate too early and good aerodynamic performance could not be maintained. Thus,

some optimization of the geometry is needed to maintain good aerodynamic and Rayleigh

loss performance.
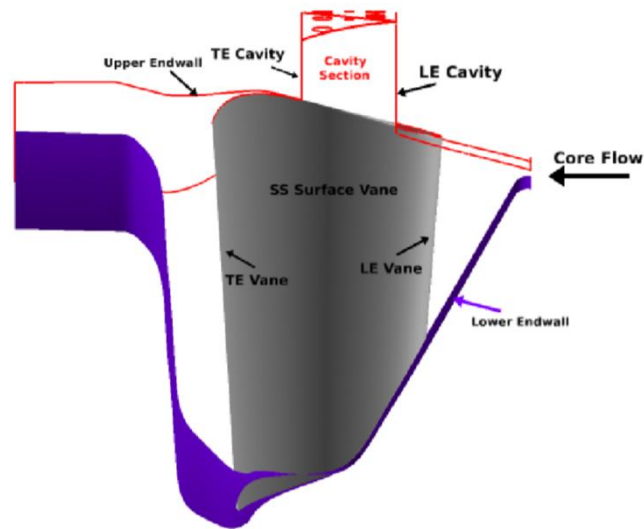
Figure 2.18. UCC hybrid vane geometry used in Johnson CFD simulation [23].

To continue the operational characterization of the AFIT UCC, a Rayleigh loss

study at more realistic Mach numbers (Mach 0.8) should be conducted. This can be

accomplished with improvements to Wilson's [5] experimental set-up with special regard

to the necessary fuel flow requirements for a higher cavity equivalence ratio at increased

cavity air percentage rates (30 and above).

2.4   Jet Engine Combustion Emissions

With the goal of future gas-turbine engines aimed at high efficiency and low

emissions, combustor designs are becoming more and more dependent upon the mixing

of fuel and air coupled with lean burning. The efficiency of the quick quench, lean burn

process is fundamental to understanding combustion emissions. The quantification of

emissions is often described in general through an emissions index (EI). The EI is

defined by the Society of Automotive Engineers [24] as:

$$EI_x = \frac{Moles\ of\ X}{Moles\ of\ Fuel} * \frac{Molecular\ Weight\ of\ X}{Molecular\ Weight\ of\ Fuel} * 1000 \qquad \text{Equation 2.5}$$

Jermakian et al. [25] studied the rich burn, quick-mix, lean burn (RQL) process to

minimize the formation of Nitrous Oxides (NO_x) in an experimental rig set-up using air

jet cross flows in non-reacting and reacting conditions at high pressure. NO_x formation

has become the target of many environmentalists for its ozone depleting impact on the

Earth's atmosphere. RQL is viewed as the next step in further reducing NO_x formation

behind other processes such as Lean Premixed Prevaporized (LPP), Dry Low NO_x

(DLN), and Lean Direct Injection (LDI).

The RQL process describes the same chain of events that occurs within an UCC.

A fuel rich cavity uses buoyancy effects to push hot combustion products in the radial

direction into an axial core flow quenching the combustion products and then

transitioning into lean burning along the remainder of the UCC vanes. The formation of

NO_x along that process is notionally depicted in Figure 2.19. From their experiment,

Jermakian et al. [25] discovered that a major driver in NO_x formation is the air temperature entering the fuel rich cavity of their set-up. Additionally, elevated pressures in the quick-mix section of the set-up also increased the formation of NO_x. Elevated pressure experiments produced NO_x concentrations of 27.2 ppm at six atmospheres versus 10.4 ppm at one atmosphere.
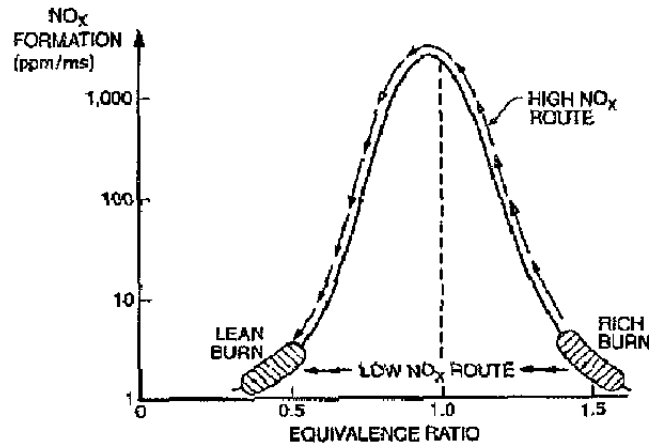
Figure 2.19. Formation of NO_x during the RQL process [25].

Lastly, the location of where the NO_x was detected is most notable from this experiment. NO_x was found to be in its highest concentration at the end walls of the combustor. This is believed to be the result of poor mixing in the quick-mix section where jets of fuel were found to form along the end walls of the rig versus being mixed within the quick-mix section. Consequently, the fuel-rich end walls housed enough heat to support the formation of NO_x. The study shows that NO_x formation is heavily dependent upon sources of heat. NO_x is formed by mechanisms requiring very high temperatures and Turns [26] describes NO_x formation via the thermal mechanism (Zelodivich Mechanism) requiring an activation energy of 319,050 KJ/kmol typically seen in areas exceeding 1800K. Thus, this temperature dependence further increases the

38

need for efficient fuel/air mixing. The ability to quick quench prevents temperatures from reaching levels favorable to NO_x formation.

In addition to pollution control, combustion efficiency is also determined by way of emissions analysis. Total unburned hydrocarbons (UHC) levels are indicative of combustion efficiency as they indicate to what degree the fuel is burning within the combustion chamber. Using a well stirred reactor, Sturgess et al. [27] linked the formation of UHCs to combustion chamber residence times and chemical reaction temperatures. Looking specifically for carbon monoxide (CO), results showed that for lower residence times and lower temperatures, CO emissions are high due to incomplete combustion. Similarly however, CO emissions are also high for higher temperature reactions with heavier fuels due to the dissociation of carbon dioxide (CO_2). Therefore, reactions occurring at the same temperature resulted in different CO concentrations for different reactor residence times. Likewise, heavier fuels yielded higher concentrations of CO at the same temperatures.

CO is a product of hydrocarbon reactions and the consumption of CO occurs much slower than the consumption of hydrocarbons in a fuel rich environment. However, using full-scale aircraft engines, Sturgess et al. [27] showed that in some circumstances the concentration of CO can be found in higher quantities than UHCs given poor recirculation conditions. If fuel is mixed into core flows too quickly or escapes into cold spots of a combustor liner, then it will remain unburned and flush itself out before mixing again with the hot mainstream flow. This condition was witnessed in increasing fashion for engines operating at lower power levels.

As engine power is increased from idle to full power moving right to left in Figure 2.20, both UHC and CO emissions decrease exponentially. However, there exists some power setting where CO concentrations are higher than UHC concentrations. This suggests that there is some mechanism by which UHC emission can be controlled. These mechanisms exist in the development of how to best design the formation of recirculation zones to promote better mixing and increase the residence times of hydrocarbons within the combustor before they exit with colder flows outside of the mainstream hot core flow. This balancing act associated with CO and UHC concentrations is directly applicable to a UCC engine application. The quick quenching process which involves the mixing of the hot fuel rich combustion chamber flow and cool main core flow will have a direct impact upon the emission levels measured at the exit of the UCC.
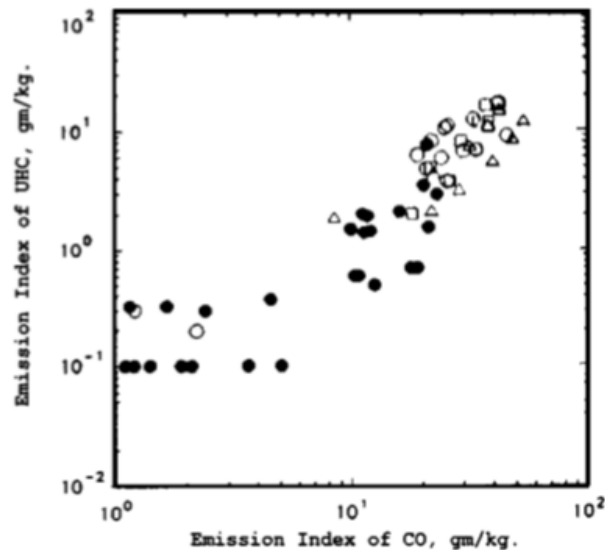
Figure 2.20. UHC vs CO Emissions for large and small jet engines (one engine per shape) [27].

In addition to the tradeoff among CO and UHCs is the overarching tradeoff among performance and pollution. The balance of CO/UHC to NO_x levels is a study of engine types comparing the traditional performance enhanced Axially Staged Combustor

(ASC) versus the non-traditional, more pollution conscious RQL methodology

combustor.   Testing commercially available full-scale ASC and quasi-RQL combustors,

Sturgess et al. [27] performed trade studies comparing CO, UHC, and NO_x emissions for

an array of combustor inlet temperatures. The experiments for both combustor types

yielded similar trends in regards to comparison of the three emission types.

(a)   (b)   (c)
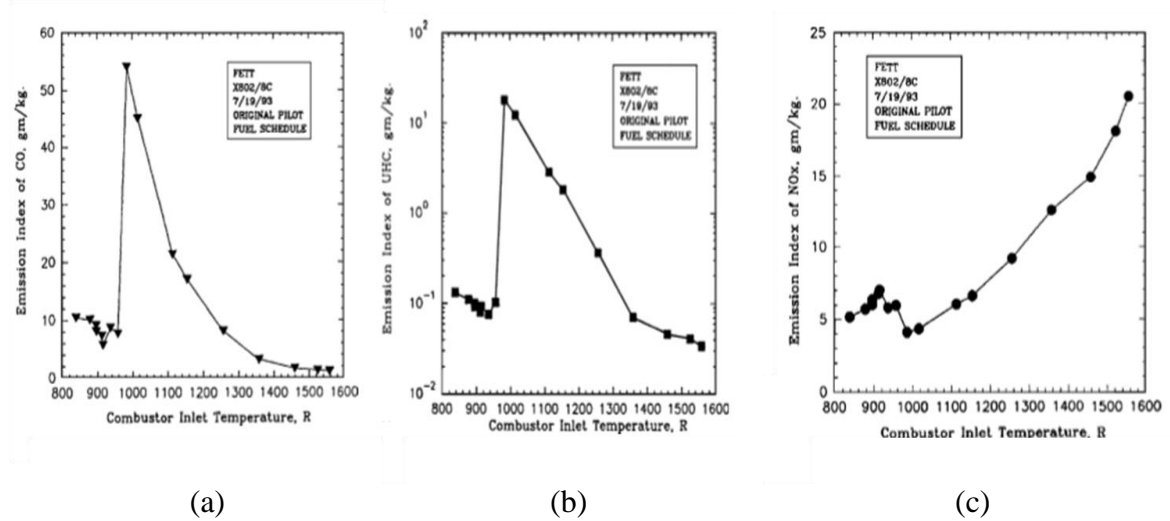
Figure 2.21. Pratt and Whitney ASC emission concentrations versus combustor inlet
temperature for a) CO, b) UHC, and c) NO_x [27].

The CO and UHC curves follow the same expected trend as the combustor inlet

temperature is increased decaying exponentially with inceases in temperature

(representing engine power settings). As this inlet temperature is increased the

mechanism for NO_x formation is highly favored and NO_x concentrations begin to climb

exponentially. These trends are expected and the resulting trade-off is seen within each

combustor type respectively.

To understand how differences in combustor types (ASC vs. quasi-RQL)

compare, Sturgess et al. [27] plotted NO_x emissions against CO emissions for an ASC

(open cirlces) and quasi-RQL combustor (solid triangle) in Figure 2.22. As power is

41

increased, the data points move from right to left. The staging of the ASC describes how

both curves start and maintain the same data points until the ASC curve folds back upon

itself, showing the increased emissions for multiple stages at increased engine power.

Because the majority of data points for the ASC exist further right and higher than the

data points of the RQL combustor, the ASC is the poorer low-emissions performer.

Notice the quasi-RQL combustor experiences larger reductions in CO coupled with

smaller penalties in NO_x versus the ASC.
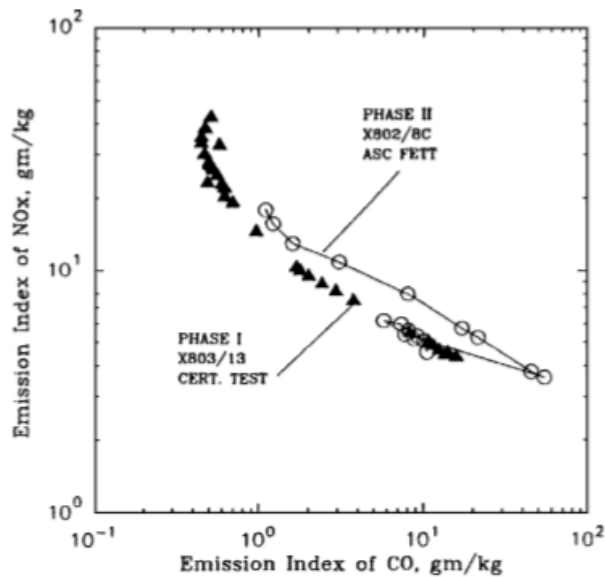
Figure 2.22. NO_x EI versus CO EI for ASC (circle) and RQL combustors (triangle) [27].

Using the AFRL UCC to study the effect of a RVC on the radial vanes of the

UCC centerbody, Zelina et al. [3] quantified EIs for several species collecting emissions

with a 5 port oil-cooled probe at the rig exit. Recall the purpose of the RVC is to

promote burned mixture mass entrainment from the circumferential cavity into the core

flow. The EI for CO is indicative of this entrainment process as the mechanism for CO

formation will lose the heat necessary to continue the production of CO as more and

more of the hot circumferential cavity flow is quenched by the cooler main core flow.

Figure 2.23a shows the vanes configured with a RVC are more effective in quenching the CO process than the flat vanes.

The RVC curve (yellow) in Figure 2.23a shows that increases in cavity equivalence ratio yield lower EI_{CO} as the mechanism for CO formation is quenched out due to the enhanced entrainment of cavity flow into the core flow provided by the RVC. As the g-load is increased and cavity equivalence ratio remains lean, EI_{CO} increases significantly as seen in Figure 2.23b. As the cavity equivalence ratio became richer, increased g-loads cause the formation of CO to quench out at an increased rate.

(a)   (b)
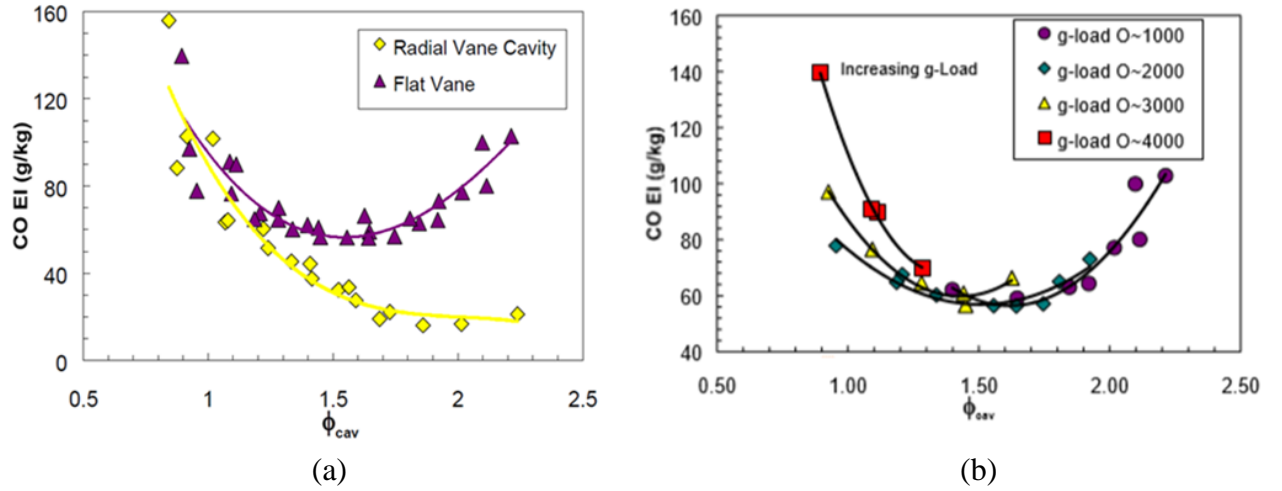
Figure 2.23. a) EI_{CO} as a function of φ_{cav} for flat vanes and RVC vanes and b) with effect of g-loading [3].

In addition to studying the effect of an RVC on emissions, Anderson et al. [28] also studied the effect of swirl direction in the UCC cavity. Comparing two fuel types, a Fischer-Tropsch (FT) blend and JP-8, in combination with different cavity swirl directions, the impacts on combustion efficiency and NO_x /CO tradeoffs were quantified.

Recall Lewis' [6] concept of bubble velocity, S_b where ρ_u is the density of the

unburned mixture, ρ_b is the density of the burned mixture, R is the radius of the

circumferential cavity and g is the g-load.

$$S_b = \frac{\rho_u}{\rho_b}\sqrt{Rg} \qquad \text{Equation 2.6}$$

Assuming a fixed radius, R and neglecting differences in gas constants, equation 8 is

realized where T_b is the UCC cavity exit temperature and T_u is the cavity inlet

temperature.

$$S_b \propto \frac{T_b}{T_u}\sqrt{g} \qquad \text{Equation 2.7}$$

Setting T_b to the adiabatic flame temperature of JP-8 the ratio $\frac{T_b}{T_u}$ may assume a maximum

value and combustion efficiency may be plotted in terms of $\frac{T_b}{T_u}\sqrt{g}$ which is referred to as

the swirl parameter (SP) [29]. SP may be used as a correlation to the amount of g-

loading within the cavity and in a sense removes the systemic variations associated with

the measurements for combustion efficiency.

The combustion efficiencies discovered by Anderson et al. [28] shed light on the

UCC's optimal region of performance. Figure 2.24a shows the combustion efficiency for

both the FT fuel and JP-8 in the CW and CCW direction at two distinct values of cavity

equivalence ratio, 0.8 and 1.2. The fuel lean combustion efficiencies are significantly

lower than the efficiencies at fuel rich conditions. Hence, the UCC favors a fuel rich

environment. Figure 2.24b shows the improvement to combustion efficiency as the

cavity equivalence ratio is increased. This trend shows a significant dependence on

cavity equivalence ratio. It is important to note however, that as cavity equivalence ratio

is increased, the UCC as a whole operates closer and closer to stoichiometric. Anderson

et al. [28] concluded that the increased combustion efficiencies at higher and higher cavity equivalence ratios shown in Figure 2.24b are most likely due to the increasing level of heat release seen throughout the entire UCC. Overall, the UCC runs at lean equivalence ratios given the significantly greater amount of core air flow to cavity air flow.

(a)   (b)
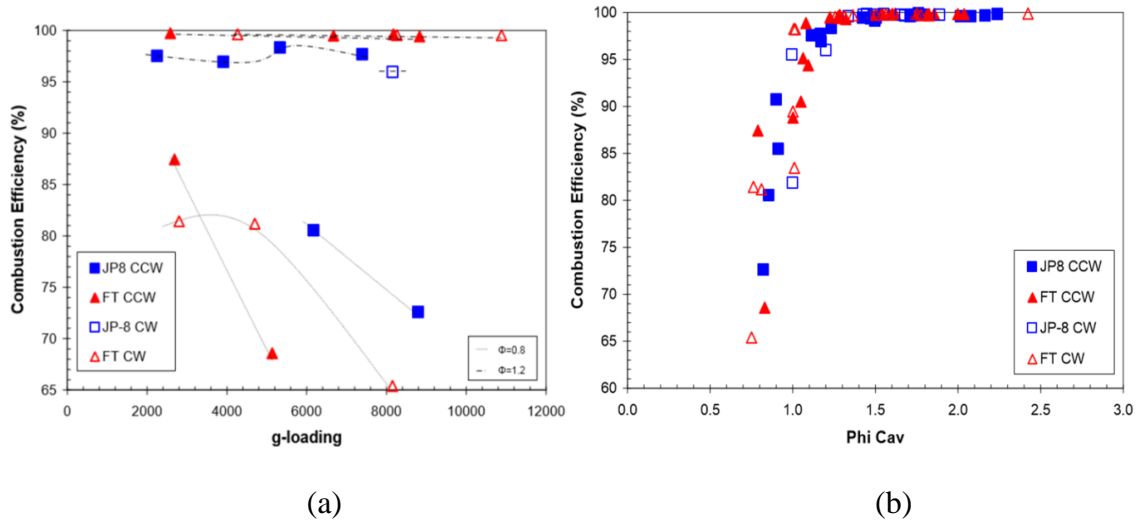
Figure 2.24. a) Combustion efficiency as a function of g-load and cavity equivalence ratio and b) only as function of cavity equivalence ratio [28].

The trade studies conducted by Anderson et al. [28] indicate the amount of burning among FT fuels and JP-8 was independent of swirl direction. The charts in Figure 2.25 show non-unique trends for trade-offs among NO_x and CO (a) as well as CO and UHC (b). Anderson attributed these results to the impacts of different fuels and the idea that flow swirl may be lost as reactions proceed from the cavity exit to the UCC exit.
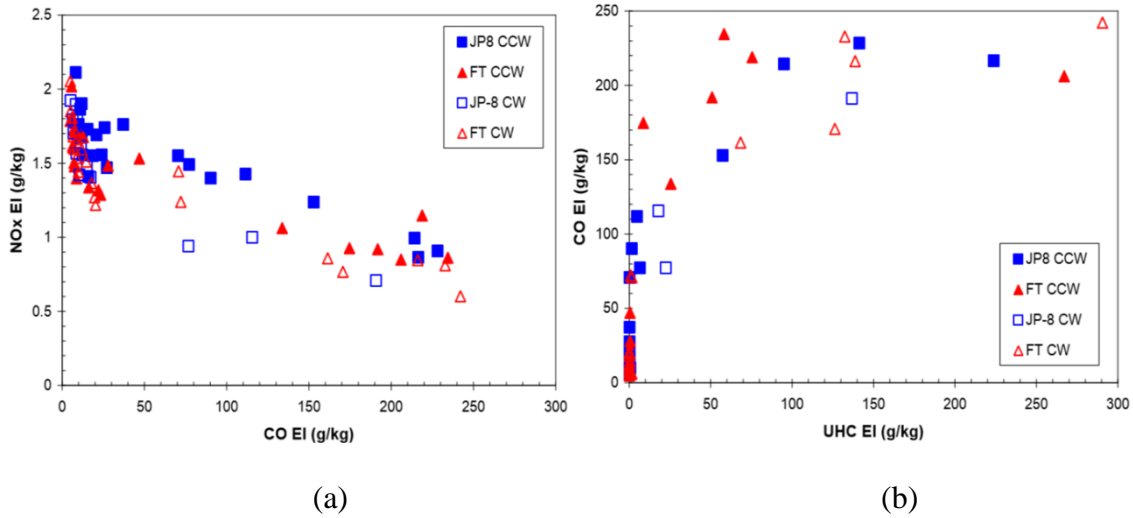
Figure 2.25. Trade-off curves for a) NO_x / CO and b) CO / UHCs [28].

2.5   Combustor Exit Profiles

Gas turbine engine performance is based off several key performance parameters including the flow characteristics of hot gas passing from the combustor exit to the turbine inlet. The issues of mechanical and thermal fatigue upon turbomachinery components are of critical importance. In today's engines, flow temperatures well exceed the melting points of turbine components and the optimization of heat transfer mechanisms and the spatial profiles of temperature and pressure play a key role in engine performance.

One of the obstacles for implementing an UCC is the ability to control this temperature profile to the turbine. A thermally non uniform flow can create problems with power extraction and heat loading within turbine blades. Should all the flow's energy focus at the inner radius of the turbine, the power capable of being extracted would be less if that energy were directed across a longer radius away from the turbine

46

ID. Turbine blades will consequently fatigue more rapidly at the hub than with a more evenly distributed temperature profile.

Using a combustion simulator in combination with the AFRL's Turbine Research Facility (TRF), Barringer et al. [30] studied turbine inlet profiles of temperature and pressure. The simulator was comprised of three concentric annular flow paths. The flow paths were oriented with several arrays of heat exchangers and dilution holes that controlled the amount of flow and thus the shape of the temperature profile entering the turbine. These profiles were measured with a seven-headed temperature rake across the exit span of the simulator and the non-dimensional temperature, θ, was defined by Equation 2.8 where T is defined as a local exit temperature and T_{avg} is defined as the average temperature across the exit span.

$$\theta = \frac{T - T_{avg}}{T_{avg}}$$

Equation 2.8

The combustor simulator was capable of generating a wide range of temperature profiles by manipulating the mass flow splits thereby producing realistic combustor exit temperature profiles. Their measured profiles ranged from midspan averaged (107), ID skewed (109), and OD skewed (108) along with mostly uniform distributions (125 and 127) as seen in Figure 2.26a. These profiles compared well to commercial engine combustor profiles shown in Figure 2.26b.
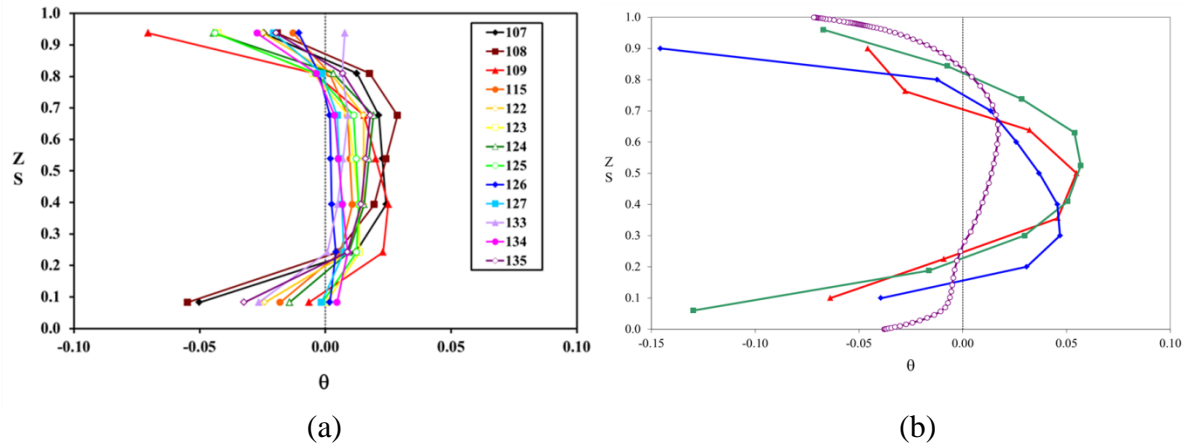
Figure 2.26. a) Combustion simulator generated temperature profiles and b) commercial engine combustor temperature profiles [30].

Samuelson [31] describes why such profile shapes are desired in order to protect the integrity of the turbine engine section. Too large of a radial and/or circumferential variation of the local temperature from the mean across the exit plane of the combustor may generate hot spots. These hot spots may destroy turbine components such as disks and blades. Ideally, the temperature at the 0% span should be reduced to protect the linkage among turbine rotor blade and shaft and at the 100% mark to avoid overheating the blade tip region. The increased circumferential area of turbine blade in the midspan region is better suited to handle the elevated heat flux. Thus, the desired temperature profile is skewed towards the OD.

Samuelson [31] further defines both a pattern factor and profile factor to characterize the combustor exit temperature profile. In Equations 2.9 and 2.10, T_3 is defined as the combustor exit temperature and T_2 is defined as the combustor inlet temperature. The pattern factor describes the deviation of the maximum span-wise temperature (T_{max}) from the temperature rise across the combustor. Additionally, the

profile factor describes the deviation of the average span-wise temperature (T_{avg}) from

the temperature rise across the combustor.

$$Pattern\ Factor = \frac{T_{max} - T_3}{T_3 - T_2}$$ Equation 2.9

$$Profile\ Factor = \frac{T_{avg} - T_3}{T_3 - T_2}$$ Equation 2.10

Barringer et al. [32] also studied the effects of turbine inlet conditions caused by

combustor pressure exit profiles relative to the survivability of turbomachinery

components. Using the same AFRL blowdown facility discussed above, Barringer et al.

[32] established a number of combustor pressure exit profiles shown in Figure 2.27. The

pressure gradients developed towards the OD were formed from the dilution of film

cooling air injected into the flow along the wall. This momentum flux from the upstream

film cooling was controlled generating the numerous test cases. The discrepancy in

pressures moving from OD to ID is explained by the need to maintain a core flow

pressure loss. The total pressure of cooling air injected through the OD surface must be

larger than that of the core flow in order for it to spread along the OD wall. Without the

pressure loss moving from OD to ID the cooling air would become stagnate at the

injection site and not continue to spread along the desired surface.
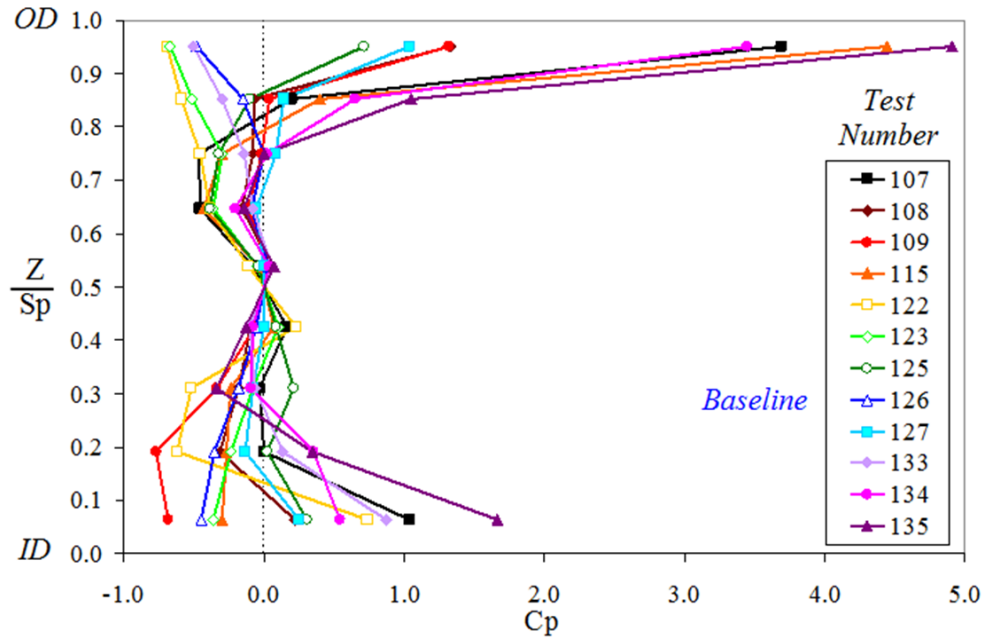
Figure 2.27. Combustor Exit Pressure profiles generated from differences in cooling air momentum flux [32].

Looking at the combustor exit pressure profile as a function of non-dimensional pressure, Barringer et al. [33] clearly show the profiles' dependence on the amount of upstream film cooling air injected through ID surface in Figure 2.28. The greater percentage of cooling flow injected leads to greater skews in the combustor exit pressure profile. Each profile maintains a vertical appearance at the OD through the mid-span due to the amount of dilution within the core flow. The more vertical stance of the profiles indicate that mixing has been effective within the combustor.
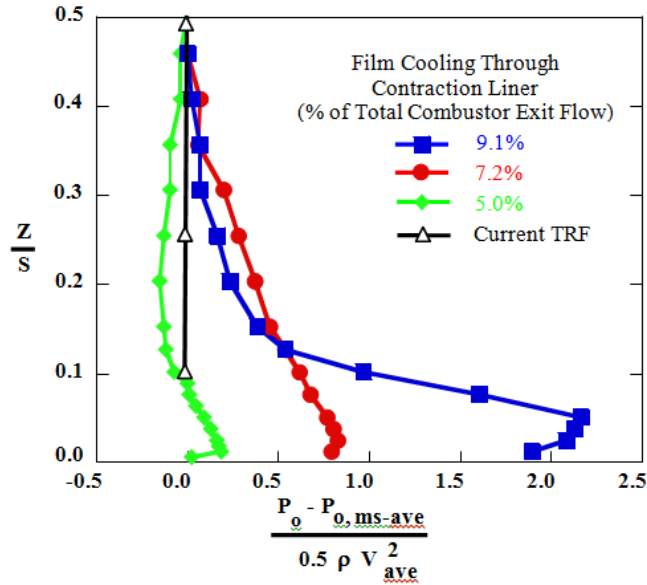
Figure 2.28. Combustor Exit Pressure profiles with increasing amounts of film cooling air [33].

When comparing both exit temperature profiles and exit pressure profiles side by side Barringer et al. [34] concluded that in the radial direction, both profiles appear uniform from ID to mid-span. When film cooling air is injected upon the OD wall however, severe gradients appear in both profiles due to the lack of dilution among cooling air and the relatively hot core flow.

(a)   (b)
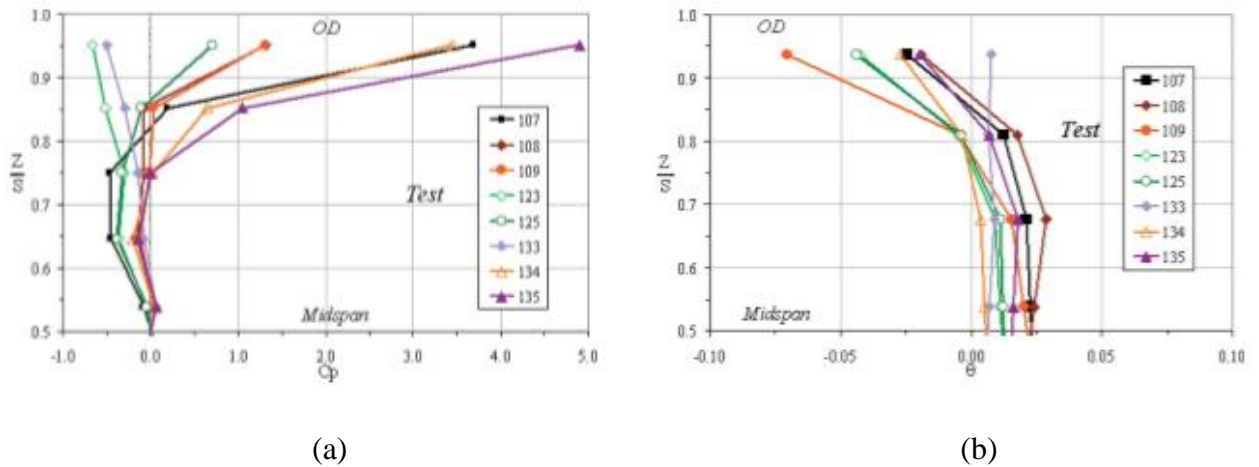
Figure 2.29. a) Combustor exit pressure profiles and b) Combustor exit temperature profiles with cooling air injection along the OD wall [34].

Film cooling schemes within the main vane passages have not been implemented on either the AFRL or AFIT UCCs. Exit pressure profiles will help to characterize the mixing of core and cavity flows within the vane passages and indicate where faster moving flows are present. Mawid et al. [35] used CFD to select an optimal vane design and configuration among three proposals shown in Figure 2.30. The differences in vane design involve the shape of the radial vane cavity used for extraction of hot combustion products from the circumferential cavity. The study was used to predict exit temperature profiles using liquid JP-8 fuel sprays.

(a)   (b)   (c)
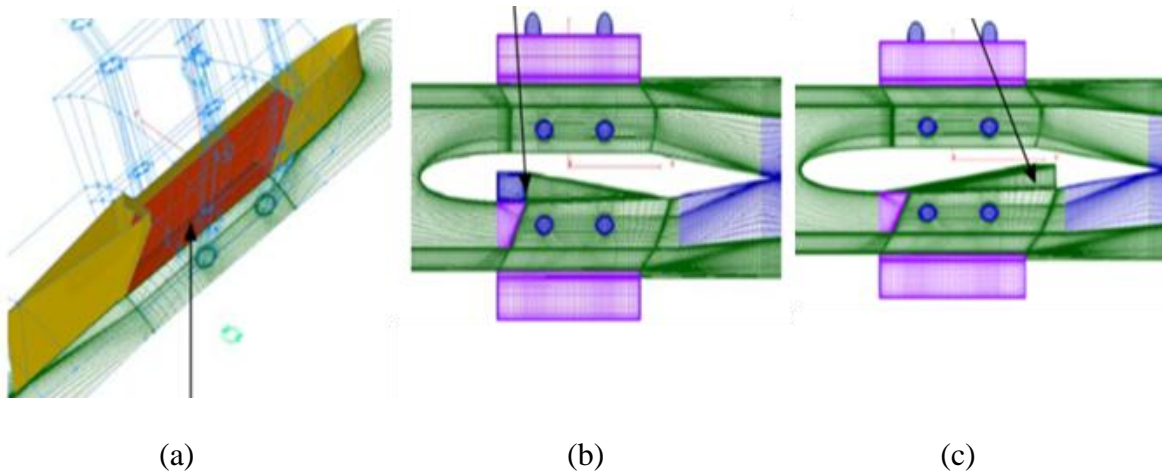
Figure 2.30. RVC configurations: a) rectangular, b) backward facing step, and c) forward facing step [35].

The CFD results in Figure 2.31 show different temperature profiles forming downstream of the radial vane cavities and highlights the importance of radial transport rates of hot combustion products into the core flow. Mawid et al. [35] concluded that the rate of transport for combustion products into the core flow is a function of the radial vane cavity size and shape. The radial vane cavity helps to shape the shear layer that forms among the circumferential and core flows. The backward facing step (Figure 2.30b) delivered the most desirable exit profile per Samuelson [31] and was utilized by

Zelina [10]. The downward angled parallelogram is responsible for generating the mixing of the two flow streams and contributes greatly to the exit temperature profile shape. The experiment of Mawid et al. [35] supports the idea that unique hot spots are formed for a given vane design. The computed temperature profiles show skews toward the outer and inner diameter walls of the exit plane.
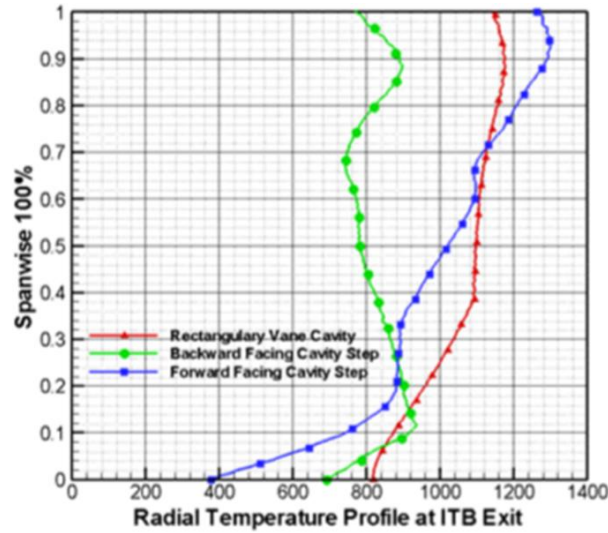
Figure 2.31. Exit temperature (K) profiles for three vane configurations [35].

2.6   Limitations of Previous Work

Having studied the work performed with the sectional UCC models studied at AFIT as well as the full-annular models at both AFIT and AFRL, further research is still necessary to fully characterize the operational capabilities of the UCC concept. With regards to the AFIT full-annular model designed by Wilson et al. [5], a study of the resulting Rayleigh losses associated with higher (closer to Mach 0.8) exit Mach number flows has not been performed to date. Improvements to the laboratory set-up will allow for increased fuel mass flow rates at the 70/30 flow split condition to validate Wilson's

[5] conclusions. Higher fuel flow rates should generate higher exit Mach numbers and consequently more representative Rayleigh pressure losses.

In addition, an emissions analysis of the AFIT UCC has yet to be performed. Emissions results will supplement the understanding of the overall combustion efficiency, identify locations of maximum heat release, and validate exit profile shapes. Lastly a characterization of the AFIT UCC's exit temperature and pressure profiles is needed. Analysis of the exit profiles' pattern and profile factors will show sensitivities to different UCC operating parameters such as cavity equivalence ratio and core/cavity flow split distributions. These profiles will help to identify needed changes to the hybrid vane design in achieving optimal profile shapes.   Accomplishing these three studies will satisfy the research objectives of this report shed light upon the necessary improvements to the AFIT UCC and other future test models.

III. Methodology

Previous efforts developed the hardware to investigate a full annular UCC. The current effort is focused around quantifying the design space for the UCC. Several goals are pursued as part of this effort including expanding the stability curve for efficient combustion in the high g cavity. Other goals focus on understanding how the equivalence ratio, the g-load and the flow split between the core and cavity flow impact the combustion dynamics. Understanding these effects will be determined by quantifying the characteristics within the cavity, but even more so at the exit plane of the UCC system.

To quantify these effects, several upgrades were needed to the AFIT UCC. This started with upgrades to the surrounding COAL Lab support equipment to provide higher flow rates to the combustor and to control the data acquisition. The primary enhancements, though, stemmed from the addition of significantly more instrumentation for the rig. These included probes to quantify and characterize thermal and pressure exit profiles, facility pressure measurements to quantify overall system losses and Rayleigh losses, and integration of a new emissions system to understand combustion efficiencies. This chapter outlines the new supporting hardware and control mechanisms, documents the upgrades made within the COAL Lab, and describes the implementation of new test and measurement equipment. Furthermore, this chapter quantifies the uncertainty of results and outlines the testing for each research objective. Lastly, this chapter introduces the design of an upgrade to the AFIT UCC to be more structurally sound and enhance the capability of the facility.

3.1. AFIT Full Annular UCC

Wilson's [5] AFIT UCC design was predicated off of the nominal flow

requirements for a typical jet engine combustor with the specific flow characteristics as

would be implemented in an axial scheme depicted in Figure 3.1. These requirements

included an inlet Mach number of 0.35 at a swirl angle of 35°and an exit Mach number of

0.7-0.8 at a 70° swirl angle. The swirl angles are achieved via the leading and trailing

edges of the hybrid vanes (green). The primary combustion zone (red) is housed by the

circumferential cavity that moves in and out of the page about the hybrid vane centerbody

which channels the core flow. The secondary combustion zone (purple) occurs within the

hybrid vane passages of the UCC centerbody.
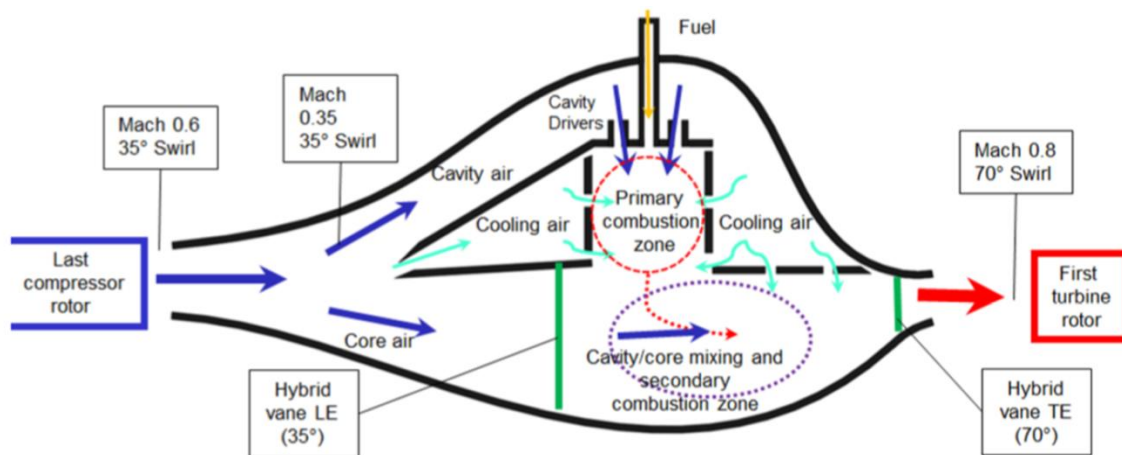
Figure 3.1. AFIT UCC flow path with key flow parameters [5].

3.2. UCC Core, Cavity, and Cooling Air Flow Paths

The AFIT UCC was designed to accommodate 0.45 kg/s of air with a 70/30

core/cavity flow split with independent core, cavity, and cooling air flow paths as shown

in Figure 3.2. Having three separate flow path configurations enables independent

control of each flow path which enables holding either the cavity or core flow constant

while varying the other to study the impact of each parameter. The AFIT UCC laboratory set-up differs from the conventional common air source scheme that would be found in a commercial axial combustor where air comes from a single up-stream source. The three separate streams of air are manipulated throughout UCC operation and each flow path maintains a unique UCC injection as shown in Figure 3.2.
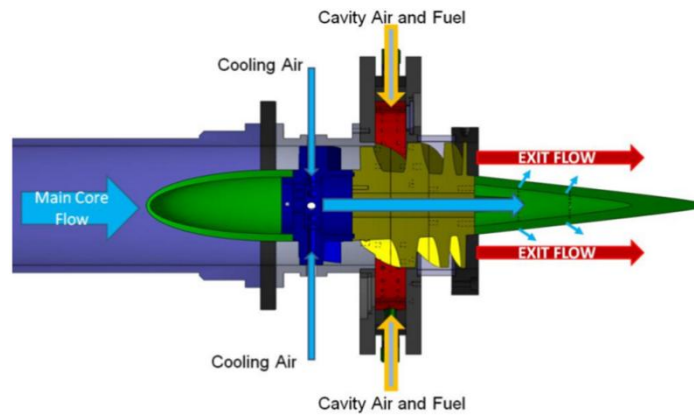
Figure 3.2. Three AFIT UCC flow paths with independent sources [5].

Starting with the core air flow path, the Ingersroll Rand H50A-SD compressor installed by Parks [17] provides up to 1 kg/s of atmospheric pressure air or a maximum of 0.1 kg/s at 862 kPa. The structure housing this compressor seen in Figure 3.3 is piped to the COAL Lab East wall via a 6,895 kPa storage tank and 3.81 cm stainless steel pressure tubing. This compressor is supplemented by two Ingersroll Rand vertical dryers to remove any air condensation generated while compressing the air. This system serves as the main source for the UCC core air and is operated solely by COAL Lab operators.

Additionally, both the cavity air and cooling air supplies begin with two AFIT 50 horsepower Ingersroll Rand compressors located on the south side of AFIT building 644 which fill the AFIT compressor tanks shown in Figure 3.3. The AFIT compressor tanks are used by the broader AFIT research community and their use is not exclusive to

COAL Lab operators. The 50 horsepower compressors provide air at a maximum of 0.15 kg/s and are plumbed in to the COAL Lab via the adjacent laboratory through the COAL Lab South wall with a single 3.81 cm stainless steel pipe.

Figure 3.3. COAL Lab external support equipment.

Continuing the flow paths from the three external COAL Lab sources, the three 3.81cm stainless steel pipes are converted to brass pipes once inside the COAL Lab, and the flows are piped into the valve system shown in Figure 3.4 on the COAL Lab's North wall. A typical flow set-up utilizes the COAL Lab compressor for core air flow and the two AFIT facility compressors for cavity and cooling air flows. Flow from the exclusive COAL Lab compressor passes through the valve system and is sized up from a 3.81 cm line to a 7.62 cm line. Flow from the AFIT facility tanks is split from a single 3.81 cm line to a 3.81 cm line and a 1.91 cm line to support the cavity and cooling flows respectively.
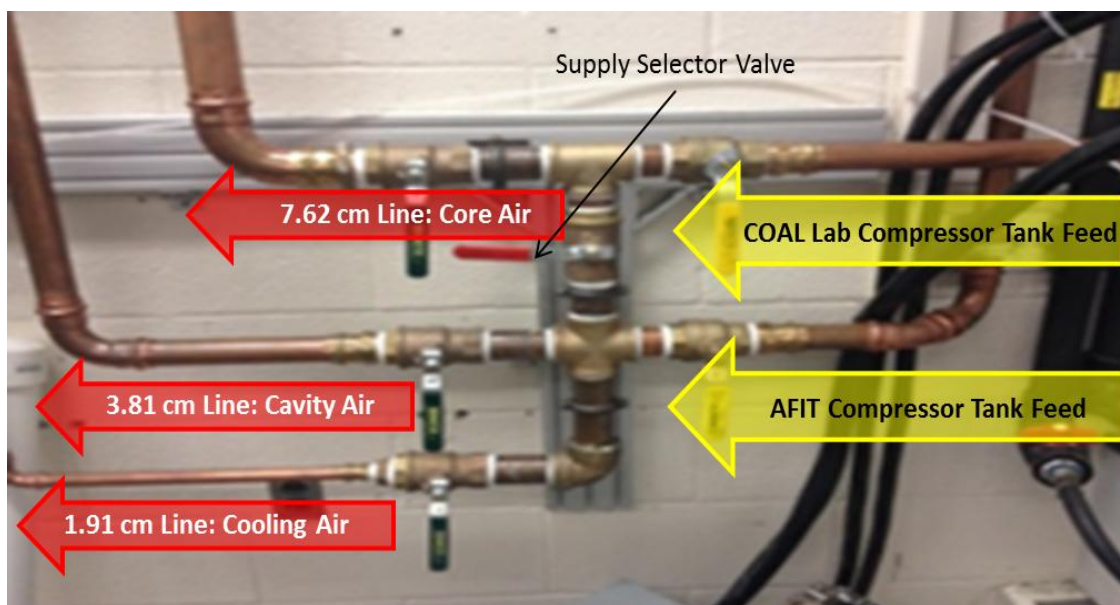
Figure 3.4. COAL Lab air supply valve system.

However, there are situations where the AFIT facility compressors are in use by additional AFIT research laboratories. In this situation, COAL Lab operators use the valve system to manipulate flow so that it is taken only from the COAL Lab external tank described above. This is done by closing the AFIT facility tanks' supply valve and opening the red supply selector valve so that flow from the COAL Lab compressor could feed the two smaller lines. The trade-off here is the limited amount of constant air supply and reduced UCC run-time.

From the valve system, the three independent flow lines (7.62 cm, 3.81 cm, and 1.91 cm) remain separate up through their interface with the UCC. Each flow line is outfitted with the same flow control equipment, sized appropriately for each size line. This equipment included (in order of the flow path direction) an air-powered solenoid valve, pressure regulator, flow meter, and flow control valve as depicted in Figure 3.5. Flow through the 7.62 cm core flow line is controlled with a Flowserve MaxFlo 3 control valve rated to a maximum flow rate of 0.6 kg/s. The 3.81 cm line also uses a FlowServe

59

MaxFlo 3 control valve capable of 0.3 kg/s and the 1.91 cm line uses a Badger control valve capable of 0.03 kg/s. The line pressures needed to support the desired mass flow rates are achieved using a Fisher 99, Fisher 299h, and a Cashoo pressure regulator for reducing the pressure within the 7.62 cm, 3.81 cm, and 1.91 cm lines respectively. These regulators step down the pressures from their respective sources to the pressures required for the desired mass flow rates.
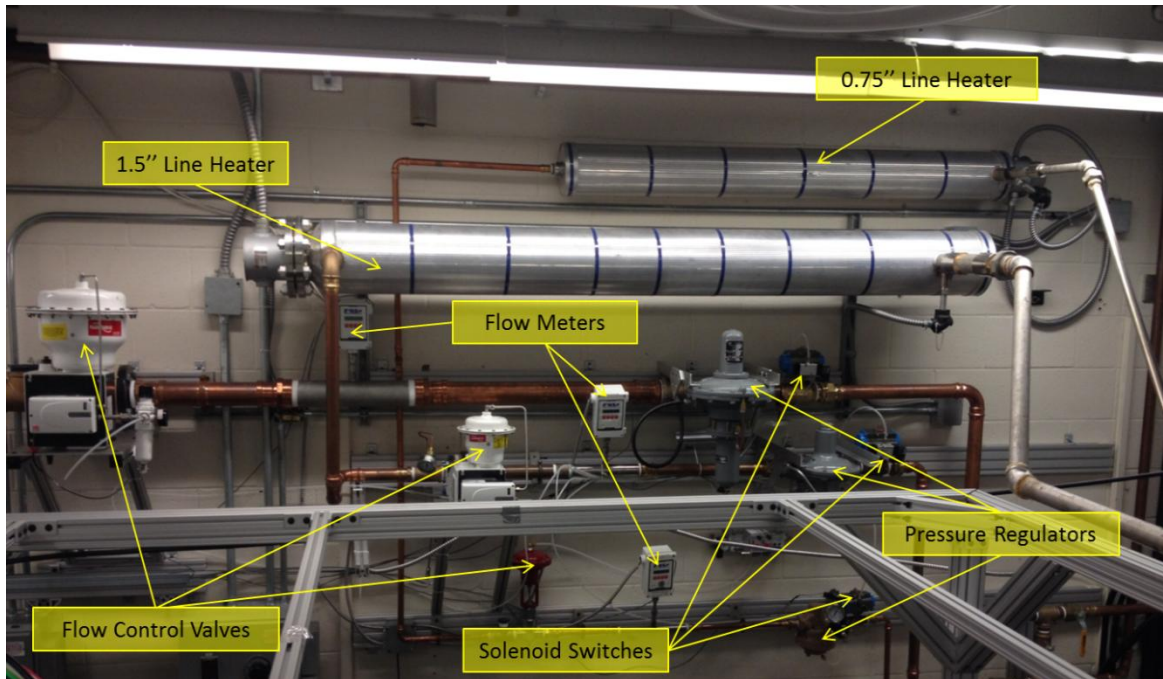
Figure 3.5. COAL Lab Air flow control equipment

The desired mass flow rates are established by the operator for each respective line. The mass flows passing through the lines are measured using FT2 Fox Thermal Instruments flow meters which also serve as the calibration for the flow control system. The flow meters maintain a manufacturer's validated accuracy of +/- 1% of the actual measured values. The flow meters are wired to three Eurotherm 2404 PID controllers which interface with the control station's LabVIEW [36] program. Operators use the LabView GUI to send 0-5 volt (DC) set point signals from the control station to the

Eurotherm PID controllers. The PID controllers then relay a 4-20 mA signal to the

FlowServe and Badger control valves. The flow meters measure the flow passing

through the line by the control valves and transmitting a 4-20 mA signal back to the PID

Controllers which then display the actual flow rates on the Eurotherm controllers in

comparison to the set-points. The ability to maintain independent flow control through

all three lines individually enhances the operator's ability to better characterize the AFIT

UCC. The entire three stream air flow set-up discussed above remained identical to that

used by Wilson [5].

3.3   UCC Fuel Flow Path

Control and manipulation of the AFIT UCC fuel mass flow rate is significant in

that although a variety of cavity equivalence ratios may be achieved for a particular bulk

mass of fuel and air it is necessary to perform studies at different bulk fuel flow masses at

the same cavity equivalence ratio. This is highlighted by insufficient fuel flow

experienced by Wilson [5] when trying to achieve more representative exit Mach

numbers for a Rayleigh loss sensitivity analysis. The fuel mass flow limitations of the

AFIT UCC prohibited the analysis from exploring losses at the 70/ 30 mass flow split

where the proper cavity equivalence ratio could not be achieved therefore limiting the

exit Mach condition. Experimental testing by Wilson [5] revealed that the controllers

could not hold steady inputs pasts 55 SLPM and fluctuations from ±1-3 SLPM were

witnessed up to 60 SLPM. These fuel flow limitations prevented high cavity equivalence

ratios (1.5-2.0) for high cavity flows and therefore, a lack of high fuel flow rate limited

the air flow that could be utilized by the UCC. The highest achievable inlet Mach number

was 0.045 which falls short of the traditional axial combustor inlet Mach number of 0.3. Hence, the highest achievable cavity equivalence ratio was 2.02 at an air mass flow split of 80/20 (9.72 kg/min total air mass). Changes discussed below were made to remedy the limitations experienced by Wilson [5].

The propane burned within the UCC cavity is stored external to the COAL Lab in the AFIT gas tank barn shown in Figure 3.6. The gas tank barn houses a liquid propane to gas propane generation station. The liquid propane is stored in four 568 liter tanks at 550 kPa. The four tanks are plumbed on two separate gas generation lines, each line utilizing two liquid propane tanks and are equipped with the same hardware. The upper line shown in Figure 3.6 maintains a manual hand-thrown switch to supply two different feed locations within the COAL Lab. One feed to the UCC and the second feed to support additional research efforts within the COAL Lab. The lower generation line is exclusive to UCC research and the UCC required flow from all four tanks when in use. From the holding tanks, liquid propane is forced through the Blue Moon liquid propane filters and into the electric Zimmerman LPG liquid-to-gas vaporizers shown in Figure 3.6. The vaporizers are rated to support 0.67 kg/min of liquid propane. Lastly, the Concoa gas regulators reduce the gas propane line pressure to a user defined pressure of 550 kPa. The propane gas is plumbed to the North wall of the COAL Lab via two bundled 1.27 cm copper lines. The fuel flow path established to this point remained unchanged from the set-up used by Wilson [5].

Figure 3.6. Liquid propane to gas propane generation equipment inside AFIT tank barn.

Inside the COAL lab, the stainless steel lines are connected to two Swagelok two-way manual valves which supply gas to the UCC flow control box. The lower propane gas line is reduced from 1.27 cm to 0.64 cm and converted into a single black polyethylene plastic gas line. The upper propane gas line is reduced from 1.27 cm to 0.64 cm and subsequently split into two 0.64 cm black polyethylene plastic lines. The three black polyethylene lines are routed to the UCC flow control box where the propane gas is staged for passage into the UCC Cavity.

Within the UCC flow control box the various gases needed for the UCC are configured. This includes the UCC igniter air, igniter ethylene, and the aforementioned cavity propane. The current flow control box configuration maintains a series of six electrical solenoid switches, six filters, and six mass flow controllers where one of each is used for each flow path. Line number one (furthest left in Figure 3.7) supports the igniter air, lines two, three and six support the propane and, line five supports the igniter ethylene. Line four remains not in use for UCC operation.

In the direction of the flow, moving bottom to top, in Figure 3.7, flows are first met by Parker fail-closed, electric solenoid valves. The valves receive a 4-20 mA signal

via an Opto 22 electrical relay circuit controlled by the user via a LabView [36] GUI.

The solenoids are independently controlled by the user and allow passage of the air and

gas flows to the six Pall flow filters. The filter sizes are 70 microns and 0.1 microns to

filter gas flows (both propane and ethylene) and air flow for the igniter respectively.

From the filters, flow passes to the mass flow controllers (MFCs). The three propane

lines utilized type 1559 MKS MFCs rated for 200 SLPM of nitrogen or 72 SLPM of

propane each. The igniter air and igniter ethylene lines utilize two ATLA MKS MFCs

rated for 50 SLPM of air and 13.4 SLPM of Ethylene respectively. The MFCs are wired

to an MKS 647c controller interface mounted in the UCC Operator's control station. The

MFCs receive 0-5 volt DC signals from the 647C interface to hold user defined set

points.
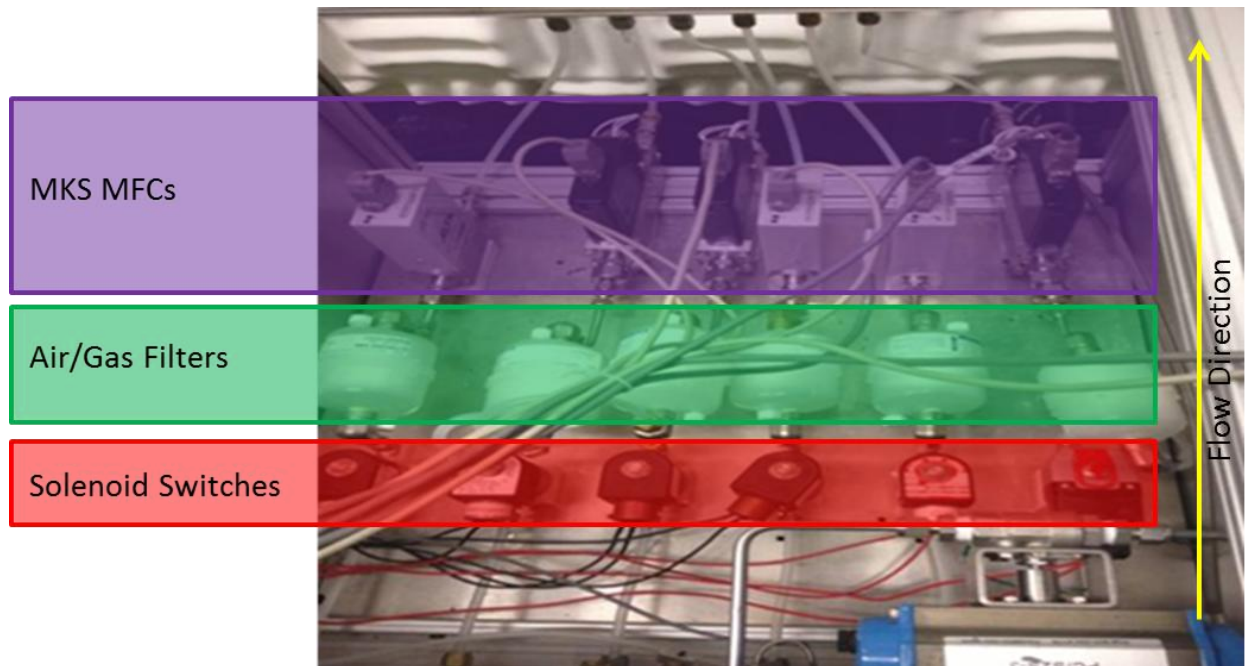
Figure 3.7. UCC Flow control box within COAL Lab.

3.3.1 Fuel Flow Upgrade

The upgrade to three type 1559 MFCs for propane (versus the two type 1559s used by Wilson [5]) was needed to better understand the impact of Rayleigh loss. They were added specifically to allow for more fuel into the UCC to obtain higher inlet Mach numbers to replicate the exit conditions from the last compressor rotor. Wilson's [5] two centerbody designs, TCB and LLCB, were shaped to accept and inlet Mach number of 0.3 and produce exit Mach numbers of approximately 0.5. However, at a core/cavity air flow split of 70/30, Wilson [5] could not flow a high enough fuel flow to achieve the necessary equivalence ratios (1.5-2.0) at high core flows. Therefore, his inlet Mach number was reduced and subsequently he could not obtain these exit Mach numbers. To remedy the lack of available fuel flow seen by Wilson [5], an additional mass flow controller (MFC) was introduced to the set-up.

The addition of the third MKS MFC allowed for three MFCs providing up to 72 SLPM of propane. The third additional controller required different fuel flow plumbing than that used by Wilson [5]. Each controller was now responsible for fueling two injection ports versus three injection ports as seen in Figure 3.8. The three MFCs were clocked so that each MFC feeds two opposing fuel ports around the circumference of the UCC.
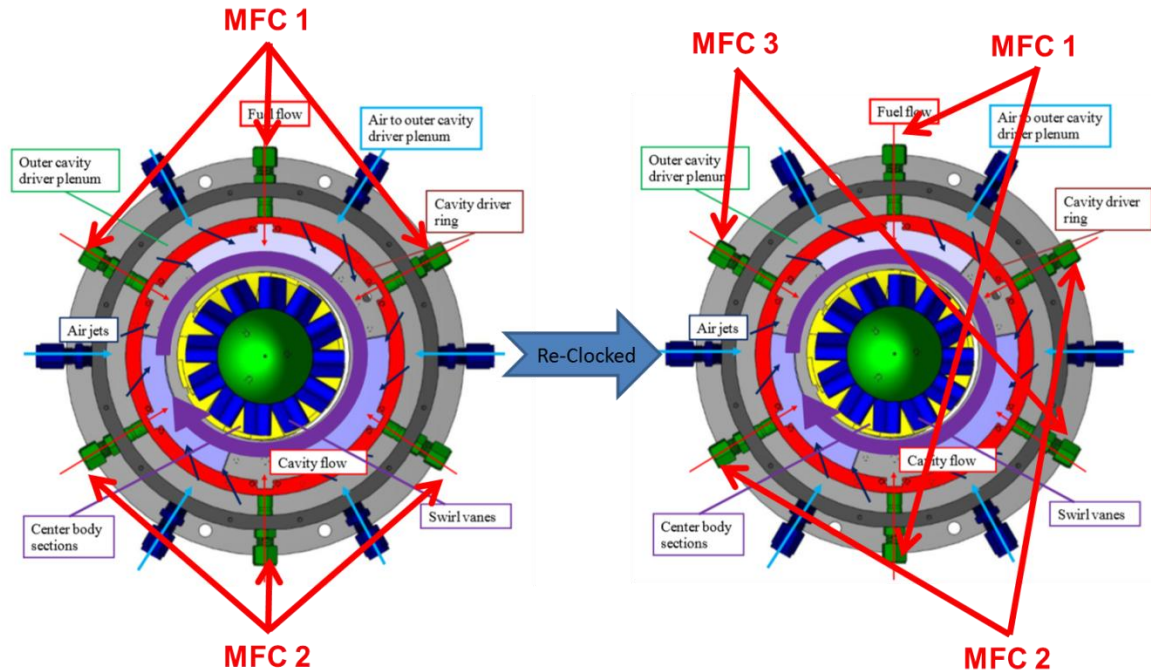
Figure 3.8. Additional MFC solution for lack of fuel flow experienced by Wilson [5].

3.3.2 Fuel Baffle Integration

Results from both Zelina [3] and Wilson [5] have suggested an inverse relationship among g-loading and fuel flow rates. Trends have indicated that as fuel flow rate decreases, g-loading increases for a given air flow. This trend suggests there exists some inhibitor to the tangential flow velocity as fuel flow rate is increased. Specific to the AFIT UCC, the six single jets of fuel injected via the holes within the air injection ring shown in Figure 3.9 create cylindrical plumes of gas within the cavity.   The tangential flow impacts these plumes of fuel like a cylinder in a cross flow as it circulates about the cavity. The impact of the flow upon these cylindrical plumes creates a stagnation point forcing the tangential flow to slow within the cavity as it moves around the pseudo stagnation points.

66
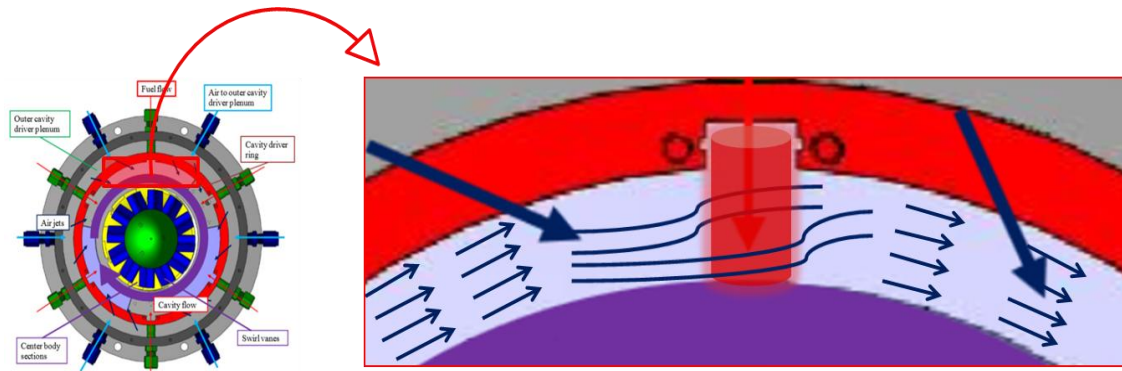
Figure 3.9. Expanded UCC cavity section with movement of swirling flow about injected fuel plume.

To alleviate the slowing of tangential flow around the cylindrical plumes of fuel, a more diffuse injection was necessary. Therefore, Wilson [5] designed the fuel baffle plate shown in Figure 3.10 consisting of eight smaller driver holes that break up the momentum of the single jet of gaseous propane. The use of gaseous propane does not warrant the need for a fuel nozzle leaving enough space between the fuel port and the air injection ring for the baffles to be inserted. Wilson [5] would decipher that operation of the AFIT UCC with the fuel baffles installed yielded challenges.
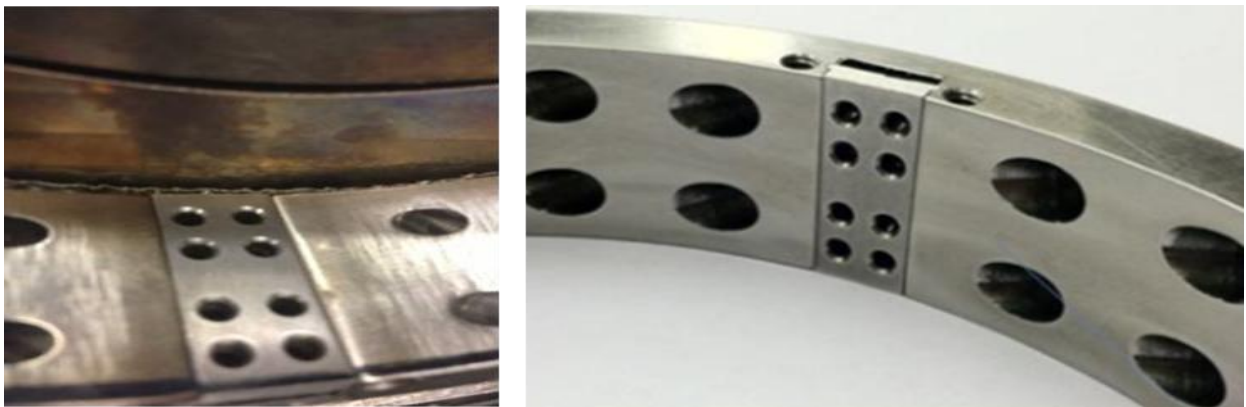
Figure 3.10. Air Injection ring with fuel baffle installed.

The baffles lie within the injection ring and sit just below the fuel injections ports relative to the fuel flow. As fuel began to flow through the injection ports, the collision with the fuel baffles generated a high pressure region of fuel housed between the baffle

and the air injection ring housing. Figure 3.11a shows the gap where this high pressure was housed.

The effects of this high pressure gap caused fuel to divert from passing into the combustor cavity and exit into regions of lower pressure. This pressure release is seen in Figure 3.11 b as fuel exits through a 6-32 socket head cap screw hole of the UCC's front plate. This photograph suggests that although the ends of the gaps shown in Figure 3.11a are sealed within the UCC by UCC's front and rear plates, not enough of a seal existed to divert the fuel through the fuel baffle holes.

(a)   (b)
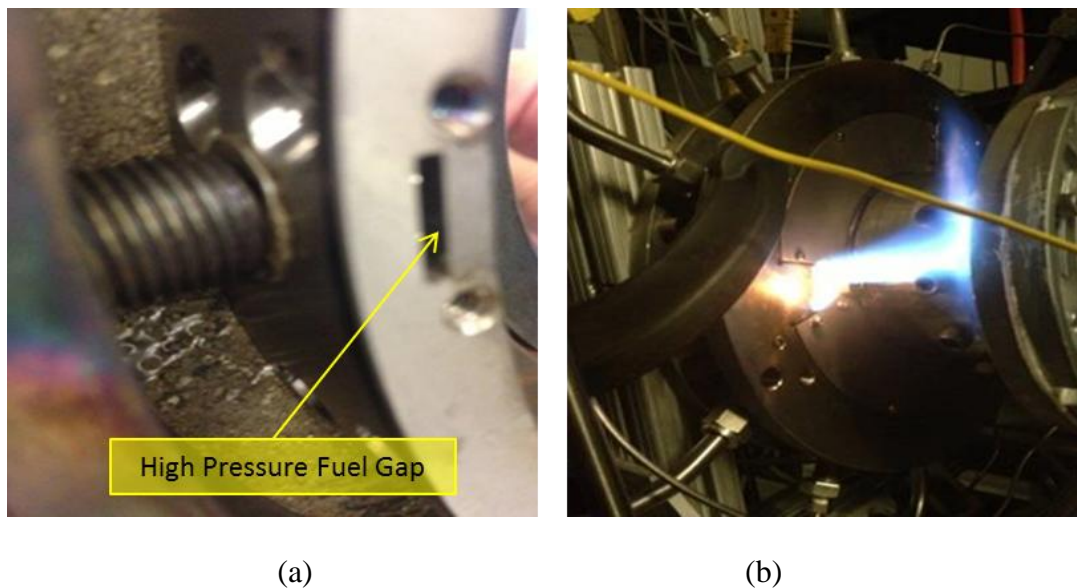
Figure 3.11. a) High pressure fuel gap caused by fuel baffle and b) high pressure fuel release exiting the UCC front plate.

Hence, an impermeable seal was needed to close the ends of the high pressure gaps. Given the heat thriving nature of the UCC cavity environment, Thermiculite, a gasket material, was used to line the walls of the front and rear plates sandwiching the high pressure gaps created by the fuel baffles. The Thermiculite gaskets were cut from a sheet to the exact dimensions of the UCC's front and rear plates, allowing for the UCC's

hardware to pass through. The gasket installation is shown in Figure 3.12 without the air injector ring.
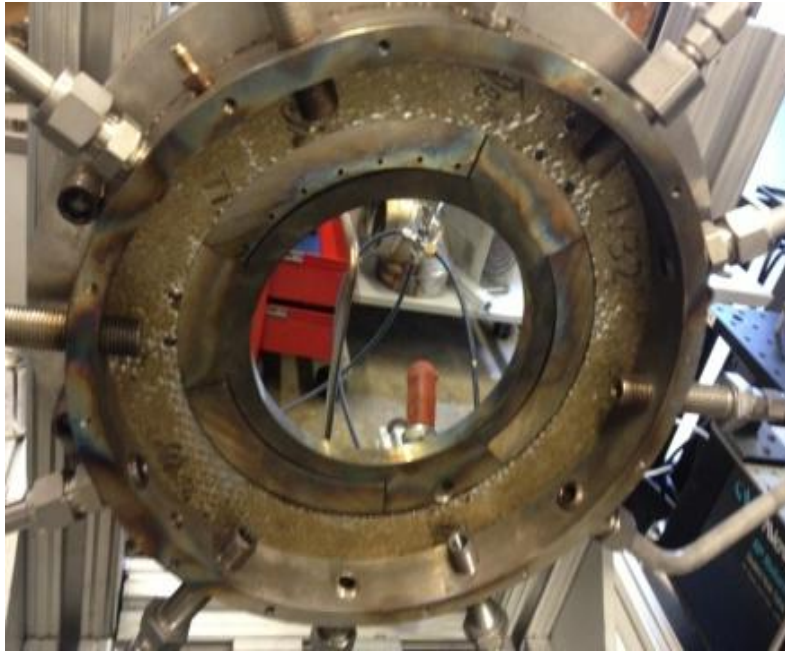
Figure 3.12. Thermiculite ring gasket attached to rear plate.

The solution to this problem was the implementation of a fuel baffle addition seen in Figure 3.13. This piece was designed in part by Wilson [5] and provided a flush gap seal about the six fuel injection ports on the air injection ring. The Hastelloy cut fuel baffle addition sits atop of the fuel baffle and is etched with a fuel receiving divot to divert fuel flow as it enters from the fuel injection port holes. The divot is seen on the top of the baffle addition at midspan in Figure 3.13a. The fuel baffle additions provided the necessary high pressure gap seal and continued to allow steady operation of the UCC.

<center>(a)   (b)   (c)</center>
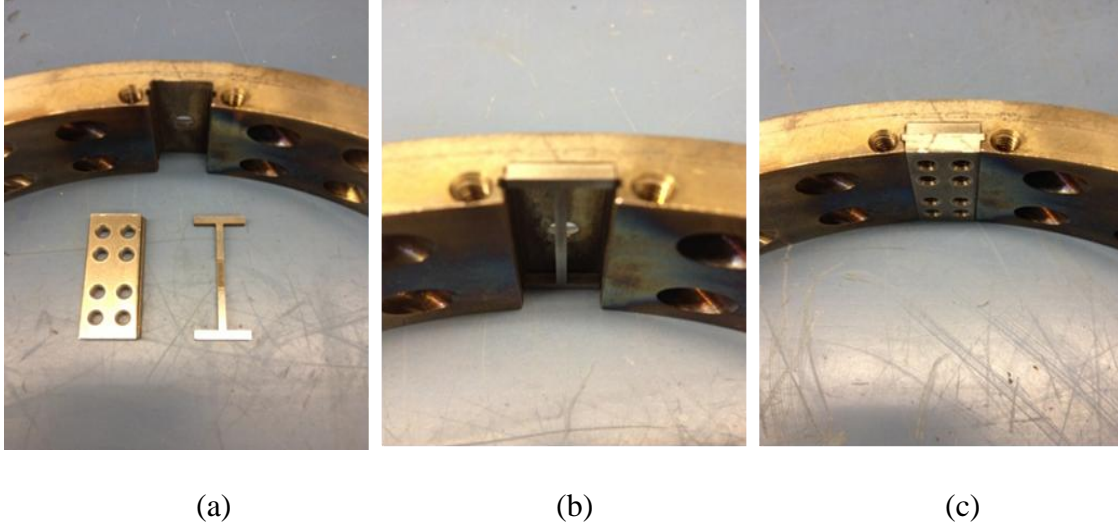
Figure 3.13. a) Fuel injection cavity open, b) with baffle addition installed, and c) with fuel baffle and baffle addition installed.

3.3.3 Calculation of Cavity/Overall Equivalence Ratio

Manipulation of the equivalence ratio was performed by maintaining a set air flow rate and increasing or decreasing fuel flow rates to match a desired equivalence ratio defined by Equation 3.1.

$$\varphi = \frac{\left(\dot{m}_{air}\middle/\dot{m}_{fuel}\right)_{stoich}}{\dot{m}_{air}\middle/\dot{m}_{fuel}} \qquad \text{Equation 3.1}$$

Here the mass flow rate is defined by $\dot{m}$ and the numerator is the ratio of air and fuel mass flow rates at the stoichiometric (*s*) condition which for propane is 15.7. Ratios below 15.7 would be considered lean and ratios greater than 15.7 would be considered rich. The difference in calculating the cavity equivalence ratio versus the overall equivalence ratio with respect to a UCC is changing the mass flow rate of air in the denominator. The cavity equivalence ratio is calculated with just the cavity air mass flow

<center>70</center>

rate and the overall equivalence ratio is calculated using both the cavity and core air mass flow rates.

3.4   Instrumentation

The full annular AFIT UCC is instrumented with 0.16 cm diameter K-type thermocouples and 0.16 cm stainless steel static and total pressure ports at the inlet, cavity, and exit planes. This instrumentation provided the parameters necessary for the calculation of tangential velocity, Mach number, g-load, pressure loss, and temperature rise across the UCC. This section will discuss new instrumentation schemes as well as the instrumentation set-ups at the exit plane used for the characterization of thermal and pressure profiles.

3.4.1   UCC Cavity Instrumentation and Total Pressure Instrumentation Upgrade

Within the UCC cavity and at the UCC exit plane Wilson [5] used 0.16 cm diameter SS tubing for collecting total and static pressure data throughout the UCC. Static pressure measurements involved flush mounting a SS tube piece to one of many instrumentation ports machined into the UCC structure using a Swagelok 0.16 cm male NPT fitting. For total pressure measurements, Wilson [5] pointed the SS tubing into the direction of the flow. This technique yielded acceptable results as total pressure measurements in the UCC cavity at the quarter and center lines were measured higher than the cavity static pressure measurements. The one downside however, was not knowing if the bent SS probe was properly aligned with the direction of the cavity flow.

Therefore, based off a suggestion from engineers at AFRL/RQTC, a design for new total pressure ports was implemented [37]. The new total pressure port design was

71

based off the concept of a pitot tube. Using high strength 0.16 cm hypodermic tubing and an Electronic Discharge Machining (EDM) hole cutter, 0.038 cm diameter holes were cut into the sides of 0.16 cm tubes. EDM holes were cut into the tube sides at precise lengths from the welded tube ends. These precise lengths were measured to provide the necessary quarter and center line total pressure measurements within the 2.54 cm wide UCC cavity.

To implement the new total pressure instrumentation scheme within the cavity, the tubes were inserted into the cavity from wall to wall and then turned until outputting the highest measured total pressure. The tubes were then indexed outside of the cavity so as to document when the EDM hole was directly in the cavity flow path. Figure 3.14 shows the pitot probe style tubes and both total pressure instrumentation schemes. Both schemes were maintained in the UCC cavity to perform an analysis upon the different schemes.

(a)
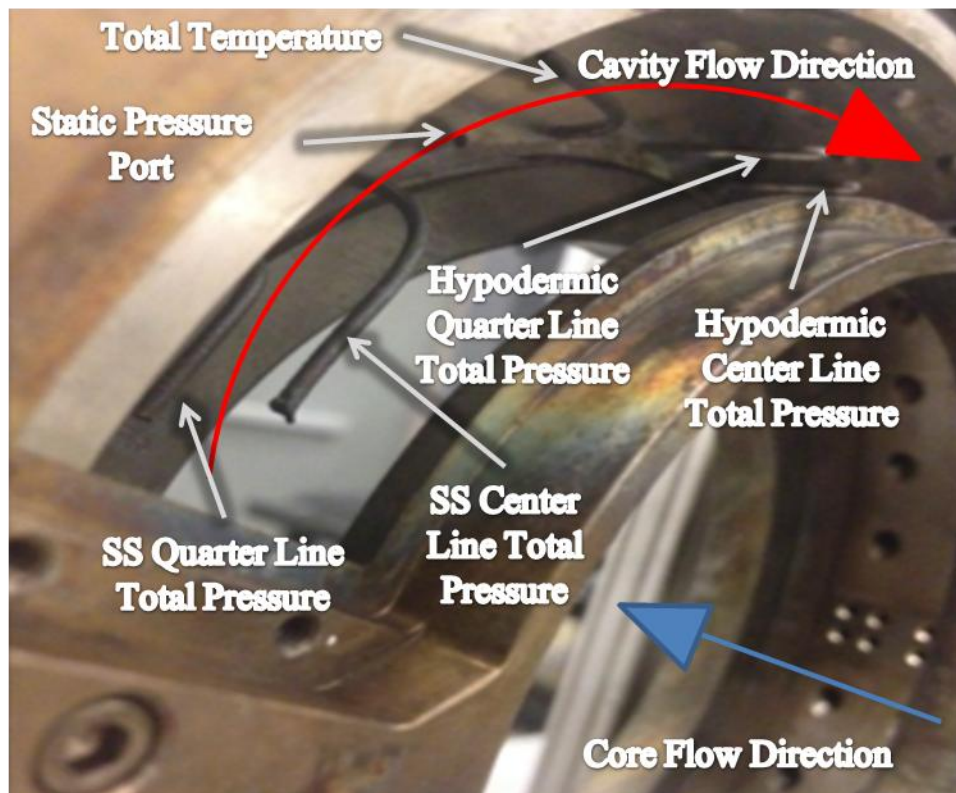
(b)

Figure 3.14. a) EDM holes in hypodermic tubing and b) total pressure instrumentation schemes used within the UCC cavity.

3.4.2   UCC Exit Plane Instrumentation

Instrumentation at the UCC exit was structured to capture the effects of swirling flow exiting the six centerbody hybrid vanes associated with the LLCB and TCB.

73

Because exiting flow is swirling, characterization of pressure and temperature in the radial as well as circumferential directions was desired. The full exit plane instrumentation ring consisted of 21 total ports with seven ports across three 60 degree circumferential spans.

Both K-type thermocouple and EDM hole style total pressure ports were used to characterize the exit profiles. With consideration to thermal profiles, to capture both circumferential and radial distributions, the instrumentation was positioned in two different configurations of seven port sets about the exit instrumentation ring. The first set varied the location of the seven probes across the circumferential direction. A 2.5 cm span exists along the centerbody exit vanes from OD to ID and the incremental variation in height was 0.32 cm. The second configuration maintained the entire seven port set at the same radial height in order to characterize circumferential variations including effects due to vane wakes. These two configurations are pictured in Figure 3.15b.

<div align="center">(a)   (b)</div>
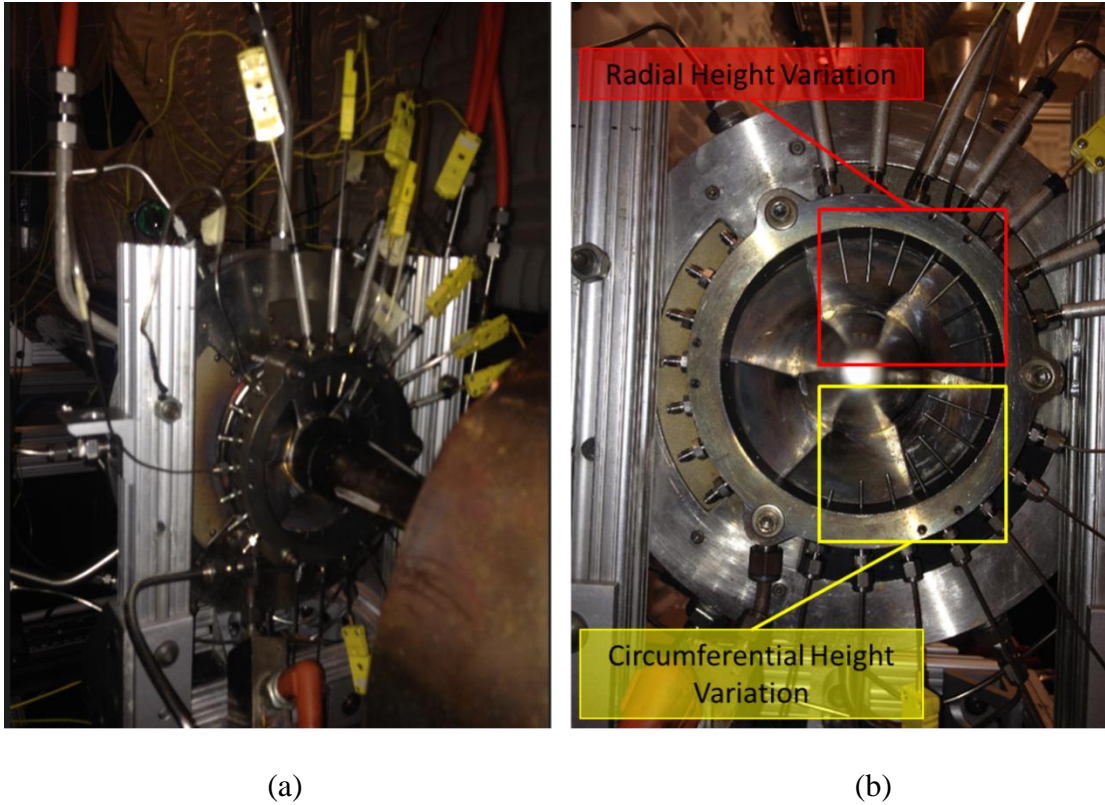
Figure 3.15. a)Thermal exit profile instrumentation and b) radial and circumferential instrumentation configurations.

In regards to the total pressure port instrumentation at the exit plane, the pitot probe styled tubes were utilized. One seven port set consisted of five pitot tubes, all the same length, with EDM holes machined out at different radial heights in 0.32 cm increments from 0.98 cm to 2.26 cm as shown in Figure 3.16a. Thus, total pressure port tubes did not span the entire gap from OD to ID. Two ports on the seven-port set were utilized differently; one for an exit span static pressure measurement and another for a bent SS total pressure port to be used for comparison in instrumentation schemes as discussed in Section 4.2.3. This total pressure port configuration set-up can be seen in Figure 3.16b. A radial height variation set-up of total pressure ports was not used for reasons discussed in Section 4.2.1.

(a)
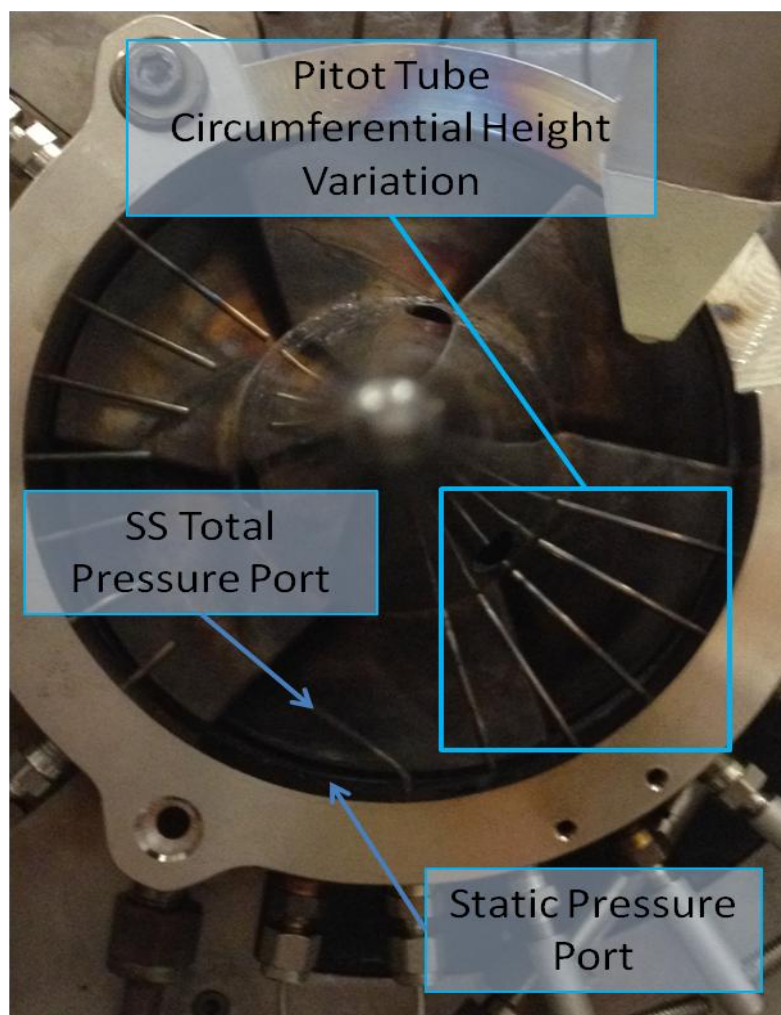
(b)

Figure 3.16. a) EDM hole location from end of tube and b) total pressure port instrumentation at UCC exit plane.

To hold the total pressure pitot style probes in place at the exit plane as shown in Figure 3.16b, a unique solution was designed to allow the probe EDM holes to be aligned with the flow path while remaining at the set vertical position. In the past, this had been done using the two-piece Swagelok ferrule system. This two piece system, once exposed to heat, created a number of configuration issues. The probes became locked in position as ferrule sets would weld themselves to the probes. This became problematic in re-configuring the instrumentation at the exit plane. Therefore, the probe stands shown in Figure 3.17 were design and utilized. The probe housing consisted of 0.64 cm diameter SS tubing cut in 2.5 cm increments. A 10-32 screw tap was inserted on the side of the housing to allow for insertion of a 10-32 plunger screw. Additionally, the bottom of the housing was tapped to fit onto the 0.16 cm male NPT fittings which encompass the exit span instrumentation ring. The plunger screw consisted of a spring loaded ball bearing tip which would depress to allow room for insertion of the pitot tube style total pressure probes. The spring loaded ball bearing applied enough tension on the probes to hold them in the correct vertical position as well as allow the probes to be twisted into the flow path direction. This assembly provided excellent probe flexibility in the harsh thermal environment at the exit plane.
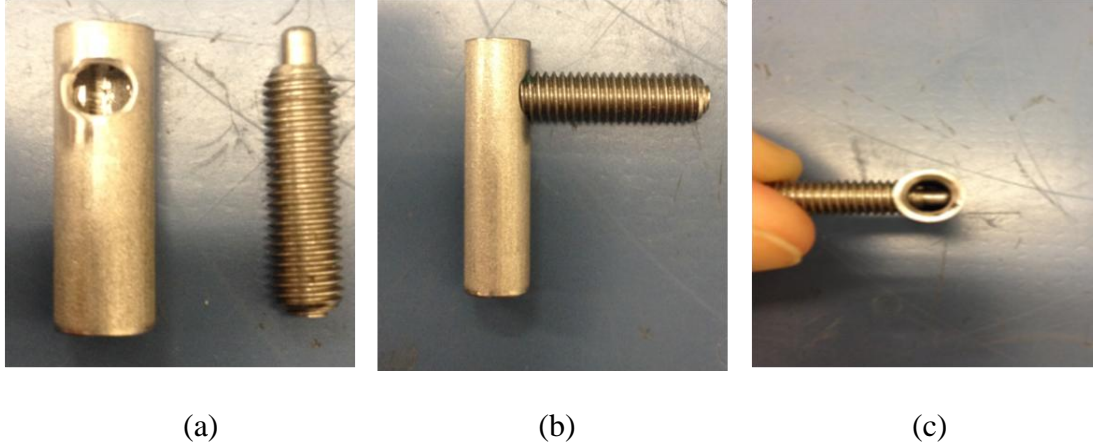
Figure 3.17. Pitot tube style probe holder assembly with a) probe housing and plunger screw, b) plunger screw inserted into the probe housing, and c) ball bearing tip in the probe housing.

3.4.3 Calculation of Cavity Mach Number, Tangential Velocity, G-load, and Rayleigh Loss

With instrumentation for total and static pressure as well as total temperature within the cavity (Figure 3.14b), calculation of the cavity Mach number and cavity tangential velocity are possible via Equations 3.2 and 3.3.

$$M = \sqrt{\left(\left(\frac{P_T}{P}\right)^{\gamma-1/\gamma} - 1\right)\frac{2}{\gamma-1}}$$
Equation 3.2

$$V_{tan} = M\sqrt{\gamma RT}$$
Equation 3.3

The total pressure is represented by P_T, static pressure by P, ratio of specific heats by $\gamma = 1.37$ for reacting flows and $\gamma = 1.4$ for non-reacting flows, universal gas constant by $R = 287$ J/kg/K, and the cavity total temperature by T. The cavity g-load then utilizes the tangential velocity parameter via Equation 2.2. The mid-span radius of the cavity is represented by $r = 6.7$ cm.

Rayleigh loss, defined in Equation 3.5, within the UCC is measured as the difference between pressure losses associated with reacting flow and non-reacting flows. Total pressures at the inlet and exit for both reacting and non-reacting flows are differenced and the result becomes the pressure loss due to heat addition.

$$\frac{P_{Tinlet}-P_{Texit}}{P_{Tinlet}}\bigg|_{Rayleigh} = \frac{P_{Tinlet}-P_{Texit}}{P_{Tinlet}}\bigg|_{Reacting} - \frac{P_{Tinlet}-P_{Texit}}{P_{Tinlet}}\bigg|_{Non-Reacting} \qquad \text{Equation 3.5}$$

3.5 Emissions Analysis

Performing a proper characterization of the AFIT UCC's performance required an emissions analysis. Previous research was not performed in this area with the AFIT full annular UCC. However, the AFIT COAL Lab did support an emissions analysis infrastructure which required the design and installation of additional components to fully support a sound emissions analysis.

3.5.1 Emissions Analysis Infrastructure

The key pieces of equipment already in place in the COAL lab were the California Analytical Instruments emissions analyzer machine (CAI) and the Mokon oil pump used as a cooling mechanism to supply heated oil to and from an emission probe. The CAI and its integration into the COAL Lab operating station was written in full detail by Conrad [38]. The Mokon oil pump was set to an operating temperature of 450 K (350°F) in order to preserve the correct specimen quenching temperature of 440 K in the oil return line. With the analysis equipment in place, the emissions infrastructure required specimen probes, a heated line extension, a high temperature solenoid switch, and a horizontal traverse.

Beginning with the probe design, emissions specimens were sought at two distinct locations at the exit of UCC; directly behind a single centerbody vane exit to capture the burning process happening within a vane passage and downstream in the UCC's exit flow path to gather an aggregate of specimens emitted from all six centerbody vane exits. The desired measurement locations are shown in Figure 3.18.
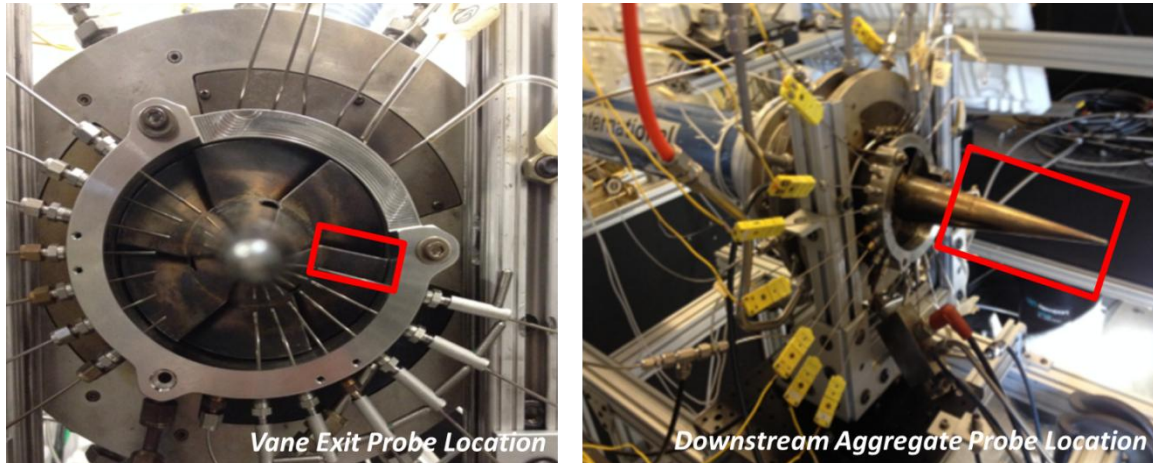
Figure 3.18. Desired emissions specimens collection locations.

The probe design for the collection of emissions specimens at each location was unique. Beginning with the centerbody vane exit probe, a single collection channel was desired to collect specimens from across the entire vane exit span. To do this, the single channel probe was mounted to a horizontal traverse. The single channel probe was designed to allow for the optimization of specimen quenching at 460 K [39]. Quenching was necessary to remove any latent heat which would allow for combustion reactions to continue in the passage leading to the CAI emissions analyzer. In addition, the probe had to be properly choked so as to allow enough of the specimen sample to reach the CAI emissions analyzer. A probe orifice size of 0.07 cm was needed to provide the proper amount of quenching and choking [40]. The probe shown in Figure 3.19 was

manufactured by AFRL/RQTC and supports cooling oil temperatures of 480 K and an oil line pressure of 275 kPa. The front tip of the tomahawk style probe is covered in a Thermal Barrier Coating (TBC) capable of withstanding temperatures up to 2200 K.

(a)

(b)   (c)
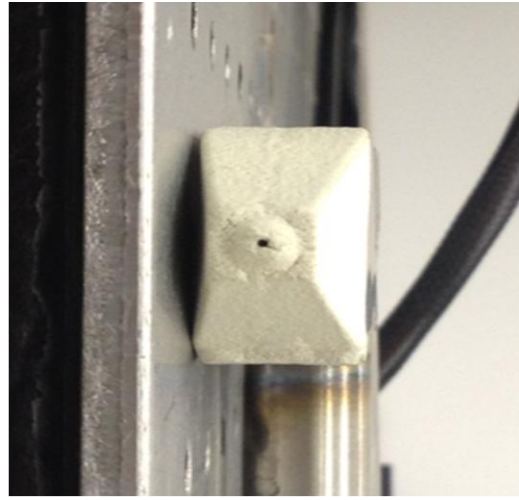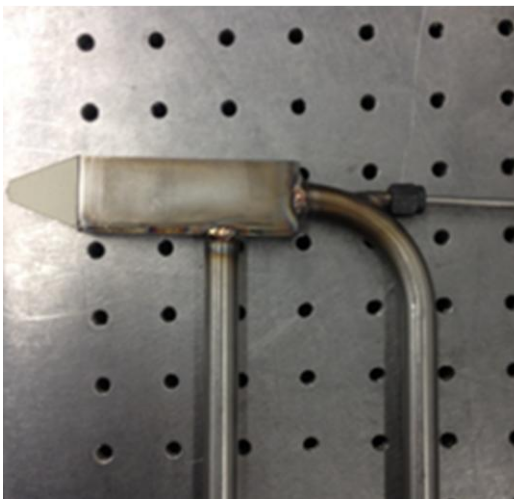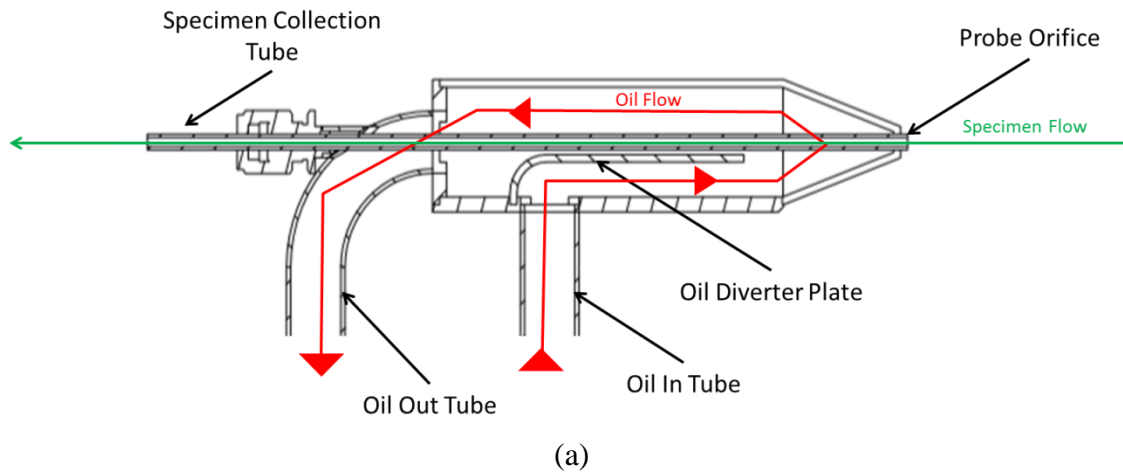
Figure 3.19. a) Single channel probe schematic with oil and specimen flow paths, b) single channel probe with TBC coating at tip, and c) single channel probe orifice size.

The downstream aggregate probe is still under design. It is desired to have a similar tomahawk profile shape only with five channels versus one. The five channels are necessary to allow a collection of specimens across the entire exit span. This five

channel probe will not be traverse mounted and the use of the five channels will allow for an analysis to be performed at discrete locations across the span or collect a bulk average via a switch mechanism.

The switch mechanism shown in Figure 3.20 consists of six high temperature solenoid switches mounted in series. The solenoid switch mechanisms are triggered by 4-20 mA signals generated by Opto 22 electrical relays which will be programmed into a LabView [36] GUI at the operator control station in the COAL Lab. The 6 channel switch was manufactured by AtmoSeal Engineering who builds high-temperature solenoid valves capable of withstanding temperatures up to 505 K at 480 kPa. Each solenoid switch may be opened or closed individually to route the given sample to the CAI. Only one measurement can be routed to the CAI emissions analyzer. Therefore, the operator may manipulate the series of switches to provide emissions analysis at any particular area pending the five channel probe's location.

In order to prevent emissions species deterioration in the lines spanning the distance from the two emissions probes to the high temperature switch location, a heated line bundle (Figure 3.20) containing the six specimen lines from the emissions probes is currently under design. The role of the heated line bundle is to maintain the collected emissions species at 460 K until they arrive at the high temperature switch. If the species are allowed to quench again in the lower atmospheric temperature of the COAL Lab prior to entering the high temperature switch, then the species that are analyzed will not be representative of the emissions species collected at the two probe locations.

Once at the high temperature switch, the species will either be allowed to pass to the emissions heated filter (Figure 3.20) or be purged through the exhaust duct depending

on how the operator has opened/closed the series of switches. The purpose of the heated

emissions filter is to remove any moisture within the sample before it is analyzed. The

moisture filter is heated to 460 K also to prevent further quenching of the emissions

species. From the moisture filter, the emissions species pass into the CAI heated line

extension maintained at 460 K which then follows three separate flow paths to each of

the three separate analyzers described by Conrad [38].
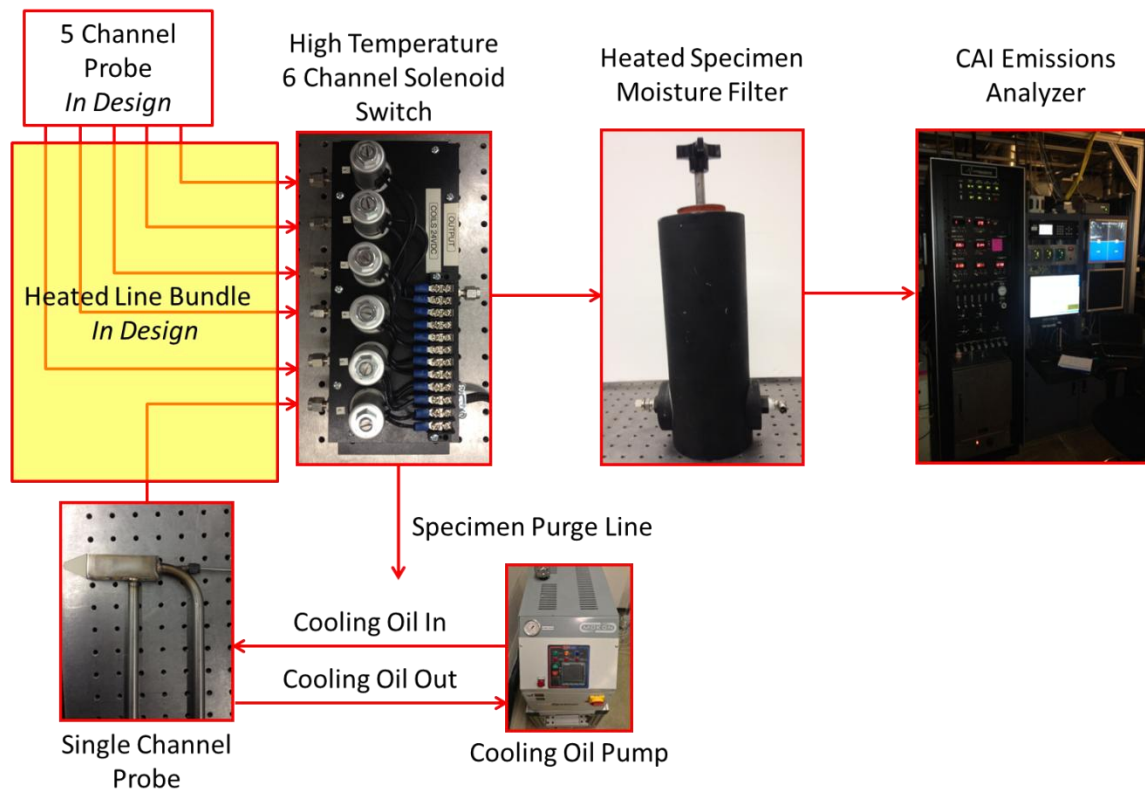
Figure 3.20. Emissions analysis infrastructure within the COAL lab.

3.5.2   Emissions Analysis Hardware Modifications

To allow for the single channel probe to have unlimited access to a single exit

vane span, a new exit plane instrumentation ring was designed and built. The full annular

instrumentation ring shown in figure 3.15b did not allow for the single channel probe to

align directly over a single vane exit. The 2/3 partial exit plane instrumentation ring

shown in Figure 3.21a consisted of 14 total ports across two 60 degree circumferential spans with one 60 degree span removed to allow for emissions probe access at the exit plane. The new 2/3 partial ring provided enough operating space for the single channel probe to operate and supported instrumentation for generating thermal and pressure exit profiles.

(a)   (b)
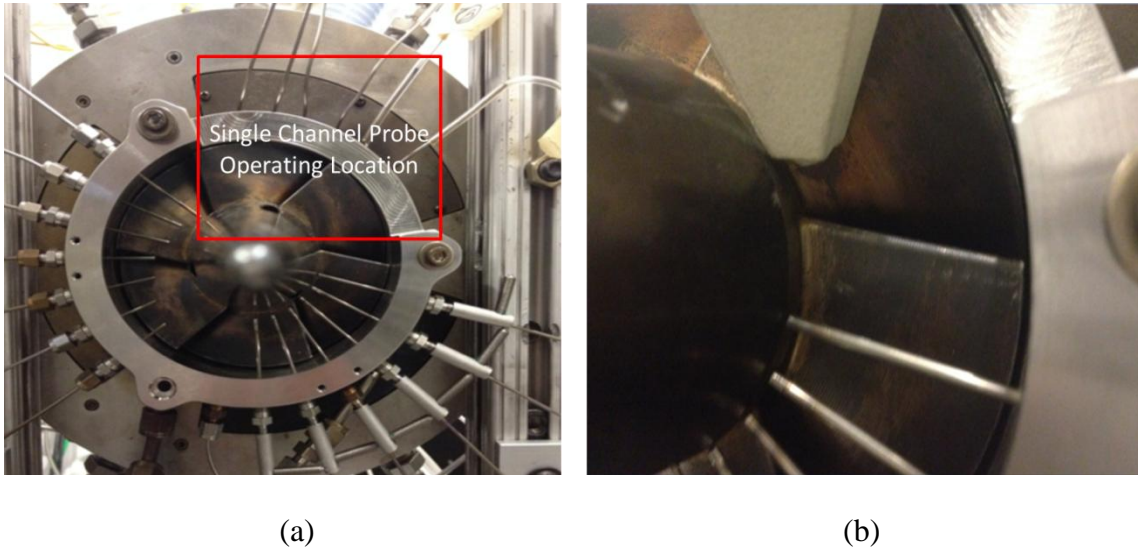
Figure 3.21. Partial 2/3 instrumentation ring with a) single channel probe operation location and b) single channel probe alignment above exit vane.

Finally, modifications to the UCC's surrounding support equipment were made to support a Newport UE41UP horizontal traverse. The traverse was used to run the single channel emissions probe (Figure 3.19) across a single centerbody exit vane spanning 2.54 cm. The traverse support stand was built to move both vertically (perpendicular to the UCC core flow) and axially (parallel to the UCC core flow) moving along stock 8020 type structural members. This allowed for proper placement of the probe and the probe support stand built off the traverse breadboard displayed in Figure 3.22.
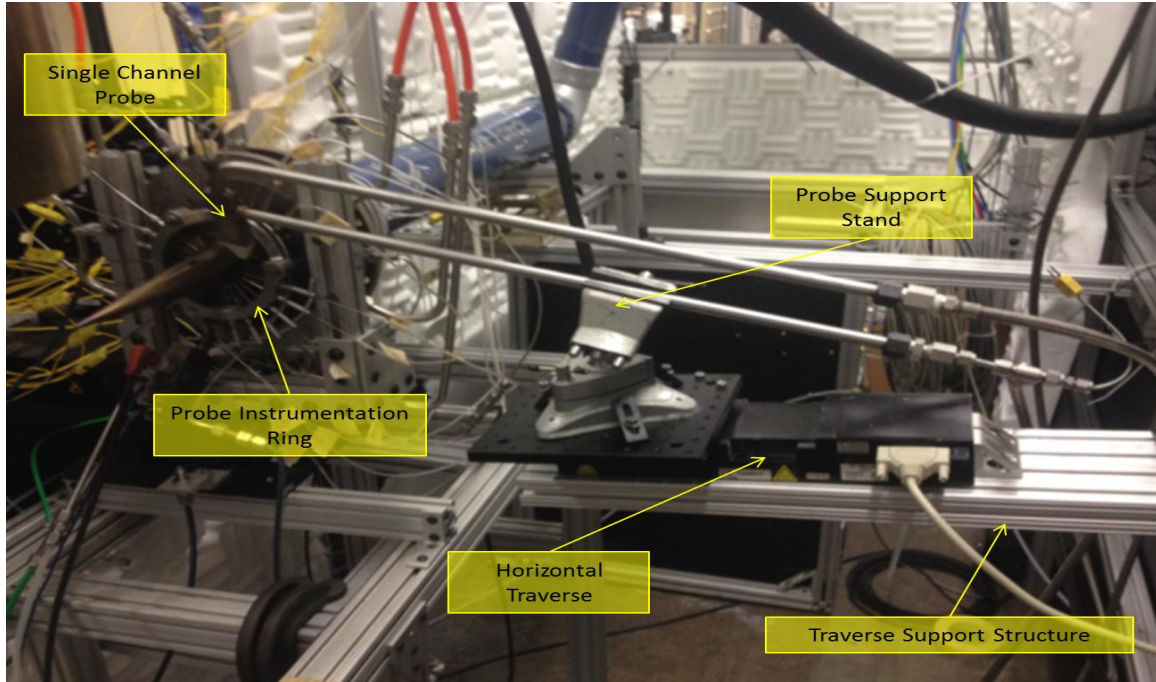
Figure 3.22. Single channel emissions probe implementation.

3.5.3 Calculation of Emissions Index and Combustion Efficiency

The EIs for UHCs and CO molecules are needed for the evaluation of the overall UCC combustion efficiency. The emissions index for any given molecule is defined by the Society of Automotive Engineers [24] via Equation 2.5. The CAI UHC analyzer behaves essentially as a carbon counter with a defined response factor to carbon molecules which is defined in Appendix A. Therefore, when accounting for the molecular weight of an UHC it is acceptable to use the molecular weight for carbon, 12 atomic mass units.

The combustion efficiency accounts for the tradeoff occurring among UHCs and CO molecules and is defined for propane via Equation 3.6 [24].

$$\eta_b = \left[1 - 4.346\frac{EI_{CO}}{H_C} - \frac{EI_{C_3H_8}}{1000}\right] * 100 \qquad \text{Equation 3.6}$$

Here, H_C is defined as the heat of combustion for propane and is valued at 2200 KJ/mol.

3.6   Uncertainty Analysis

          Measurements associated with this research involve temperature, pressure,

fuel and air mass flow rates as well as the use of general measurements tools such as a

ruler or micrometer. The accuracy of the equipment associated with these measurements

was susceptible to errors within the calibration of the tools themselves. Therefore, an

uncertainty analysis was performed to quantify the accuracy to measured values of the

measurement equipment within the COAL Lab. Figure 3.23 highlights the major

measurement equipment used within the COAL Lab to perform this research. The

published accuracies for each piece of equipment in Figure 3.23 and a baseline set of

experimental results are listed in Table 3.1.
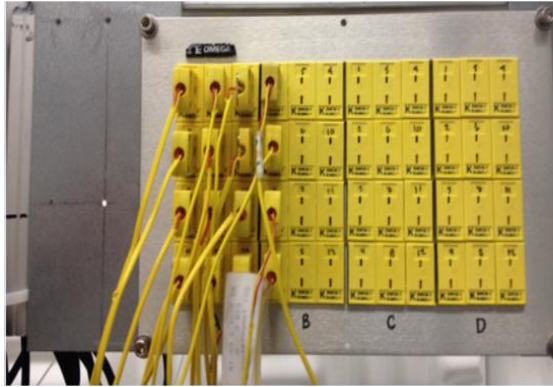
(a)
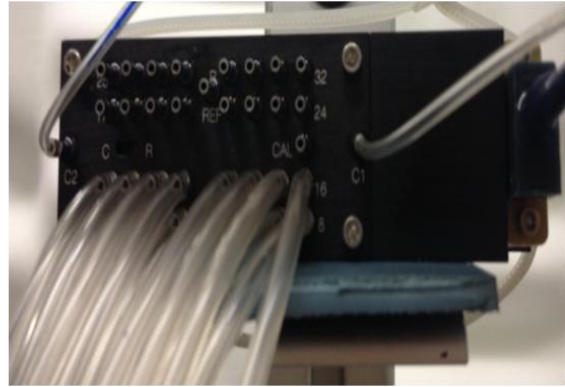
(b)

(c)

(d)

(e)

Figure 3.23. COAL Lab measurement tools: a) K-Type thermocouple pin board, b) DTC
ESP-32HD pressure transducer, c) BIOS Definer 220 fuel flow meter, d) Fox FT2 air
flow meter, and d) Mitutoyo micrometer.

Table 3.1. Published accuracies and experimental results for COAL Lab equipment.

Measurement	Equipment	Experimental Result	Accuracy
Static Pressure	ESP-32HD Transducer	101671 Pa	$\pm 0.03\%$
Total Pressure	ESP-32HD Transducer	101864 Pa	$\pm 0.03\%$
Temperature	K-Type Thermocouple	1048 K	$\pm 2.2\ deg$
Cavity Radius	Micrometer	6.7 cm	$\pm 0.1\ cm$
Fuel Mass Flow Rate	BIOS Definer 220	1.62 kg/min	$\pm 0.25\ \%$
Air Mass Flow Rate	Fox FT2 Flow Meter	90 SLPM	$\pm 1.0\ \%$

From the Constant Odds general form equation [41], shown in Equation 3.7, the uncertainties for cavity Mach number, cavity tangential velocity, cavity g-load, and cavity equivalence ratio were quantified.

$$\delta R = \left\{ \left(\frac{\partial R}{\partial x_1} \delta_{x_1} \right)^2 + \left(\frac{\partial R}{\partial x_2} \delta_{x_2} \right)^2 + \cdots + \left(\frac{\partial R}{\partial x_n} \delta_{x_n} \right)^2 \right\}^{0.5} \qquad \text{Equation 3.7}$$

Here the function/equation is R, x_n is the measured experimental result, and δx_n represents the equipment's measurement accuracy.

The uncertainty of calculated experimental results is shown in Table 3.2. The uncertainty associated with Mach number is orders of magnitude smaller than the uncertanties associated with the other parameters. Because the g-load is dependent upon the square of tangential velocity, the uncertainty associated with g-load grows with error in tangential velocity. Therefore, the largest uncertainty is associated with the g-load.

Table 3.2. Calculated error using Constant Odds general form equation.

Parameter	Measured Value	Uncertainty	Accuracy of Measurement
Inlet Mach Number	0.054	0.006 M	89.9 %
G-Load	1740	414 G	80.8 %
Tangential Velocity	33.8 m/s	3.79 m/s	89.9 %
φ_{cav}	1.65	0.01	99.4 %

Additionally, a repeatability study was performed to check for gross inaccuracies in the data from test date to test date. G-load, Inlet Mach number, and exit Mach number samples were taken on three separate dates for the same reacting flow conditions; core/cavity flow split of 7.92/1.8 kg/min (80/20 core to cavity flow split) and 100 SLPM of fuel. The standard deviation of these parameters across the three dates was 85 g, 0.003, and 0.049 respectively. The unsteadiness of the fluid used to make these measurements is responsible for these deviations. The ambient conditions which change on a daily basis may also have a significant impact on the local operating conditions.

Finally, the calibration curves for each of the three propane MFCs as well as the ESP-32HD pressure transducer can be found in Appendix B. The calibration curves show virtually no significant hysteresis impacts due to loading and unloading. A Root Sum of Squares (RSS) analysis, which combines sources of error at different data points to show the deviation of a given measurement from the expected value was performed with results listed in Table 3.3. Each of the three propane MFCs were calibrated from 0 to 30 L/min and the pressure transducer was evaluated from 0 to 28 kPa.

Table 3.3. RSS analysis results.

Date	Uncertainty
MFC 2	1.62 SLPM
MFC 3	1.42 SLPM
MFC 6	1.78 SLPM
ESP-32HD Pressure Transducer	0.01 (PSID)

3.7   Testing

The main objectives of this research effort including the characterization of

thermal and pressure exit profiles, quantification and evaluation of emissions

performance, and quantification and evaluation of overall system pressure losses and

Rayleigh loss were accomplished following the implementation of the equipment

modifications discussed above. This section outlines the UCC configurations, equipment

set-ups, and test matrices used to accomplish each research objective.   These tests will

outline the new experiments performed with the AFIT UCC.

3.7.1   Thermal and Pressure Exit Profiles

This experiment provided the foundation for future research in shaping and

molding thermal and pressure profiles to optimal levels. The primary objective of this

experiment was to characterize the heat release and pressure distributions at set locations

across the exit span from ID to OD. The secondary experimental objective was to study

those parameters that most strongly influence the shape and magnitude of the thermal and

pressure profiles. These parameters include the cavity g-load, the cavity equivalence

ratio, the mass flow split, and total bulk air mass flow. Each test associated with this

experiment was accomplished using the 0.45 cm hole combustion ring as well as the

LLCB designed by Wilson [5]. The combustion ring was oriented to provide CW

swirling flow relative to a downstream flow perspective. The UCC was operated with

injection ring fuel baffles which were not utilized in the results provided by Wilson [5].

In terms of testing for the characterization of thermal exit profiles, the test matrix

shown in Table 3.4 was constructed to verify the results of LeBay [15] in showing the

sensitivity of the temperature profile to changes in mass flow ratio more so than cavity

equivalence ratio and g-loading. Four distinct flow splits were evaluated: 60/40, 70/30,

75/25, and 80/20. The bulk air masses at each flow split were maintained so as to keep

the level of heat release purely a function of the cavity equivalence ratios. The cavity

equivalence ratios were selected based off the UCC's stability map discussed in Section

4.1 and the UCC's ability maintain a steady level of performance for the given

atmospheric conditions. The circumferential height variation instrumentation scheme

shown in Figure 3.15b was used to collect the resulting profiles.

Table 3.4. Thermal exit profile test matrix.

Core Mass Flow Rate kg/min	Cavity Mass Flow Rate kg/min	Bulk Air Mass Flow Rate kg/min	Core /Cavity Flow Split %/%	Fuel Mass Flow Rate SLPM	Cavity φ
3.40	2.16	5.40	60/40	120	1.65
3.40	2.16	5.40	60/40	114	1.57
3.40	2.16	5.40	60/40	105	1.45
3.40	2.16	5.40	60/40	100	1.38
3.40	2.16	5.40	60/40	90	1.24
3.40	2.16	5.40	60/40	75	1.03
3.40	2.16	5.40	60/40	63	0.87
4.54	1.93	6.47	70/30	36	0.56
4.54	1.93	6.47	70/30	45	0.69
4.54	1.93	6.47	70/30	54	0.83
4.54	1.93	6.47	70/30	63	0.97
4.54	1.93	6.47	70/30	75	1.16
4.54	1.93	6.47	70/30	90	1.39
4.54	1.93	6.47	70/30	100	1.55
4.86	1.62	6.48	75/25	54	0.99
4.86	1.62	6.48	75/25	63	1.16
4.86	1.62	6.48	75/25	75	1.38
4.86	1.62	6.48	75/25	90	1.65
4.86	1.62	6.48	75/25	100	1.84
4.86	1.62	6.48	75/25	115	2.11
4.86	1.62	6.48	75/25	130	2.39
4.86	1.62	6.48	75/25	145	2.66
4.86	1.62	6.48	75/25	156	2.88
7.92	1.80	9.72	80/20	54	0.89
7.92	1.80	9.72	80/20	63	1.04
7.92	1.80	9.72	80/20	75	1.24
7.92	1.80	9.72	80/20	90	1.49

Pressure exit profiles were also collected using the same UCC equipment configuration as the thermal exit profiles. The influencing parameter of interest was mainly the mass flow split as Barringer [32, 33] shed light on the fact that exit plane pressure profiles are heavily influenced by the momentum of entrained air flows. These entrained air flows exist in the form of film cooling air in a combustor liner or the entrainment of cavity flow into core flow within a UCC. Therefore, the test matrix in Table 3.5 was built to highlight changes to the pressure profile with changes in mass flow split. Specifically, the amount of core flow is increased noticeably between each flow split so as to highlight the profile's sensitivity to core flow momentum.

Table 3.5. Pressure exit profile test matrix.

Core Mass Flow Rate kg/min	Cavity Mass Flow Rate kg/min	Bulk Air Mass Flow Rate kg/min	Core /Cavity Flow Split %/%	Fuel Mass Flow Rate SLPM	Cavity φ
3.40	2.16	5.40	60/40	120	1.65
3.40	2.16	5.40	60/40	114	1.57
3.40	2.16	5.40	60/40	105	1.45
3.40	2.16	5.40	60/40	100	1.38
3.40	2.16	5.40	60/40	90	1.24
3.40	2.16	5.40	60/40	75	1.03
3.40	2.16	5.40	60/40	63	0.87
3.96	1.62	5.58	70/30	54	0.99
3.96	1.62	5.58	70/30	63	1.16
3.96	1.62	5.58	70/30	75	1.38
3.96	1.62	5.58	70/30	90	1.65
3.96	1.62	5.58	70/30	100	1.84
3.96	1.62	5.58	70/30	105	1.93
5.04	1.62	6.66	75/25	54	0.99
5.04	1.62	6.66	75/25	63	1.16
5.04	1.62	6.66	75/25	75	1.38
5.04	1.62	6.66	75/25	90	1.65
7.92	1.80	9.72	80/20	54	0.89
7.92	1.80	9.72	80/20	63	1.04
7.92	1.80	9.72	80/20	75	1.24
7.92	1.80	9.72	80/20	90	1.48
7.92	1.80	9.72	80/20	100	1.65
7.92	1.80	9.72	80/20	105	1.74

3.7.2 Emissions Analysis

The primary objective of the emissions experiments was to characterize emissions across the exit span from ID to OD at set locations across the exit span. The secondary objective was to understand the parameter(s) that best promoted good combustion efficiency.   The CAI machine was configured to collect UHC, CO_2, CO, and O_2 specimens. The single channel probe, mounted on a horizontal traverse spanned the 2.54 cm exit span at 5 mm increments making a total of 6 collection points across the entire exit span from ID to OD using the experimental set-up shown in Figure 3.22. The experiment was performed using the 0.45 cm hole combustion ring, providing CW cavity swirl, in combination with the LLCB. Again, the UCC was operated with injection ring fuel baffles which were not utilized previously. Table 3.6 outlines the test conditions used to identify those parameters most influential to combustion efficiency. The matrix

maintains the same flow split at the same bulk air mass flow rate, different flow splits at the same cavity equivalence ratio, and different flow splits at the same bulk air mass flow rate. Conducting the analysis in this fashion shows combustion efficiency sensitivities to either the cavity bulk air mass flow, the cavity g-loading, or the mass flow split.

Table 3.6. Emissions analysis test matrix.

Core Mass Flow Rate kg/min	Cavity Mass Flow Rate kg/min	Bulk Air Mass Flow Rate kg/min	Core /Cavity Flow Split %/%	Fuel Mass Flow Rate SLPM	Cavity φ
6.12	1.62	7.74	70/30	90	1.65
6.12	1.62	7.74	70/30	105	1.93
6.12	1.62	7.74	70/30	114	2.09
6.12	1.62	7.74	70/30	120	2.21
4.68	1.98	6.66	70/30	90	1.35
3.96	1.62	5.58	70/30	54	0.99
3.96	1.62	5.58	70/30	63	1.16
3.96	1.62	5.58	70/30	75	1.38
3.96	1.62	5.58	70/30	90	1.65
3.96	1.62	5.58	70/30	100	1.84
3.96	1.62	5.58	70/30	105	1.93
6.48	2.16	8.64	75/25	90	1.24
5.04	1.62	6.66	75/25	54	0.99
5.04	1.62	6.66	75/25	63	1.16
5.04	1.62	6.66	75/25	75	1.38
5.04	1.62	6.66	75/25	90	1.65
3.24	1.08	4.32	75/25	60	1.65
7.92	1.80	9.72	80/20	54	0.89
7.92	1.80	9.72	80/20	63	1.04
7.92	1.80	9.72	80/20	75	1.24
7.92	1.80	9.72	80/20	90	1.48
7.92	1.80	9.72	80/20	100	1.65
7.92	1.80	9.72	80/20	105	1.74
6.12	1.62	7.74	80/20	100	1.84
5.40	1.26	6.66	80/20	63	1.49

These tests were conducted using a combination of the circumferential height varying thermocouple set-up, circumferential height varying pitot probe set-up, and single channel emissions probe. This set-up, shown in Figure 3.24, allowed for the comparison of thermal, pressure and emissions profiles at the same test conditions.

94
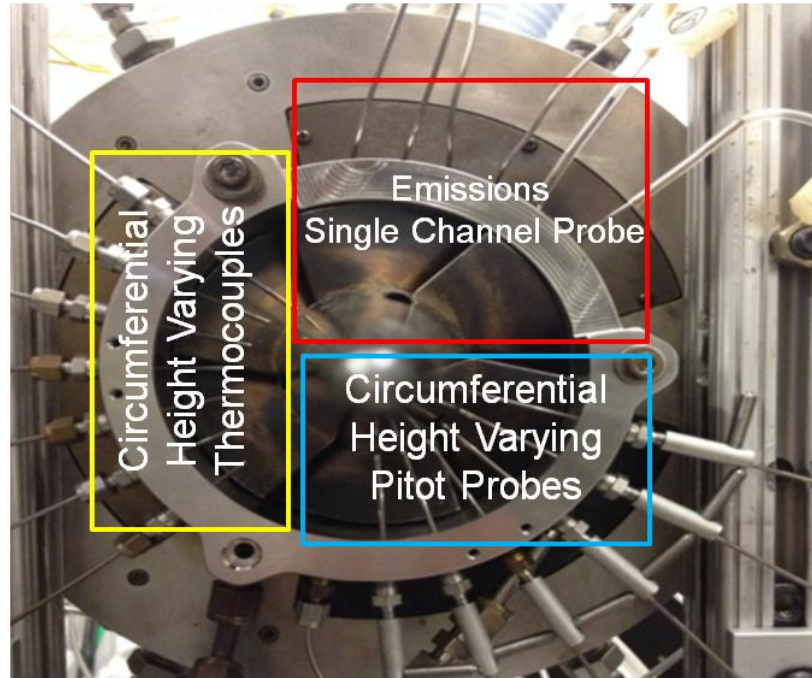
Figure 3.24. Emissions, thermal profile, and pressure profile set-up.

3.7.3 Pressure Loss and Rayleigh Loss Analysis

Pressure loss experiments were performed with a primary objective of

characterizing the UCC system pressure losses from inlet to exit. The main component to

component pressure drops of interest are inlet to exit, air plenum to UCC cavity, and

UCC cavity to exit. This characterization will help identify where the pressure drops

exist throughout the UCC to drive the flow from inlet to exit. As a secondary objective,

it was sought to embellish upon the work performed by Wilson [5] to achieve more

realistic Rayleigh pressure loss numbers resulting from higher inlet and exit Mach

numbers. The addition of a third propane MFC (as discussed in Section 3.3.1) allowed

for higher cavity equivalence ratios at lower core to cavity flow splits (i.e. 70/30) to be

investigated. Again, all experiments associated with this research objective were

conducted using the 0.45 cm hole combustion ring, providing CW cavity swirl, with both

LLCB and fuel baffles installed. The test matrix in Table 3.7 boasts an array of mass flow

splits at various bulk air masses and cavity equivalence ratios. UCC system pressure

losses will be shown as a function of mass flow split and various bulk air masses. The

difference in reacting and non-reacting flows was required to quantify the pressure loss

between aerodynamic flows and Rayleigh flows.

Table 3.7. System and Rayleigh pressure loss test matrix.

Core Mass Flow Rate kg/min	Cavity Mass Flow Rate kg/min	Bulk Air Mass Flow Rate kg/min	Core /Cavity Flow Split %/%	Reacting/Non-Reacting	Fuel Mass Flow Rate SLPM	Cavity φ
4.68	1.98	6.66	70/30	Non-Reacting	-	-
4.68	1.98	6.66	70/30	Reacting	90	1.35
3.96	1.62	5.58	70/30	Non-Reacting	-	-
3.96	1.62	5.58	70/30	Reacting	54	0.99
3.96	1.62	5.58	70/30	Reacting	63	1.16
3.96	1.62	5.58	70/30	Reacting	75	1.38
3.96	1.62	5.58	70/30	Reacting	90	1.65
3.96	1.62	5.58	70/30	Reacting	100	1.84
3.96	1.62	5.58	70/30	Reacting	105	1.93
5.04	1.62	6.66	75/25	Non-Reacting	-	-
5.04	1.62	6.66	75/25	Reacting	54	0.99
5.04	1.62	6.66	75/25	Reacting	63	1.16
5.04	1.62	6.66	75/25	Reacting	75	1.38
5.04	1.62	6.66	75/25	Reacting	90	1.65
7.92	1.80	9.72	80/20	Non-Reacting	-	-
7.92	1.80	9.72	80/20	Reacting	54	0.89
7.92	1.80	9.72	80/20	Reacting	63	1.04
7.92	1.80	9.72	80/20	Reacting	75	1.24
7.92	1.80	9.72	80/20	Reacting	90	1.48
7.92	1.80	9.72	80/20	Reacting	100	1.65
7.92	1.80	9.72	80/20	Reacting	105	1.74
5.40	1.26	6.66	80/20	Non-Reacting	-	-
5.40	1.26	6.66	80/20	Reacting	63	1.49

IV. Analysis and Results

Three primary objectives encompass the goals of this research effort: the key parameters that influence the thermal and pressure exit profiles, the quantification of UCC system pressure losses as well as Rayleigh pressure loss, and the characterization of emissions species at the exit plane. The secondary objective is to study the impacts on UCC operation with respect to changes in the cavity equivalence ratio, total combustor air mass, and the core/cavity mass flow ratio. The results for each objective will be outlined sequentially in this chapter beginning with the characterization of the combustor's exit profile. These profiles shed light upon the subsequent emissions analysis and drive the analysis for understanding the overall system losses associated with the AFIT UCC. The baseline operating conditions for the combustor are outlined with a stability map describing the relationship between the cavity equivalence ratio and the cavity g-load. This fundamental relationship outlines the key factors which are responsible for the manipulation of the exit conditions, the combustor's emissions characteristics and the overall system losses.

4.1.   UCC Operating Baseline

The AFIT UCC range of operability is defined by characterizing the UCC cavity equivalence ratio as a function of the cavity g-load. Figure 4.1 exhibits the stability mapping of the UCC. The stability map shows the cavity equivalence ratio as a function of the cavity g-loading. The map is formed by first establishing a desired flow split condition and then setting a fuel flow rate which adjusts the cavity stoichiometry to a desired equivalence ratio. Reducing the fuel flow rate at each flow split condition until

97

blowout occurs explains how the map in Figure 4.1 was generated. The stability of each

set point was judged via visual and audio inspection. Stable points operated with steady

exit plane luminescence and a distinct, constant pitch. Decreasing stability points were

indicated by a fainter luminescence at the exit plane and periodic disruptions in operating

pitch. Blowout occurred when the UCC could no longer sustain operation. Overall the

UCC operated at a stable condition for flows splits ranging from 85/15 to 70/30 at cavity

equivalence ratios from 0.56 to 2.86 and cavity g-loads from 0 to approximately 3900.

The green data points outline the UCC's overall stability performance staying consistent

with results of Zelina [3] and Wilson [5], decreasing cavity equivalence ratios

(decreasing fuel flows) correspond to higher cavity g-loads. The lower decreasing

stability (yellow) and blowout (red) conditions trend lines indicate the cavity lean limits

of stability for the AFIT UCC while the upper stability lines indicate the cavity rich limits

of stability.
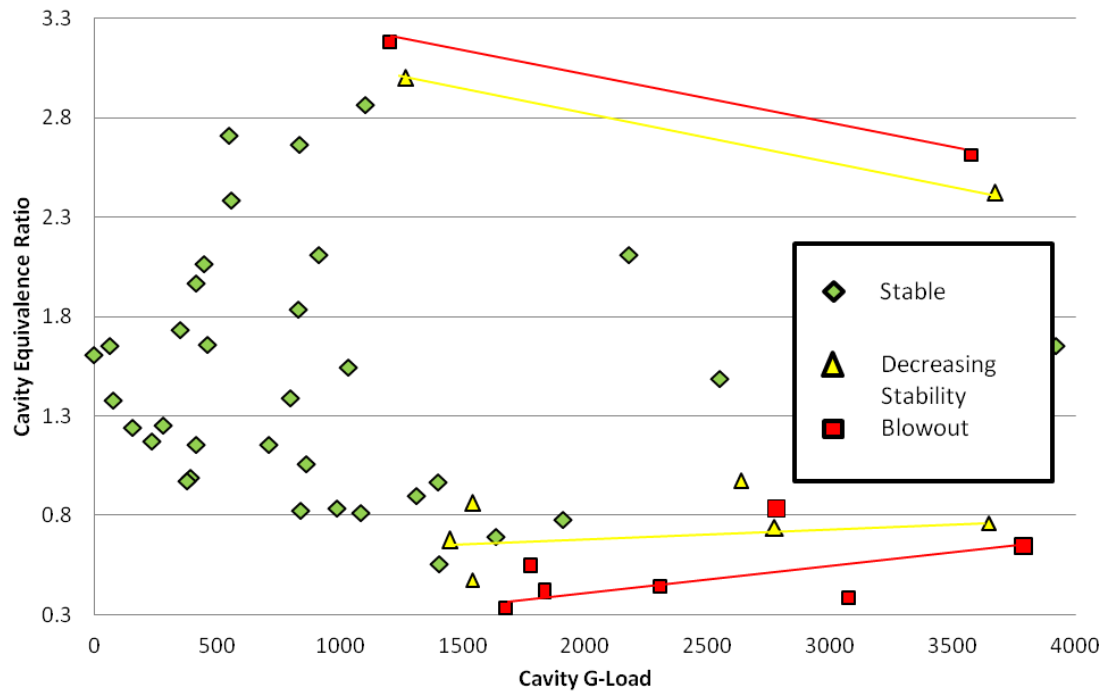
Figure 4.1. AFIT UCC stability map.

4.2   Identification and Characterization of Exit Profiles

The shape and magnitude of the UCC thermal and pressure exit profiles is important to quantify since the goal for the UCC is to generate similar boundary conditions to the turbine stage of an axial engine. Ideally, the turbine should not be able to distinguish between flows exerted from a UCC versus a traditional axial length combustor. The overall implementation goal of a UCC into a traditional axial engine would be to make the transition between combustor types without any loss in turbine output performance. Understanding the key parameters that influence the profiles shape is vital to mold these exit thermal and pressure profiles properly.

4.2.1   UCC Thermal Exit Profiles

Exit thermal profiles are desired to stay consistent with those described by Samuelson [31] and Barringer [30] with an OD skew to maximize turbine power extraction from the flow and increase the survivability of critical turbomachinery components. This study documents the exit temperature profiles of the AFIT UCC over a range of cavity flow splits with the same overall total mass flow. All tests were conducted using the same UCC configuration to include the LLCB, 0.45cm diameter hole air injection ring, and clockwise swirl direction. Both the UCC core flow and cavity flows were independently controlled to obtain four Core/Cavity percentage air flow splits at 60/40, 70/30, 75/25, and 80/20.   The UCC cavity was fueled with gaseous propane (C_3H_8) with flow rates that varied from 0.06 to 0.29 kg/min. This generated cavity equivalence ratios which ranged from 0.56 to 2.86 resulting in overall equivalence ratios of 0.16 to 0.71 at g-loads ranging from 0g to 2060g.

Measurements for the characterization of the thermal exit conditions were taken with the circumferential height varying probes (yellow box in Figure 3.15b) for the 60/40, 70/30, 75/25 and 80/20 core to cavity flow splits at an average inlet temperature of 291K and in accordance with test matrix in Table 3.4. At each flow split, as the fuel (and thus the equivalence ratio) was increased in the cavity, higher temperatures were recorded at the exit plane consistent with the higher heat release for the additional fuel. Figure 4.2 shows that the temperature profile was consistently skewed toward the OD. For a given flow split, this trend was maintained over the range of cavity equivalence ratios from lean UCC cavities to rich cavities. Although these profiles are OD skewed, their shape is not entirely consistent with those presented by Barringer [30]. Therefore,

there exist some modifications to key operating parameters that will shape these profiles differently.

(a)   (b)

(c)   (d)
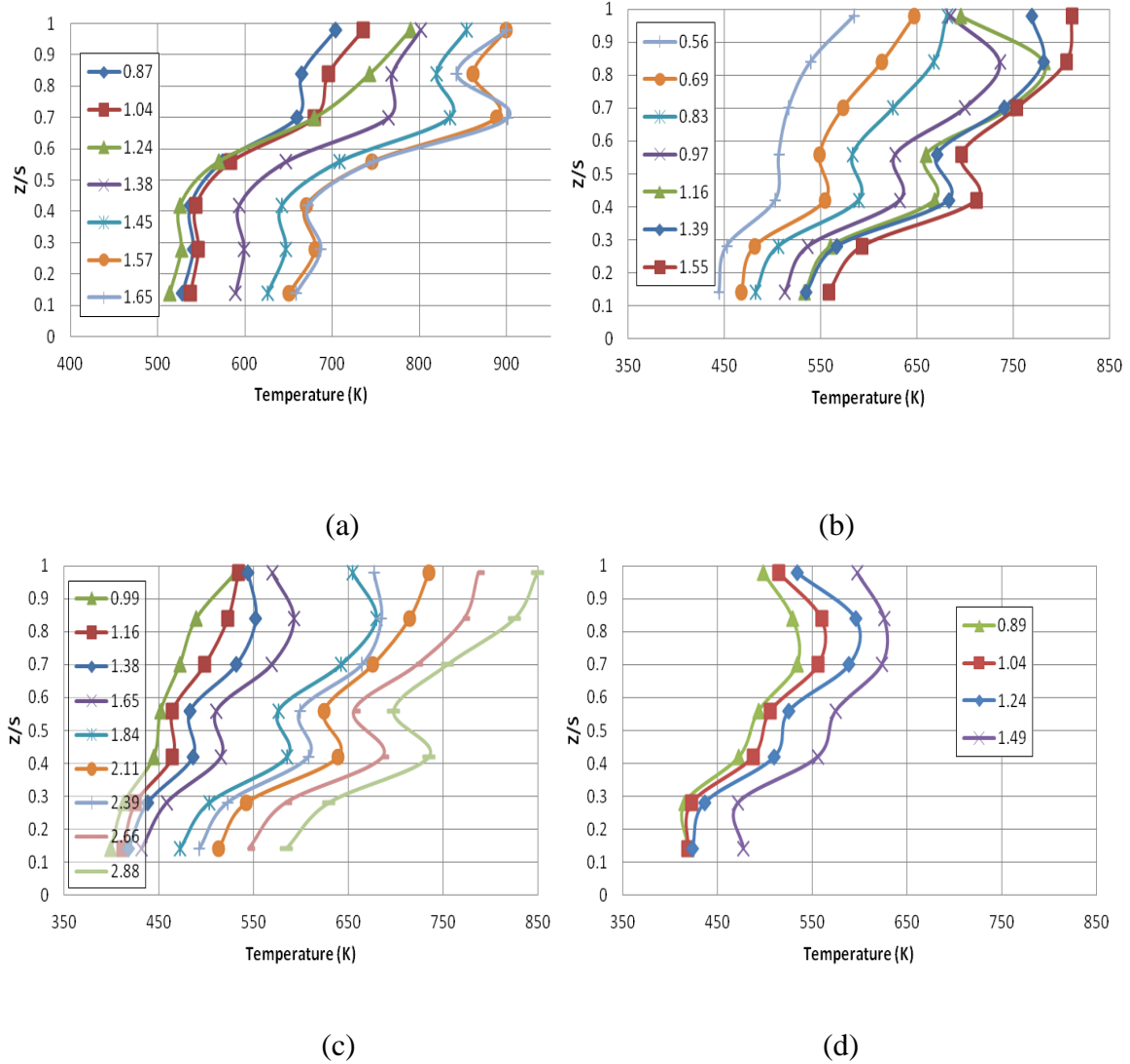
Figure 4.2. Temperature profiles for circumferential varying probes with a) 60/40 b) 70/30 c) 75/25 and d) 80/20 flow splits.

To further understand the temperature profiles' sensitivity to equivalence ratio, the data was re-plotted in terms of the pattern (Equation 2.9) and profile (Equation 2.10) factors. Shown in Figure 4.3 for the 75/25 and 80/20 flow splits, as equivalence ratio

increases, the factors remain nearly identical. Hence, in the case of the pattern factor, the maximum temperature deviates from the temperature rise across the UCC equally for all changes in cavity equivalence ratio. Similarly, the average exit temperature deviates equally from the temperature rise across the UCC for the profile factor. This confirms the results from LeBay et al. [15] that the cavity equivalence ratio does not impact the exit temperature profile but merely affects magnitude of the heat release and thus the overall temperature level.
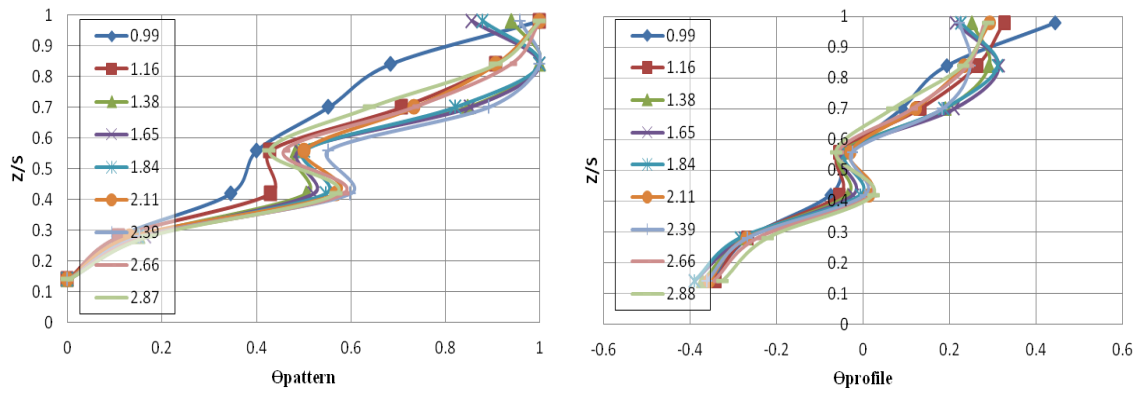
(a)
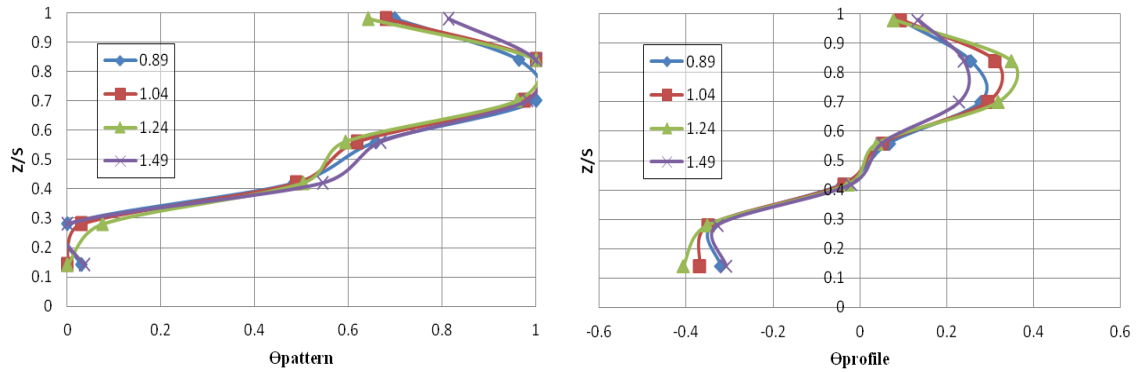
(b)

Figure 4.3. Pattern and Profile factors for a) the 75/25 and b) 80/20 flow splits.

This insensitivity to increased levels of fuel flow indicates that the UCC exit temperature profile is largely independent of the cavity equivalence ratio. However, Figure 4.4 depicts the pattern and profile factors are sensitive to the flow split. Cavity equivalence ratios between 1.38-1.55 are shown for each of the four flow splits. This variability suggests that the temperature profile is more sensitive to the mass flow split. This finding is consistent with that of LeBay [15] where increases in the mass flux ratio between the core and cavity flow correlated to increased flame injection angles out of the UCC cavity. Hence, changes in flow split dictate the degree to which hot gas products exit the UCC cavity.

(a)   (b)
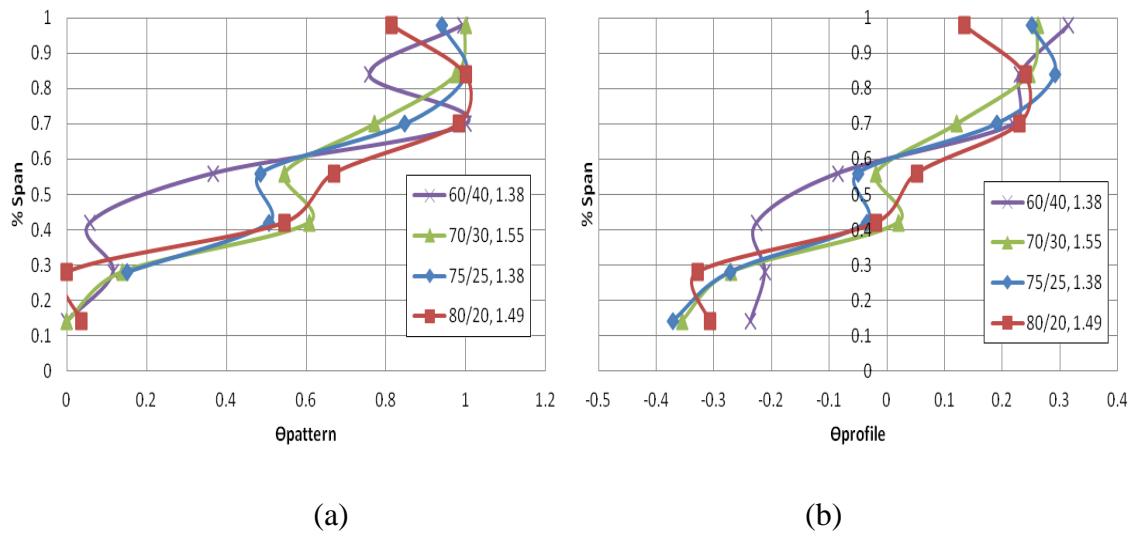
Figure 4.4. a) Pattern and b) profile factors for 60/40, 70/30, 75/25, and 80/20 flow splits for equivalence ratios of 1.38-1.55.

To further highlight the difference of heat release amongst the four flow splits, temperatures were measured at midspan (Figure 3.15b red box). Here the average temperature was significantly reduced at the same cavity equivalence ratio as the flow split was changed. As the cavity air decreased, the temperature in the cavity also

decreased as expected based on flame temperature as a function of cavity equivalence ratio and also shown by Parks [17]. Parks [17] used Chemkin [42] to study the effect on flow split for a similar UCC configuration. Table 4.1 reveals that as the cavity equivalence ratio increases past one, the temperature in the cavity drops. For very fuel rich cavities ($\varphi > 2.0$), there is not enough air for combustion to continue once flow from the UCC cavity is entrained into the on-coming core flow. Therefore, temperatures remain close to that of the core flow. For lesser equivalence ratios, ($\varphi = 1.0 \ to \ 1.75$) reactions continue to occur after mixing with the core flow and there exists a temperature rise through the remainder of the UCC center body vane passages and past the exit plane. However, when the core flow dominates the flow split (83.4% case) reactions are quenched immediately upon introduction to the core flow and minimal temperature rise is experienced throughout the remainder of the UCC.

Table 4.1. Reacting flow temperature rise through UCC vane passages [Data from 17].

Mass Flow Cavity Split (%)	Cavity φ	Cavity Temp (K)	Cavity Exit Temp (K)	Vane Exit Temp (K)
16.7	2.5	700	700	700
18.8	2.21	750	750	750
19.8	2.1	1100	1250	1300
20.8	2.0	1250	1300	1325
23.8	1.75	1250	1300	1325
33.3	1.25	1375	1400	1450
41.7	1.0	1425	1400	1450
83.4	0.5	1490	1500	1500

Figure 4.5a highlights this phenomenon for the current results. As the core flow split increases, the overall heat release is decreased as the heat is quenched by the larger more dominant core flow. For cavity equivalence ratios greater than one, the average exit midspan temperature begins to rise up until the point where the cavity becomes too rich ($\varphi > 2$) as seen in the 75/25 flow split condition. Figure 4.5b indicates the same trend in terms of the overall UCC equivalence ratio. Furthermore, the 60/40 flow split resulted in

104

significantly higher exit temperatures for the same amount of fuel. Therefore, it is

apparent that there was a preferential distribution of the flow between cavity and core.

(a)   (b)
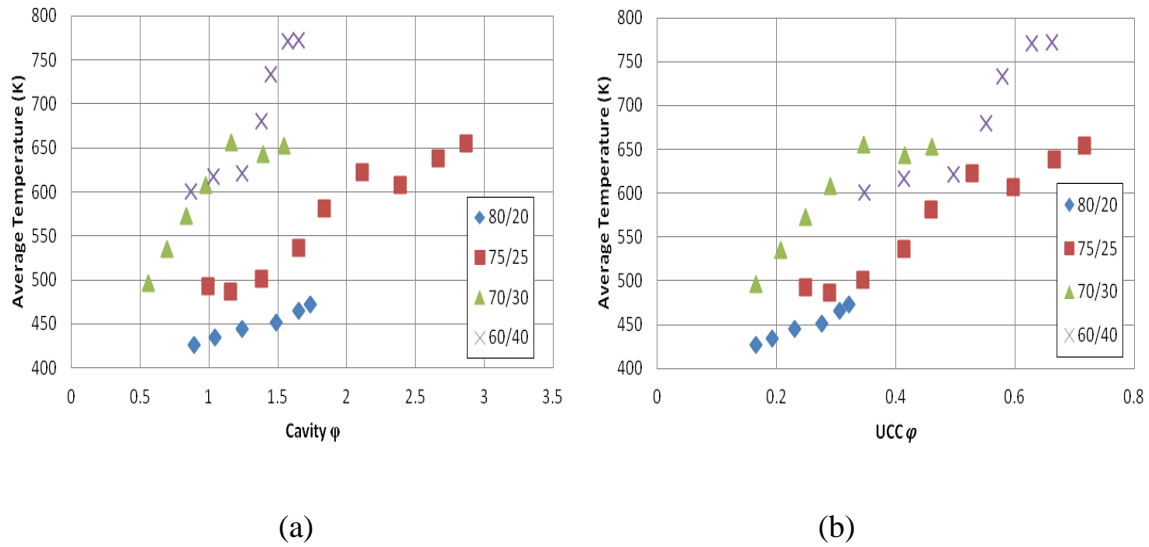
Figure 4.5. Radial midspan average of temperature at UCC exit as function of a) Cavity
equivalence ratio and b) the overall UCC equivalence ratio.

Comparing the heat release at a common 70/30 mass flow split, for different

amounts of total bulk air, as shown in Figure 4.6, one can see the 6.66 kg/min bulk air

mass relates to the largest total heat release. Note that more rich equivalence ratios could

not be achieved at the 6.66 kg/min condition because of operational issues and not

stability issues.   Moving from left to right, rich cavity blow out occurs at relatively high

cavity equivalence ratios for the 5.58 and 7.74 kg/min bulk air masses. However, this

rich blowout does not correlate to a large heat release. This suggests the 6.66 kg/min air

mass induces a better combustion process. Moving right to left, the 5.58 and 7.74 kg/min

bulk air masses do not support lean burning as well as the 6.66 kg/min air mass again

suggesting a more robust combustion process at this total air mass. All in all, a larger

total air mass supports larger cavity equivalence ratios however, this benefit is not

realized at the exit plane as the heat is quenched out by the larger air mass.
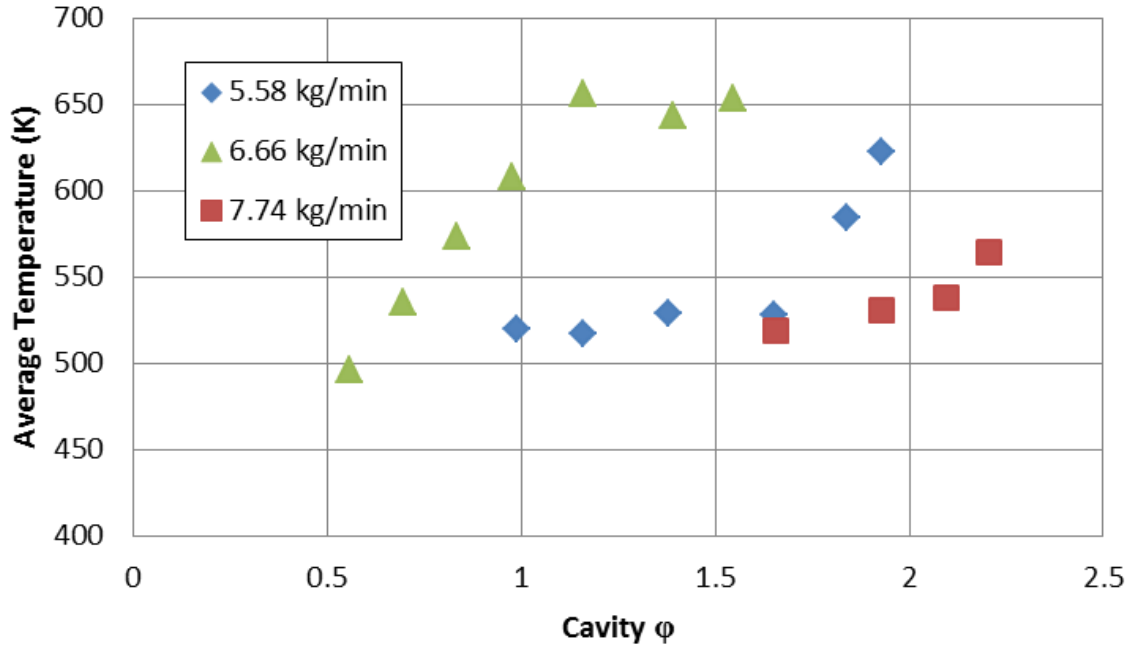
Figure 4.6. Heat release among different total air masses at 70/30 mass flow split.

The variations in profile shape are largely a function of the core and cavity flow

conditions. However, the pitch wise location of the exit thermocouples was affected by

the presence of the vane wake. For the circumferential height variation configuration

(Figure 3.15b yellow box) the thermocouple at 40% was impacted by the wake emanating

from the vane as indicated in Figure 4.7. By investigating the profile across the

circumferential pitch with seven additional temperatures at the same height (Figure 3.15b

red box) and then moving together in the radial direction, the impact of the vane exit

wake was reduced. Radial height variations were made in 0.32 cm increments from ID to

OD starting at 0.32 cm from the OD to 2.24 cm from the OD. Figure 4.7 captures the

difference in the data collection schemes for the two configurations at the same 70/30

flow split with cavity equivalence ratio of 0.97. The seven probes were averaged

circumferentially generating the radial variation curve (blue) which removed the impact

of the wake on the exit profile as compared to the circumferential height variation

configuration (red). The emissions analysis conducted in Section 4.4 will offer a better

understanding of these results by showing where the combustion process is occurring

across the exit span.
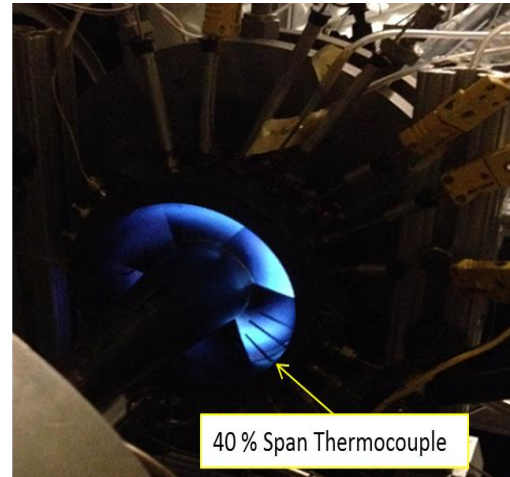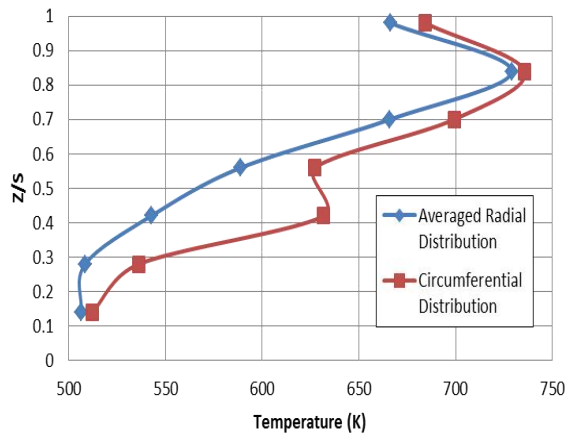
(a)   (b)

Figure 4.7. a) Average radial variation versus circumferential variation and b) UCC exit
plane flame location.

Comparing temperature profiles taken at the same test condition with temperature

probes at different circumferential locations about the exit plane as seen in Figure 4.8, the

profile shapes maintain their OD skew yet differ in magnitude. Figure 4.9a shows the

differences in the profiles. The total UCC inlet temperatures were 293K and 295K for

9 Nov 2013 and 1 Feb 2014 respectively. The 9 Nov 2013 profile maintains a

discontinuity at the 40% span mark due to the thermocouple lying directly behind the

vane exit. This discontinuity is shifted in the 1 Feb 2014 profile given the different

circumferential orientation between the two dates. Looking at the resulting pattern factors, the profile shape remains similar between the two dates as shown in Figure 4.9b. This speaks to the repeatability of the results at the same mass flow split condition on different dates. The slope of the pattern factor profiles is similar and subtle differences can be attributed to the differences in thermal profile magnitudes.

(a)   (b)
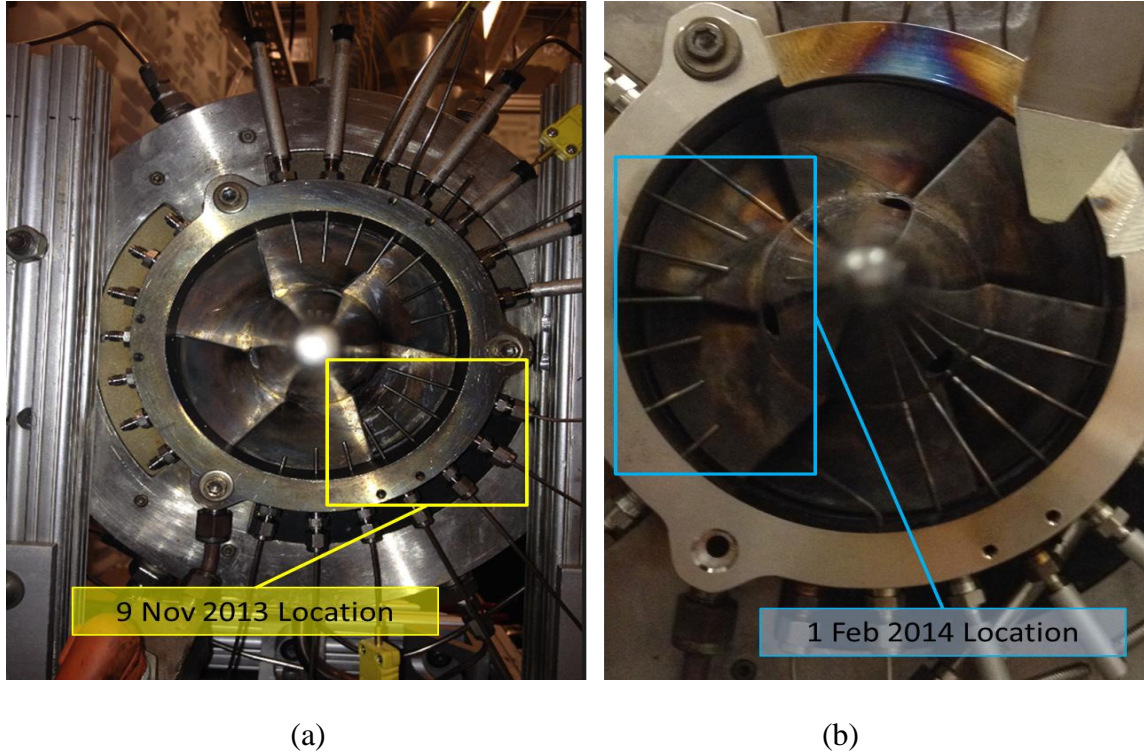
Figure 4.8. Circumferential height varying thermocouple locations on a) 9 Nov 2013 and b) 1 Feb 2014.

(a)   (b)
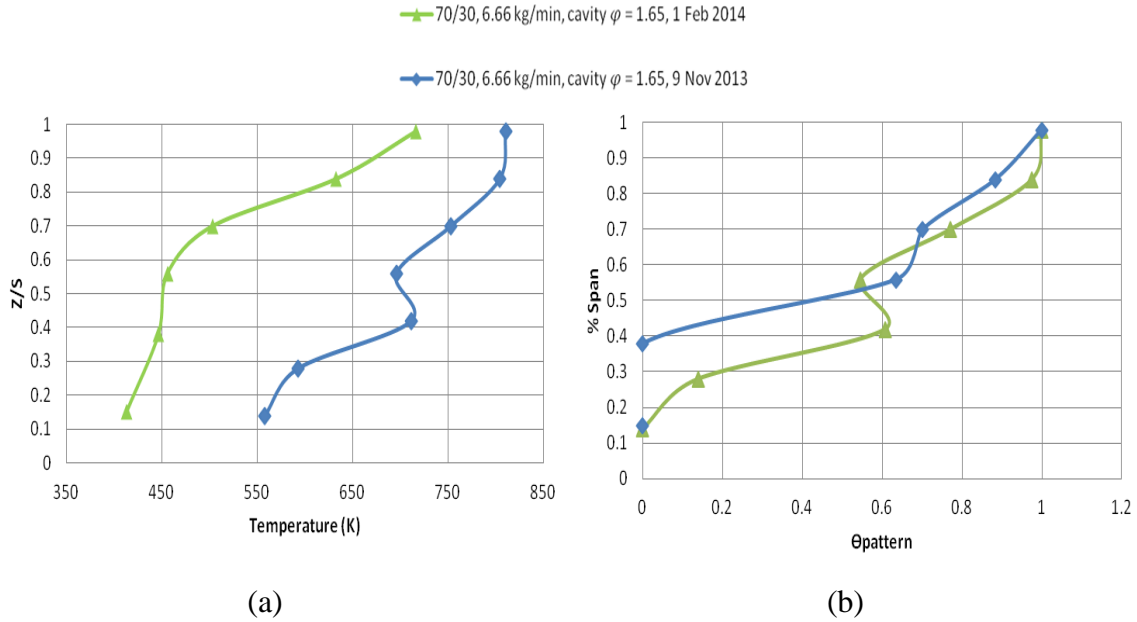
Figure 4.9. a) Thermal profiles from 1 Feb 2014 and 9 Nov 2013 and b) resulting pattern factors.

4.2.2   UCC Pressure Exit Profiles

Understanding of the exit profile shape sheds light onto where the most power extraction will occur by the turbine across the span. Barringer [32, 33] highlights that skews in the pressure profile indicate regions of faster moving flow due differences in the flow momentum. Controlling where these high momentum skews occur will help to maximize the turbine power extraction from the oncoming flow.

Measurements for the characterization of the pressure exit conditions were taken with circumferential height varying probes (Figure 3.16) which utilized the high strength hypodermic tubing with an EDM hole in accordance with the test matrix in Table 3.5. The four core/cavity flow splits evaluated were 60/40, 70/30, 75/25 and 80/20 at an atmospheric pressure of 100.98 kPa and exit plane static pressures of 102.92 kPa, 103.06 kPa, and 102.57 kPa respectively. At each flow split, as the fuel (and thus the

109

equivalence ratio) was increased in the cavity, pressure profiles remained constant

through a variety of cavity equivalence ratios. Figure 4.10 shows that the pressure profile

was consistently skewed toward the OD as was observed with the thermal profiles. For a

given flow split, this trend was maintained over the range of cavity equivalence ratios

from lean UCC cavities to rich cavities. For the 70/30 and 75/25 flow split conditions, a

drop in total pressure is experienced at the 60% span followed by an increase toward the

OD. For the 60/40 and 80/20 flow split conditions, only a significant increase in total

pressure is experienced starting at the 60% span moving toward the OD.
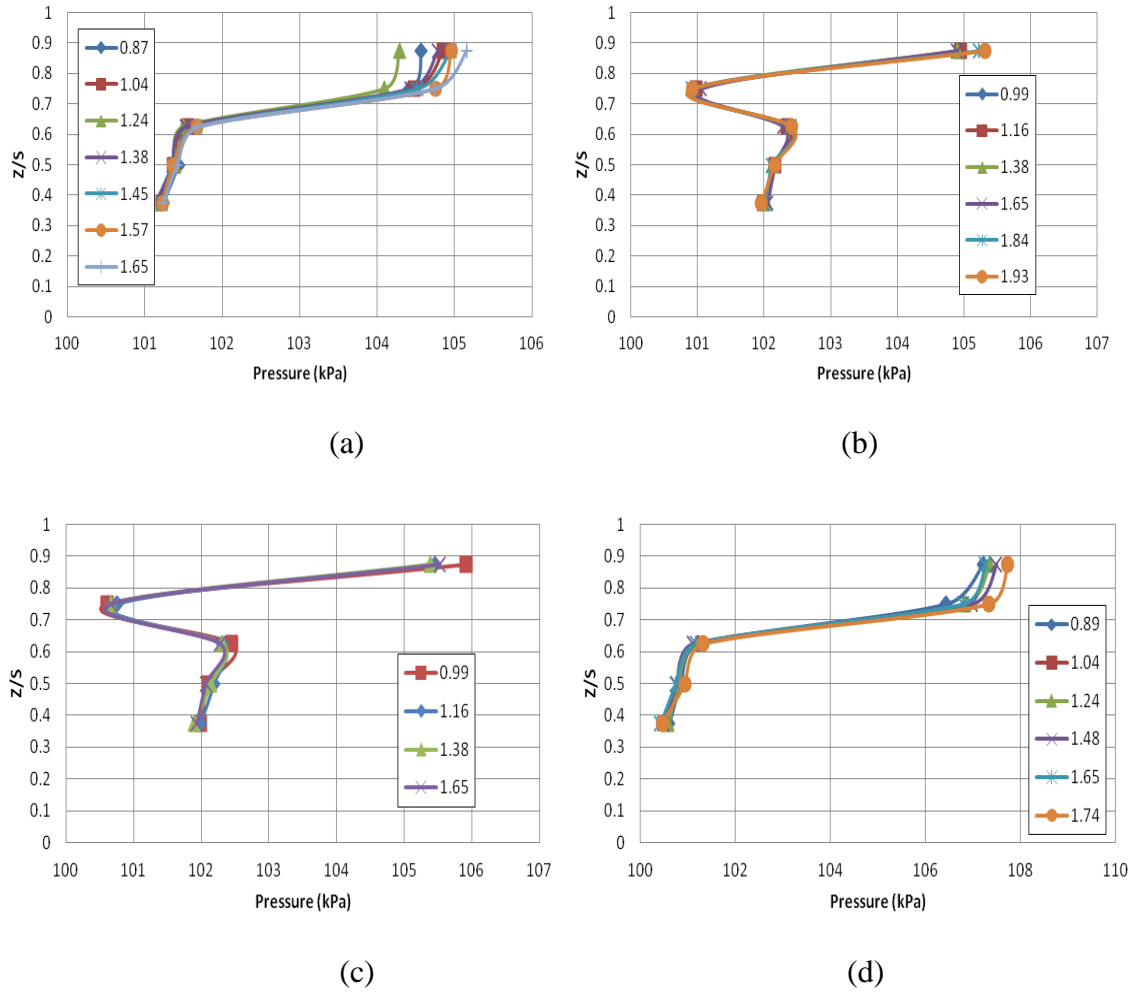
Figure 4.10. Pressure profiles for circumferential varying probes with a) 60/40 b) 70/30 c) 75/25 and d) 80/20 flow splits.

The OD skew associated with profiles in Figure 4.10 is best described by relating the entrainment of hot cavity flow into the relatively cooler core flow to the entrainment of wall film cooling into core combustor flow as would be seen within a traditional axial combustor. Barringer [32, 33] showed similar looking profiles and linked the larger momentum of the cooling flow to skew within the measured profiles. Specific to the UCC, the relatively larger momentum of the cavity flow carries through to the exit plane of the combustor. The centerbody vane passages do not mix the two colliding flow paths

111

from the core and cavity effectively. More effective mixing of the entrained air from the cavity would result in profiles with less severe profile gradients resulting in a more uniform pressure distribution across the exit span.

As with the thermal profiles, sensitivities to changes in the cavity equivalence ratio are best seen through the use of non-dimensional pattern and profile factors for pressure where pressure replaces temperature in Equations 2.9 and 2.10. Figure 4.11 shows the pattern and profile factors for the 75/25 and 80/20 flow split conditions where increases in the cavity equivalence ratio resulted in nearly identical profiles. This indicates that both the maximum and average pressures are deviating the same with respect to the pressure drop across the combustor regardless of the cavity equivalence ratio.
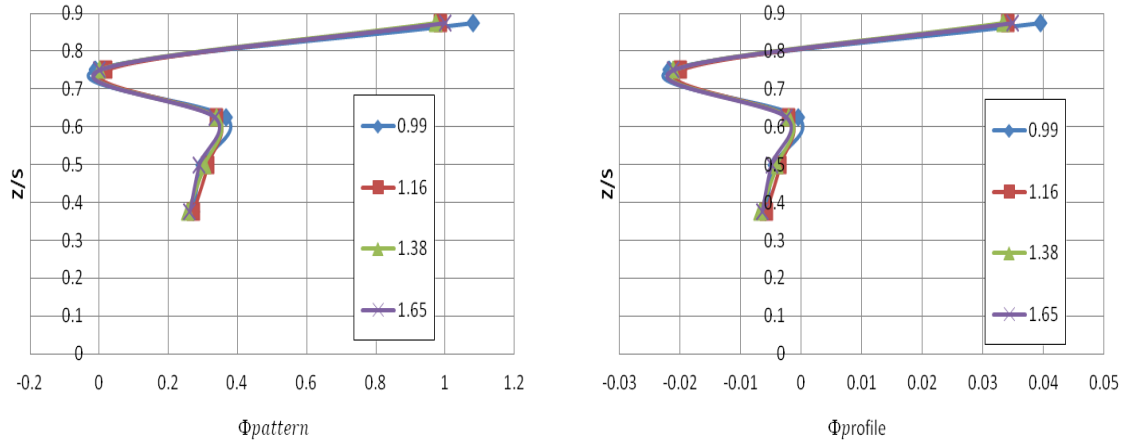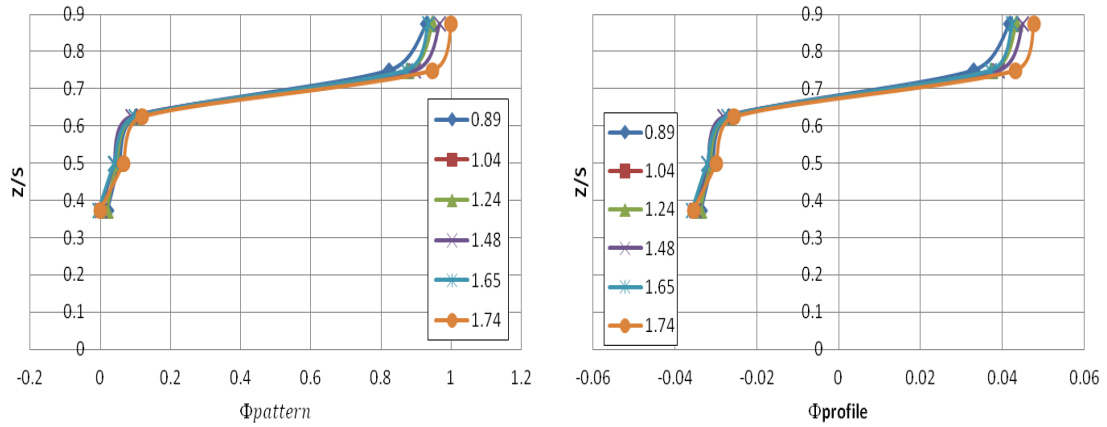
Figure 4.11. Pattern and profile factors for a) the 75/25 and b) 80/20 flow splits.

This insensitivity to increased levels of fuel flow indicates that the UCC exit pressure profile is largely independent of the cavity equivalence ratio. However, Figure 4.12 depicts that the non-dimensional pattern and profile factors for pressure are sensitive to the flow split. The degree of variability across the four flow splits for one cavity equivalence ratio suggests that the pressure profile is more sensitive to the mass flow split than the cavity equivalence ratio. This finding is consistent with that of Barringer [32, 33] where increases in cooling air mass flow directly correlated to increased profile

113

skews. With the UCC application, cooling air is analogous to the cavity flow where

increased cavity flows caused the maximum exit plane pressure to deviate from the

pressure drop across the combustor much quicker as demonstrated in the 80/20 case in

Figure 4.12a.

(a)   (b)
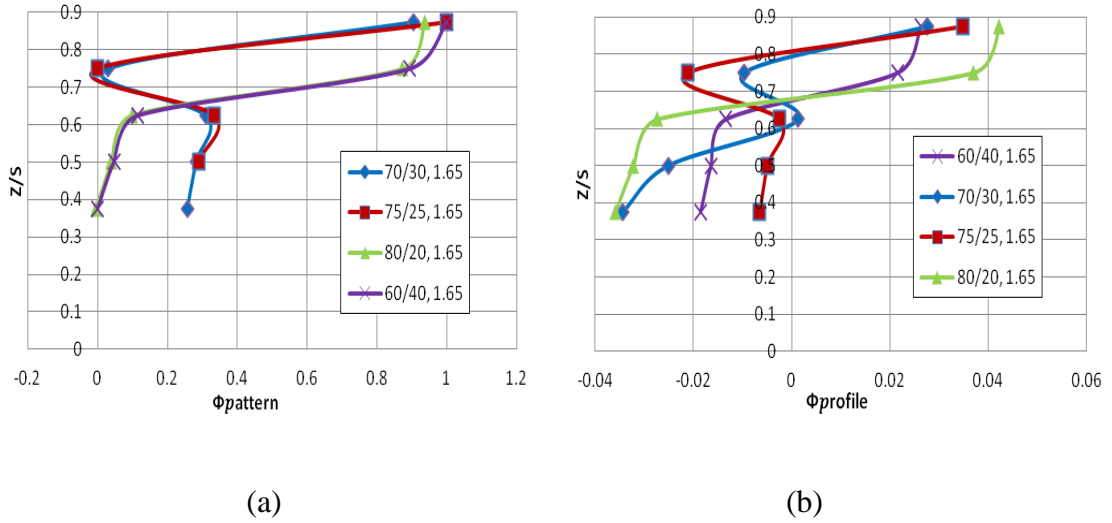
Figure 4.12. a) Pattern and b) profile factors for 60/40, 70/30, 75/25, and 80/20 flow
splits for equivalence ratio of 1.65.

4.2.3 Total Pressure Instrumentation Scheme Comparison

Section 3.4.1 outlined differences in total pressure ports used throughout the

AFIT UCC. This section is intended to provide an analysis of how the two different style

probes performed through the data collection history. Table 4.2 outlines some of the

measurements produced and the locations of those measurements. The measurements

were made in terms of differential pressure (P-P_{atm}) from the atmospheric pressure. In

comparing the measurements, a noticeable difference occurred in the differential pressure

output of the cavity pitot tube style probes from 29 Jan 14 to 30 Jan 14. The cavity

measurements taken with the pitot tube style probes on 30 Jan 14 is noticeably less than

the SS style probes. Important to note is the test conditions from date to date are not

consistent and the disparity in measurements provided by the two different style probes

from day to day is the takeaway. It is believed that the cavity heat forced the small EDM

machined holes to swell on the pitot style tubes. This swelling then closed the hole

diameter and resulted in a smaller measurements. Data from this date forward was

collected using the SS bent tube style. At the exit plane however, the heat did not cause a

decrease in the pitot style tube EDM holes and the measured results stayed consistent

from date to date.

Table 4.2. Comparison of total pressure instrumentation schemes.

Style Probe	SS Bent	Pitot	SS Bent	Pitot
Date	29 Jan 14	29 Jan 14	30 Jan 14	30 Jan 14
¼ Cav $P\text{-}P_{atm}$	0.3193	0.3255	1.1192	0.2438
½ Cav $P\text{-}P_{atm}$	0.3189	0.3179	0.7899	0.00425
Exit $P\text{-}P_{atm}$	0.1959	-0.0022	1.0178	-0.0028

4.3   UCC System Losses and Rayleigh Losses

The identification of UCC system losses and Rayleigh losses is paramount in the

understanding of how best to integrate the UCC into a traditional axial engine. In an

axial engine, air is supplied to the combustor via one source, not two independent sources

as done throughout this study.   Because air flow comes from a single common upstream

source, that source will eventually be split to fill the UCC cavity and core flows. An

understanding of the pressure drop across the UCC hardware components is essential for

the design and development of the hardware necessary for diffusing the single air source

into core and cavity air flows. This research will identify the component by component

losses of the AFIT UCC.

The Rayleigh loss study attempts to further characterize the UCC's performance by quantifying the pressure drop from inlet to exit resulting from heating a constant volume of flow. In previous research, Wilson [5] designed and tested two centerbodies and concluded that his LLCB design was most effective at mitigating the overall UCC Rayleigh pressure loss. However, Wilson's [5] quantification of Rayleigh pressure loss was hindered by not running flows at truly representative combustor inlet Mach numbers (approximately 0.3). The lack of air supplied by the COAL Lab hindered the available inlet Mach number thus reducing the amount fuel available for burning in the UCC cavity. This research also suffered from generating low inlet Mach numbers and therefore serves as a supplement to the results provided by Wilson [5].

4.3.1   UCC System Losses

A comparison of the pressure drop between the air plenum and the UCC cavity as a function of the pressure drop from the inlet to the exit will shed light upon which core/cavity mass flow splits and which total bulk air masses provide the most favorable pressure gradient. Again, a favorable pressure gradient moving from air plenum to UCC cavity is desired so as to continue to drive the flow from inlet to exit with flow coming from a single upstream source. The main air flow areas associated with the main passage of flow are shown in Figure 4.13.
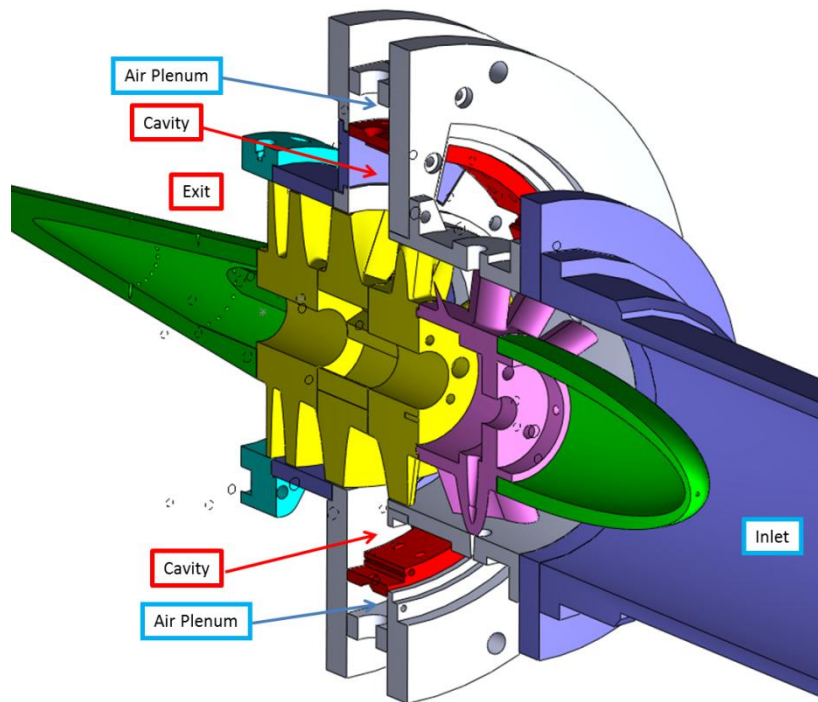
Figure 4.13. UCC flow path hardware components.

Comparing the total pressure drop from air plenum to exit plane against the total pressure drop from inlet to exit amongst three different mass flow splits, the relationship appears linear regardless of mass flow split. The linear relationships in Figure 4.14 indicate that the growth in pressure drop across the air plenum to the exit is the same amount as the growth in the pressure drop from inlet to exit. Because the relationship maintains a slope of less than one, a slightly larger pressure drop is experienced from inlet to exit for increases in pressure drop from plenum to exit. This is ideal as the potential for total pressure drop from inlet to exit should be greater across the UCC so as to drive the flow from inlet to exit. Should the pressure drop from air plenum to exit be

117

larger, the flow may become stagnate as it fights against an unfavorable pressure gradient moving from inlet to air plenum.
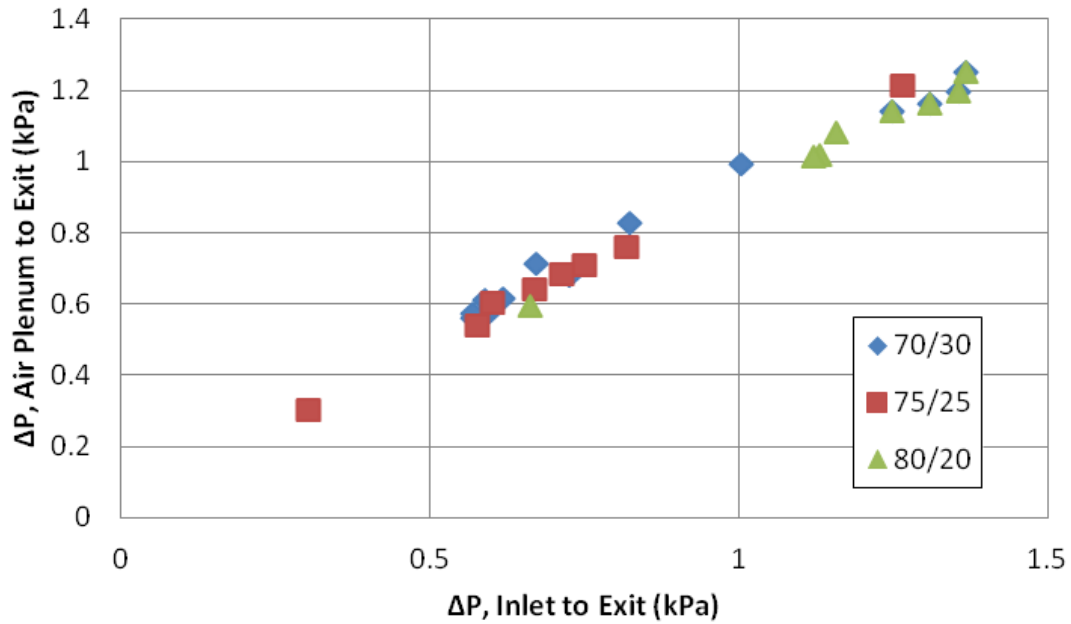
Figure 4.14. Linear relationship amongst pressure drops from air plenum to exit and inlet to exit across different mass flow splits.

Examining the same two total pressure drops across different amounts of total bulk air mass, the linear relationship is maintained as seen Figure 4.15. This is positive in the fact that the flow has an impetus to move from inlet to exit without regard for the mass flow split or the total bulk air mass.
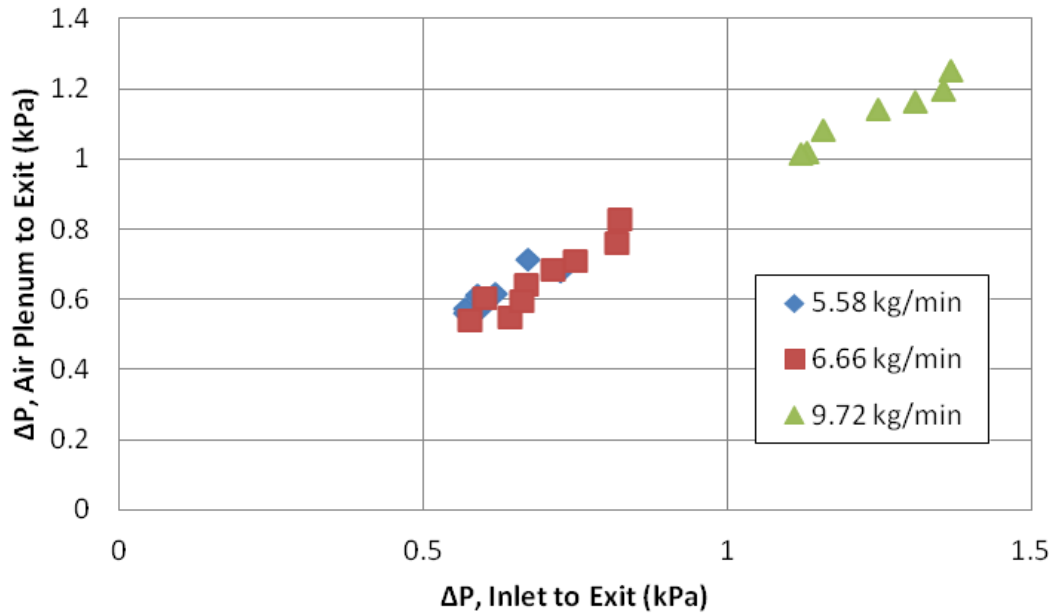
Figure 4.15. Linear relationship amongst pressure drops from air plenum to exit and inlet to exit across different bulk air masses.

4.3.2   UCC Rayleigh Losses

The issues surrounding the quantification of Rayleigh losses for the AFIT UCC have involved low inlet and exit Mach numbers due to a lack of mass flow generation at the inlet. To be truly representative of traditional axial combustors, the AFIT UCC attempts to simulate the flow exiting the compressor EGV at Mach = 0.3. Traditional axial combustors receive air at Mach = 0.1. The only upgrade to the COAL lab from the work performed by Wilson [5] to help in this area was the addition of a third mass flow controller to increase the amount of fuel available for burning at larger cavity air mass flow rates.

The Rayleigh loss results from this study as well as the corresponding inlet and exit Mach numbers are found in Table 4.3. Like the results found in Wilson [5], the largest Rayleigh losses correspond to the largest exit Mach numbers generated at an 80/20 flow

split. The largest Rayleigh loss generated at the 80/20 flow split by Wilson [5] was

4.19% at a cavity equivalence ratio of 1.82 compared to 5.34% at a cavity equivalence

ratio of 1.76 in this study. The addition of the third mass flow controller allowed this

study to generate a Rayleigh loss of 3.41% at a cavity equivalence ratio of 2.21 compared

to Wilson [5] who could not generate cavity equivalence ratios from 1.5 to 2.0 at the

70/30 mass flow split. The average inlet Mach numbers shown below remain low given

COAL Lab core air flow limitations. Inlet Mach numbers are computed at the area

behind the UCC pre-swirler because this component mimics the flow exiting the last

compressor stage and the area change from the UCC inlet to post pre-swirler is

significant, 0.0077 m^2 to 0.0029 m^2. This change in area led to inlet Mach numbers from

0.062 to 0.098 across the conditions listed in Table 4.3. The main COAL Lab

compressor could not maintain the appropriate air mass flow rate to generate more

representative inlet Mach numbers (i.e. $M = 0.3$). The storage tank housing the needed

air depletes too fast for any stable conditions to be maintained.

Table 4.3. Rayleigh loss study results.

Core Mass Flow Rate kg/min	Cavity Mass Flow Rate kg/min	Core /Cavity Flow Split %/%	Avg Inlet Mach	Avg Exit Mach	Max Rayleigh Loss (%)
3.96	1.62	70/30	0.062	0.232	3.41
5.58	1.62	75/25	0.077	0.251	3.57
7.92	1.80	80/20	0.098	0.327	5.34

Running non-reacting flows to capture UCC aerodynamic losses and then reacting

flows to capture losses due to heat addition, Rayleigh pressure losses were quantified as

the difference in losses. Figure 4.16a shows the non-reacting and reacting flow pressure

losses and where Rayleigh loss occurs with each point representing a change in the cavity

equivalence ratio. Larger core flow percentages increased pressure losses at lower exit

temperatures. This is largely due to the increased amount of air quenching the heat from the combustion reactions quicker than mass flow splits with lower core flow percentages. Figure 4.16b shows the pressure loss for the 80/20 and 70/30 mass flow splits for differing amounts of total bulk air mass. With respect to the 80/20 flow split condition, inlet to exit pressure loss grows with increases in total bulk air mass. However, the 70/30 flow split condition does not see as much of a change in pressure loss with increases in the total bulk air mass. This indicates that the 80/20 flow split condition is more sensitive to changes in the total bulk air mass than the 70/30 flow split condition. Furthermore, Rayleigh loss is more significant at the 80/20 flow split condition and the amount of loss is further dependent upon the total bulk air mass.
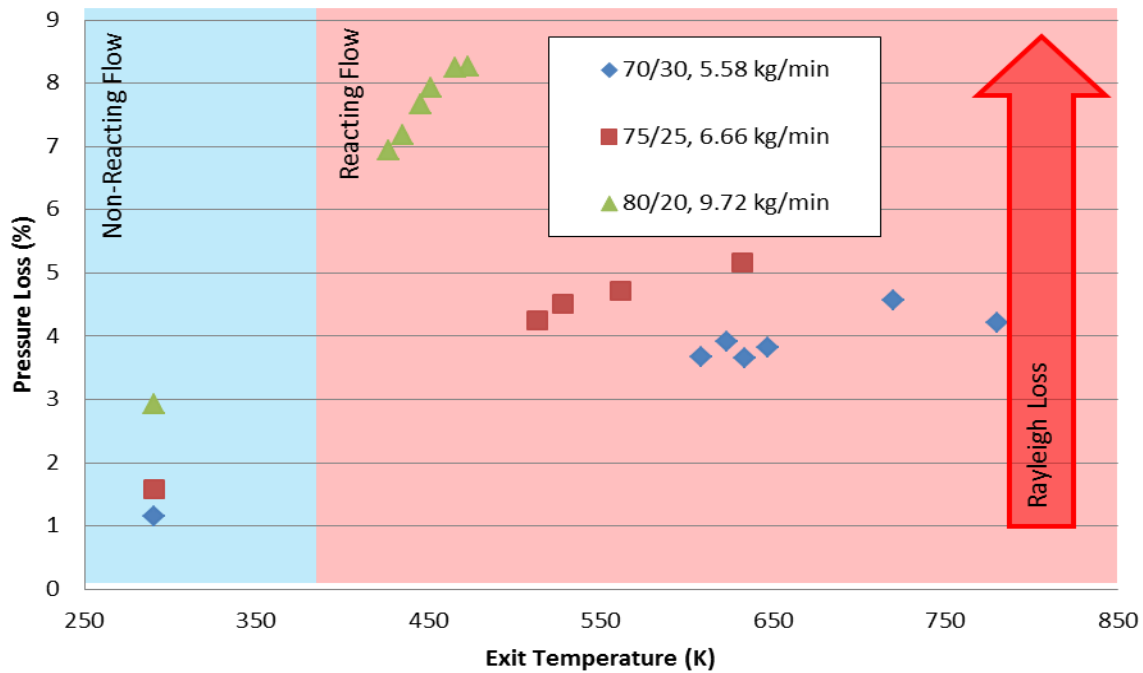
(a)
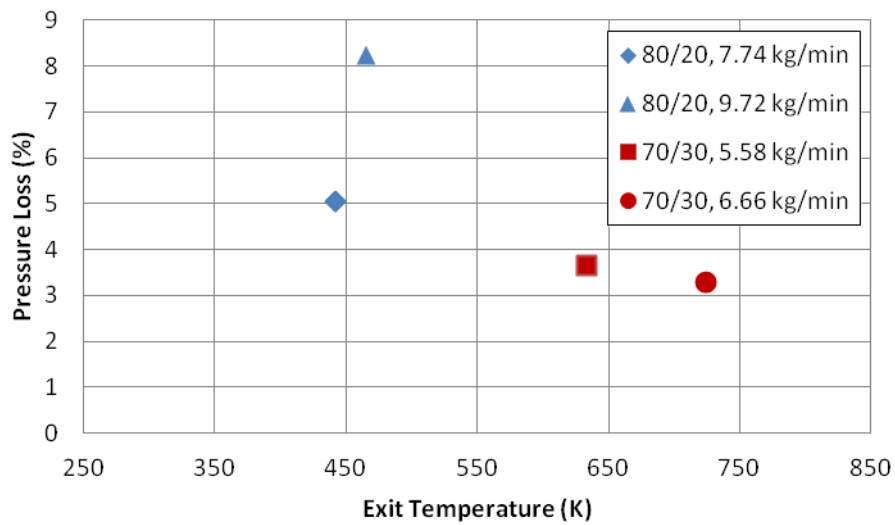
(b)

Figure 4.16. a) Resulting pressure loss from reacting and non-reacting flows and b) pressure loss at common flow splits with differing amounts of total bulk air mass.

122

Pressure losses resulting from increases in the exit Mach number are shown in Figure 4.17a. Higher exit Mach numbers were achieved at the largest total bulk flow condition corresponding to the larger core flow percentage. Each data point of Figure 4.17a corresponds to a unique cavity equivalence ratio. The pressure loss at each cavity equivalence ratio is shown in Figure 4.17b. As the cavity equivalence ratio increases, the resulting pressure loss increases as well. The richest cavity equivalence ratios for each respective flow split indicate reduced pressure losses as these points begin to enter the UCCs region of decreasing stability.

(a)   (b)
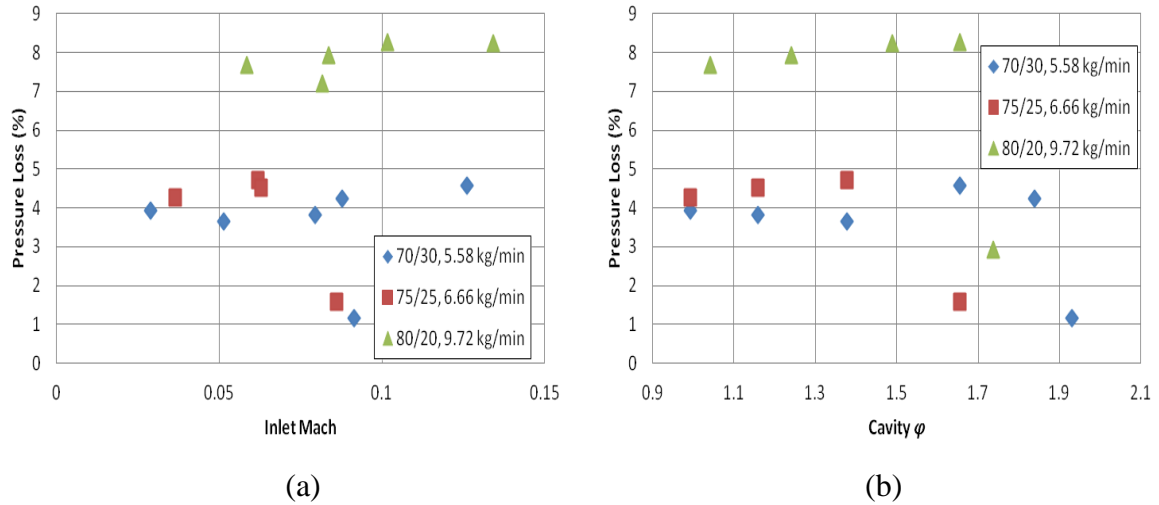
Figure 4.17. Pressure loss as a function of a) exit Mach number and b) cavity equivalence ratio.

4.4. Emissions Analysis

An emissions analysis was performed on the AFIT UCC combustor using the CAI analyzer described in Section 3.5. The analysis was performed to measure the combustion performance of the AFIT UCC with changes to three specific operating parameters: cavity equivalence ratio, mass flow ratio and the total combustor air mass.

The emissions analysis should shed light upon the shapes of the thermal and pressure exit profiles.

To quantify the emissions seen across the exit span, the set-up shown in Section 3.5.2 was used to collect emissions specimens from six span-wise locations for a 70/30 mass flow split running a bulk air mass of 6.66 kg/min at a cavity equivalence ratio of 1.65. The percentages of total analyzed volume collected in 20 second intervals at each span-wise location of UHCs, CO_2, CO, and O_2 are shown in Table 4.4. Overall, the percentage of UHCs appears lower than the other analyzed species. This result is due to the relative small amount of fuel in the flow compared to the overall total air mass which is naturally rich with respect to CO_2, CO, and O_2 molecules. Moving from ID to OD, percentages of UHCs and CO tradeoff as the combustion process becomes more efficient. The OD span-wise locations boast the most efficient burning as UHCs are completely absent in the collected volume.

Table 4.4. Percentages of emissions species at span-wise locations across exit plane.

% Span ID to OD	16	32	48	64	80	96
UHC %	0.0077	0.0046	0.0014	0.0008	0	0
CO_2 %	1.231	1.245	1.466	2.089	3.296	4.39
CO %	0.339	0.202	0.239	0.332	0.769	1.022
O_2 %	19.312	19.232	19.143	19.108	17.858	16.363

The percentages of the UHC and CO species are used to compute the combustion efficiency per Equation 3.6. Configuring the single channel emissions probe at mid exit span, cavity equivalence ratio sweeps were conducted to study the resulting emissions. Figure 4.18 shows combustion efficiency as a function of the cavity equivalence ratio for two unique flow splits. Moving from left to right, combustion efficiency decreases for increases in cavity equivalence ratio. At an equivalence ratio of 1.65 both flow splits

show an improvement in combustion efficiency. The efficiency then drops again while the cavity becomes richer. This sudden improvement in efficiency suggests a preferential operating cavity equivalence ratio of 1.65. Ideally, combustion efficiency should improve to a point with increases in cavity equivalence ratio and then begin to fade as the cavity becomes too rich.
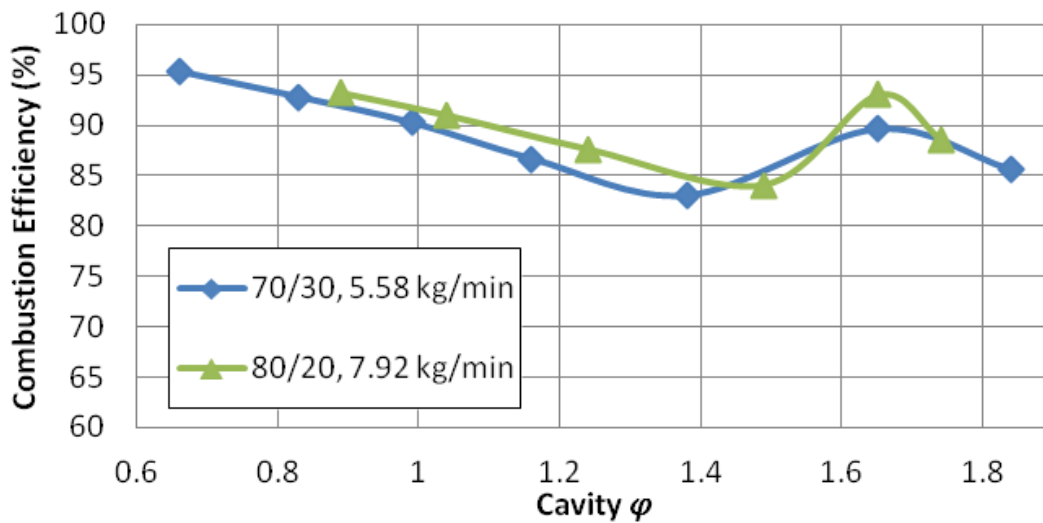
Figure 4.18. Combustion efficiency as a function of cavity equivalence ratio.

Studying the tradeoff among UHC and CO emissions sheds light upon how the combustion process occurs over a range of cavity equivalence ratios. Figure 4.19 shows the UHC emissions index (EI) as function of the CO EI for two distinct mass flow splits. Each data point from left to right corresponds to a richer and richer cavity equivalence ratio. Moving from left to right, the CO EI reaches a maximum while the number of UHCs available for burning increases. This helps to explain why efficiency begins to suffer with richer and richer cavity equivalence ratios as less and less UHCs are converted to combustion by-products such as CO.
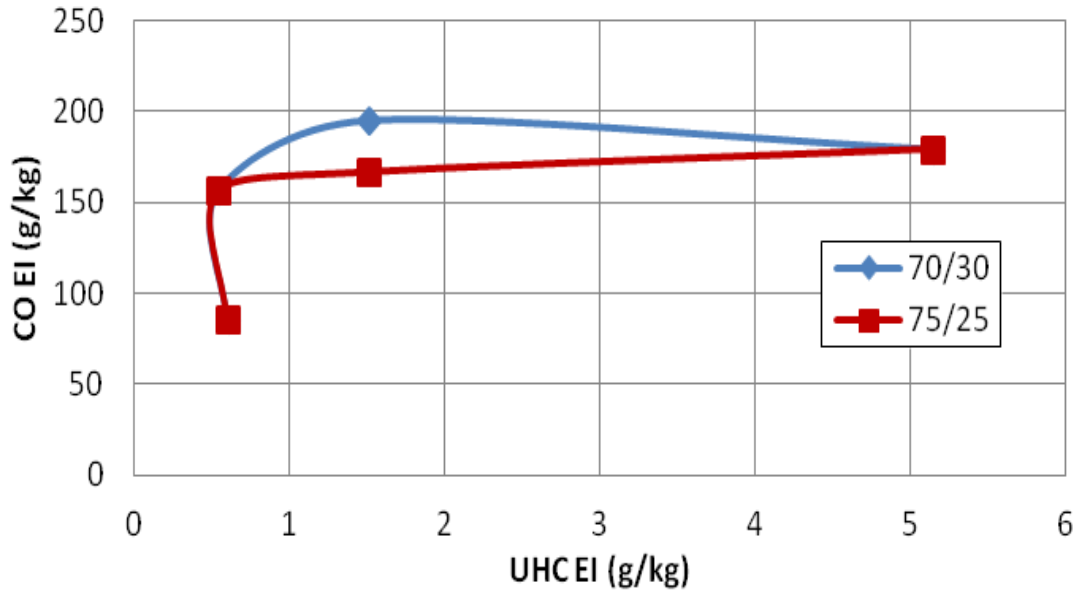
Figure 4.19. Emissions index tradeoff among UHCs and CO.

Further emissions studies are discussed in the following sections using the set-up shown in Figure 3.24. These studies compare thermal and pressure profiles with combustion efficiency as a function of changes to cavity equivlance ratio, mass flow ratio, and the total combustor air mass.

4.5   Influence of Cavity Equivalence Ratio on Emissions and Exit Profiles

While maintaining the same bulk air mass of 6.66 kg/min and manipulating the mass flow split at a constant fuel flow rate of 63 SLPM, the cavity equivalence ratio is forced to change. A study of the resulting combustion efficiency is shown in Figure 4.20a. Looking across the span from ID to OD, lower mass flow splits struggle to maintain combustion efficiency as seen with the 70/30 and 75/25 mass flow splits. The 80/20 split on the other hand improves its efficiency. The corresponding thermal profile in Figure 4.20b shows the largest heat relesase for smaller amounts of core flow. One

would expect that as combustion efficiency drops, so too would the resulting heat release as is the case toward the OD.

The corresponding pressure profile in Figure 4.20c for the 80/20 flow split lags behind the 70/30 and 75/25 profiles at the ID and OD. One may presume that as the core mass flow increases, a slippage of air from the core flow comes up through the hybrid centerbody vane passages into the cavity. This slippage of air from core to cavity would explain why the pressure profile never regains its momentum to catch up to the lower percentage core flows. This would improve combustion efficiency across the span as more air within the cavity forces the equivalence ratio closer to zero and quenches the heat expected from a higher equivalence ratio.
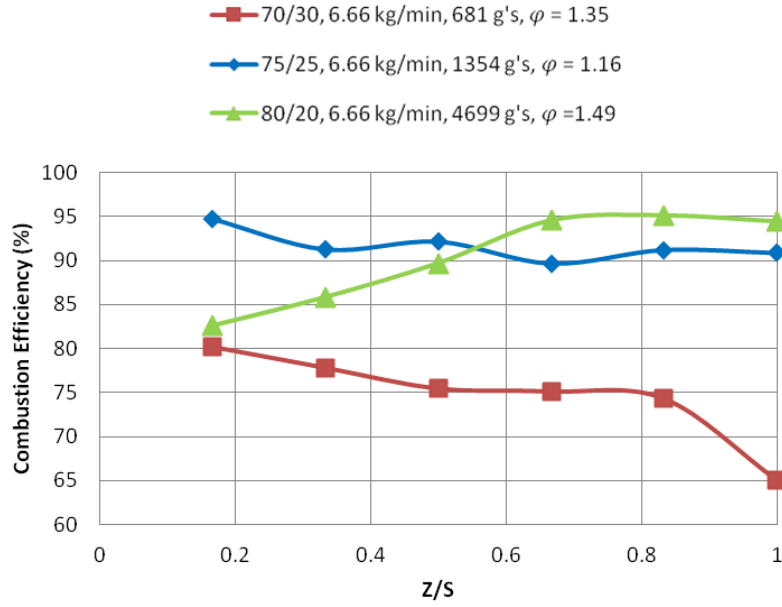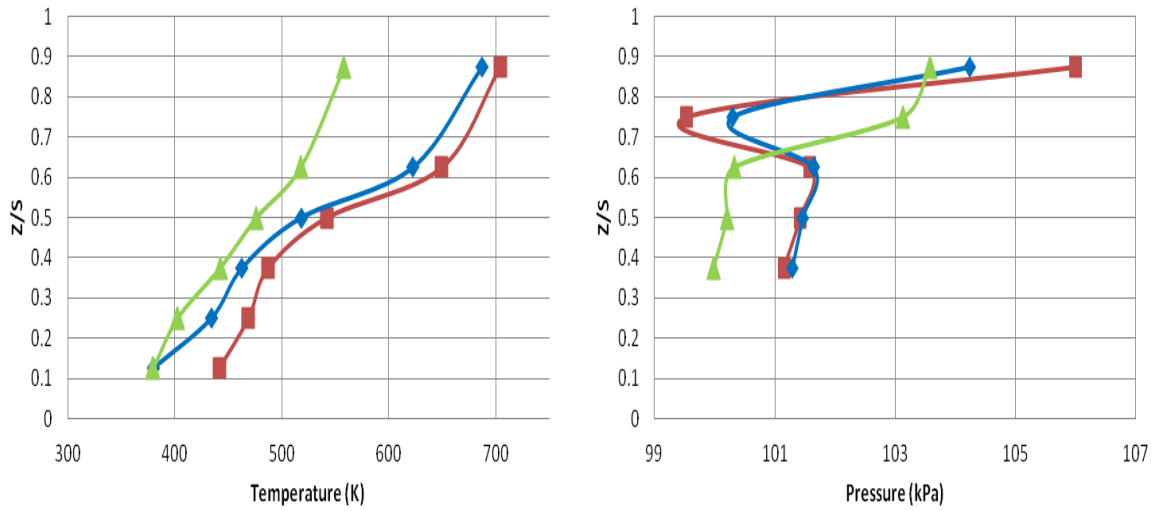
Figure 4.20. Influence of cavity equivalence ratio on a) combustion efficiency, b) thermal profiles and c) pressure profiles.

4.6   Influence of Mass Flow Split on Emissions and Exit Profiles

By maintaining a constant fuel flow rate of 90 SLPM and a constant cavity air

mass flow, the cavity equivalence ratio is maintained. Changing the distribution of mass

flow between core and cavity at a constant cavity quivalence ratio therefore results in different bulk air mass flow rates with different mass flow splits. The resulting emissions are shown in Figure 4.21a for three mass flow rates at unique bulk air mass flows. Overall, larger bulk air masses at larger core mass flow performed better in terms of combustion efficiency at a cavity equivalence ratio of 1.84. This cavity equivalence ratio appears too rich for the 70/30 mass flow split case as the combustion efficiency drops below 90% moving across the exit span from ID to OD.

The magnitude of the thermal profiles seen in Figure 4.21b again follow the trend shown above in Figure 4.21b where larger core air mass flows correspond to smaller amounts of heat release. Although the 70/30 case exhibits the worst combustion efficiency, the heat release remains higher. To explain this, the amount of cavity g-loading shows that for smaller g-loads, heat release in incresed. The larger core air mass flows exhibit larger cavity g-loads which lead to increased cavity residence times. Therefore, the increased residence time improves the combustion efficiency however, the magnitude of the heat release suffers as hot combustion products stay resident in the cavity longer. Hence, the heat release from the more efficient combustion processes is transferred to the cavity walls versus out the exit plane.

The pressure profiles in Figure 4.21c show that again, the momentum of larger core air mass flows lags behind that of smaller core air mass flows. Considering the notion of air slipping from the the hybrid vane passages into the cavity with larger core air flows may explain this loss in momentum at the exit plane. This air slippage may also explain the dramatic increase in cavity g-loading for the larger core air mass flows. The

increased amount of cavity air would push g-loading to levels higher than expected and

improve the combustion efficiencies of fuel rich cavities as more air is available to burn.
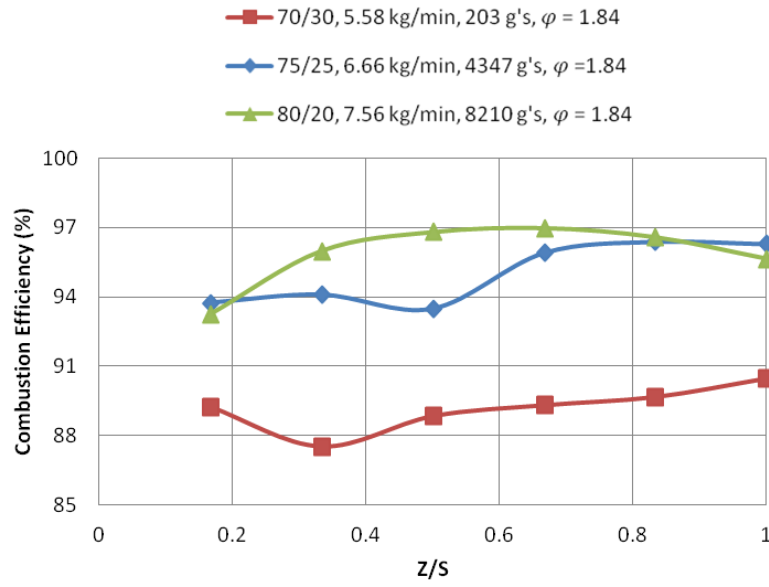
(a)
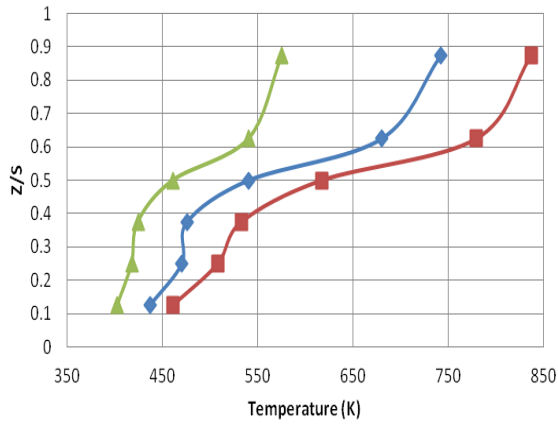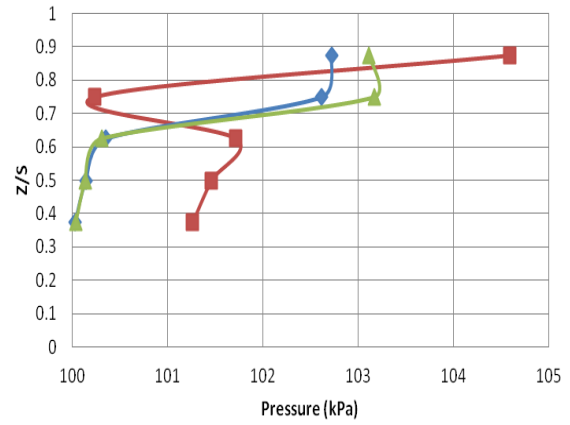
(b)   (c)

Figure 4.21. Influence of mass flow split on a) combustion efficiency, b) thermal profiles and c) pressure profiles.

4.7   Influence of Combustor Air Mass Flow on Emissions and Exit Profiles

The combustor air mass flow or bulk air mass flow combines the core and cavity air mass flow rates. The combustion efficiency associated with increases in bulk air mass flow at the same mass flow split is shown in Figure 4.22a. The trend across all three bulk air mass flows is consistent from ID to OD. Because the bulk air mass flow differs for one mass flow split, the cavity equivalence ratio could not be maintained for a constant 90 SLPM fuel flow rate across all three cases. Combustion efficiency suffers at the OD for all three cases as the heavier combustion byproducts gravitate toward the OD of the hybrid vane passages carrying hot gas from the cavity to the exit plane.

The thermal profiles in Figure 4.22b look uniform given the same mass flow split. As discussed previously, the thermal profiles are more sensitive to changes in mass flow split and will maintain the same profile for the same mass flow split. Despite having a poor combustion efficiency at the OD, the magnitude of the heat release is highest at the OD. There appears to be a lag in the thermal profiles where the point of maximum heat release does not occur at the point of maximum combustion efficiency. This makes sense considering that there exists some level of combustion occurring within the hybrid vane passages as the flow moves axially from the cavity to the exit plane.

As was the case for the thermal profiles, the pressure profiles in Figure 4.22c appear nearly uniform in profile shape given the same mass flow split across all three amounts of bulk air mass. Again, the momenutm of the largest bulk air mass (7.56 kg/min) lags behind the momentum of the smaller bulk air masses suggesting that too much core air mass flow results in a slippage of air from the core into the cavity. This slippage may explain why the combustion efficiency of the 6.66 kg/min case is lower

than the 7.56 kg/min case. The 7.56 kg/min case may be dumping air into the cavity

causing an increase in combustion efficiency across the exit plane whereas the 6.66

kg/min case does not have enough core flow momentum for air to slip into the cavity.

This concept of air slippage from core to cavity at increased bulk air masses and

increased core air mass flows requires further investigation.

(a)
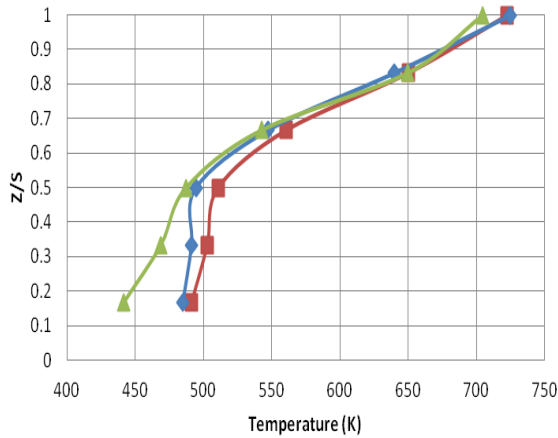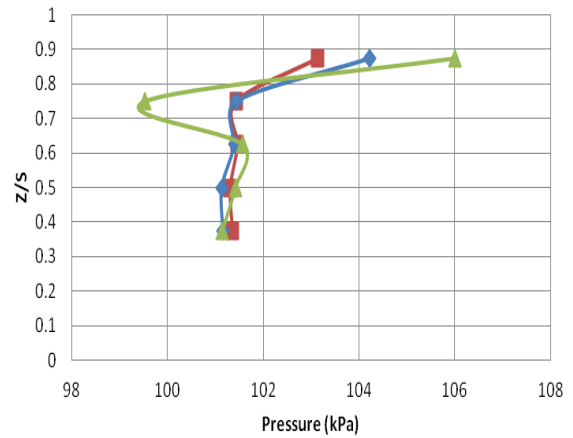
(b)   (c)

Figure 4.22. Influence of bulk air mass flow on a) combustion efficiency, b) thermal
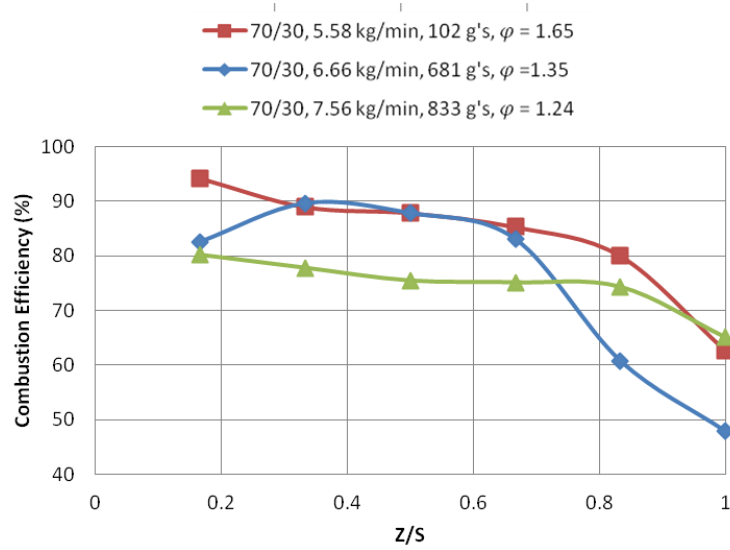profiles and c) pressure profiles.

V. Conclusions and Recommendations

The main research objectives of this effort were accomplished with a number of equipment upgrades and additions to support the UCC and the surrounding COAL Lab. Contributions were made in the characterizing the AFIT UCC operational performance in the form of identifying: thermal and pressure exit profiles as well as the emissions performance, key system losses in the form of pressure drops across specific flow paths and Rayleigh losses as well as the emissions performance. This chapter summarizes the conclusions and lessons learned from the testing and results discussed previously.

5.1   Upgrades

5.1.1   COAL Lab Equipment

The upgraded fuel flow capabilities as well as the addition of key emissions analysis equipment increased the COAL Lab's overall functionality. The addition of a third MFC allowed the research to carry on at increased cavity equivalence ratios with increased amounts of air. The development of a single channel emissions probe, a five channel emissions probe, a heated line extension, and a high temperature solenoid switch will greatly enhance the facility's emissions analysis capabilities which were not in place previously.

5.1.2   UCC Hardware

Several hardware upgrades were made to the UCC itself for improvements to performance as well as instrumentation. The use of the fuel baffles and the fuel baffle additions allowed for the UCC to operate with a more diffuse injection pattern, boosting the level of g-loading experienced within the cavity. The development of an additional

133

exit plane instrumentation ring helped allow for real-time analysis of emissions, thermal and pressure profiles all at once. This contributed greatly to the flexibility of data collected as thermal and pressure profiles may now be compared to emissions performance all at the same test conditions.

5.1.3   Instrumentation

The development of new total pressure pitot tube style probes offered a unique solution aimed at providing more accurate measurements for total pressure within the UCC cavity as well as at the exit plane. The addition of the pitot probe holders utilizing a ball bearing plunger screw at the exit plane alleviated issues regarding probe installation as well configuration change outs. The challenges associated with maintaining good measurements relative to the SS bent probes involved the sizing of the EDM holes along the sides of the probes. Increasing the size of these holes to alleviate the swelling of the holes in hot environments may increase the probe's survivability. The hole size will have to be balanced with the precision of the measurement, making sure not to take an average of the total and static pressure around the probe.

5.2   Testing Conclusions

The main research objectives of characterizing the exit thermal and pressure profiles, system total pressure losses and emissions were each completed with a variety of observations and lessons learned. The results of this effort should serve as a baseline for future research.

5.2.1. Exit Profiles

The resulting thermal and pressure profiles showed sensitivities mainly toward the mass flow split. The four core/cavity mass flow splits studied included 60/40, 70/30, 75/25, and 80/20. The magnitudes of the profiles were largely a function of the cavity equivalence ratio and the momentum of the core flow for the thermal profiles and pressure profiles respectively. The thermal and pressure profiles maintained an OD skew with a maximum exit temperature of 900K at a 60/40 flow split and maximum exit total pressure of 108 kPa at an 80/20 flow split. Using the non-dimensional pattern and profile factors, the profile shapes appeared stacked upon one another when plotted as a function of cavity equivalence ratio. The profile's sensitivity to changes in mass flow ratio were realized when the pattern and profile factors showed increased variability among profile shape at different mass flow ratios.

5.2.2 System Losses and Rayleigh Loss

The almost linear relationship of total pressure drop from air plenum to exit and inlet to exit sheds a positive light on the eventual operation of the AFIT UCC from a single upstream air source. This shows that the flow is driven through the UCC with an adequate total pressure drop from inlet to exit. A maximum inlet to exit total pressure loss of 8.3% was realized at an 80/20 mass flow split and 9.72 kg/min total combustor air mass flow rate. The one area of concern that still remains is the pressure loss due to heat addition at high Mach number (Rayleigh loss). Because the COAL Lab compressor could not replicate compressor EGV flows at Mach = 0.3 the results presented in this study remain too low. A maximum inlet to exit Rayleigh total pressure loss of 5.34% was realized at an 80/20 flow split condition and an inlet Mach number of 0.13. Higher

inlet Mach numbers will lead to higher exit Mach numbers and eventually more total

pressure loss. The highest sustainable core mass flow rate with the existing compressor

was 7.92 kg/min. This mass flow rate is only 22% of what is capable of flowing through

the core mass flow air lines within the COAL Lab.

5.2.3   Emissions Analysis

The emissions results provided in this study are the first documented for the AFIT

UCC. The equipment modifications discussed previously allowed for the quantification

of emissions at the exit plane. The CAI analyzer performed consistently throughout

testing and offers the COAL Lab a variety of emissions analysis flexibility. The results

showed that combustion efficiency was independent of the heat release at the exit plane.

The best emissions performers corresponded to the smallest amount of heat release and

poorest emissions performers corresponded to the maximum amount of heat release. The

80/20 flow split condition often proved to be the best emissions performer however, the

increased amount of core air flow appeared to quench the heat release experienced at the

exit plane. On the other hand, the 70/30 flow split often proved to be the poorest

emissions performer however, the relative lower amount of core air flow (compared to

the 80/20 flow split condition) allowed temperatures to increase beyond those of the best

emissions performer. In addition, combustion efficiency overall appeared to be more

sensitive to the mass flow ratio versus the total combustor air mass flow rate just as was

the case with the thermal and pressure exit profiles.

5.3   Recommendations for Future Work

Now that a baseline for the AFIT UCC performance has been established and

some of the parameters influencing that performance are beginning to be understood,

136

future work on the AFIT UCC should be made into optimizing the flow characteristics for passage to the turbine section. Further work is needed in the characterization of the exiting flow. This study showed that thermal profiles taken at different circumferential locations with the same test conditions yielded different profile shapes. The swirling nature of the hybrid centerbody vanes induces a swirl into the exiting hot gas. Further investigation of this swirling exit path may be done with CFD to understand the amount of swirl, whether or not that swirl is consistent, and how far downstream that swirl continues. This understanding will boost experimental efforts as researchers will better understand key areas of interest along the exit path. Parks [17] introduced the concept of unique vane cavities aimed at shaping exit profiles. With a CFD analysis indicating how the swirl pattern propagates, these unique vane cavity patterns may bring positive benefits to controlling the exiting flow.

In addition, the concept of air slippage from the core flow to the cavity requires further investigation. The large fluctuation of g-load for small changes in cavity equivalence ratio at increased amounts of core air mass flow is of concern. Often the measured g-load is higher than expected given a specific fuel flow rate and cavity air mass flow rate. Without understanding this consequence of air slippage from core to cavity, it is difficult to know what kind of g-loading to expect in the cavity. Consequently this has an impact upon the combustion efficiency as well as the thermal and pressure profiles. New centerbody designs or additional hardware to control this slippage may be necessary. The improved optical access of the UCC v3.0, discussed in Appendix C, may allow for identifying this phenomenon and understanding which mass flow splits and which total combustor air masses induce the slippage.

137

Finally, an integration of the COAL Lab's data acquisition systems is needed. The multiple systems involved with temperatures, pressures, and emissions combined with controls for fuel and air mass flow rates generates too much task saturation for a single operator. An integration of the UCC controls as well as the data acquisition systems will allow for more expansive research efforts.

RELATIVE RESPONSE FACTORS
(Methane to Other VOC Responses as Measured with a CAI Model 300HFID)

NUMBER	COMPOUND	CH4/X RATIO	C3H8/X RATIO
1	Acetaldehyde	0.52	0.40
2	Acetone	0.64	0.74
3	Acrylonitrile	0.79	0.61
4	Benzene	0.97	2.24
5	1,3 Butadiene	0.96	1.46
6	Butanone (MEK)	0.70	1.06
7	Carbon Tetrachloride	0.61	0.23
8	Chloroform	0.69	0.26
9	CS2	0.01	0.003
10	Desflurane	0.26	0.30
11	Enflurane	0.53	0.61
12	Ethane	1.00	0.77
13	Ethene	0.98	0.75
14	Ethanol	0.62	0.47
15	Ethyl Acetate	0.60	0.92
16	Freon 11	0.20	0.08
17	Freon 12	0.31	0.12
18	Freon R-134a	0.68	0.52
19	Glycol Ethers	0.21	0.16
20	Halothane	0.97	0.75
21	1,5 Hexadiene	0.97	2.24
22	n-Hexane	0.96	2.20
23	Isoflurane	0.38	0.44
24	Methane	1.00	0.38
25	Methanol	0.68	0.26
26	Methylene Chloride	0.70	0.27
27	Propane	0.87	1.00
28	Propanol	0.74	0.85
29	Sevoflurane	0.52	0.80
30	Styrene	0.86	2.64
31	Tetrachloroethene (PCE)	0.95	0.73
32	Tetrahydrofurane	0.63	0.96
33	1,1,1 Trichloroethane	1.04	0.80
34	Trichloroethene (TCE)	1.03	0.79
35	Toluene	0.94	2.52
36	Vinylidene Chloride	1.00	0.77
37	m-Xylene	0.90	2.75

The CH4 / X Ratio (or CH4 Relative Response Factors) were derived by calibrating a CAI Model 300HFID using 99.99% pure N2 as a zero gas and a certified methane / balance N2 span gas. Certified cylinders of other gases (also with N2 as a balance gas) were then introduced into the analyzer and the measured value recorded. The relative response factors were then calculated by the following:

$$\text{RELATIVE RESPONSE FACTOR} = \frac{\text{MEASURED VALUE}}{\text{PPM VALUE OF THE CYLINDER} \times \text{"B"}}$$

Where "B" = The number of carbons in the Brutto formula
(Example One: The Brutto formula for propane is C3H8. Therefore, "B" = 3)
(Example One: The Brutto formula for hexane is C6H14. Therefore, "B" = 6)

The C3H8 / X Ratio (or C3H8 Relative Response Factors) were then calculated by multiplying the CH4 Ratio for each gas by 1.15

Appendix B

Fuel MFC Calibration and Pressure Transducer Calibration

Calibrations for the three MKS type 1559 MFCs were performed with the BIOS Definer 220 which is capable of handling flows up to 30 SLPM. The BIOS Definer 1020 flow calibrator was not available for use to calibrate flows exceeding 30 SLPM. The curves proided for better accuracy of fuel mass flows by using a linear curve fit for the calibration. MFC 6 responded poorly to flows less than 15 SLPM. That data has been removed from the individual curve fit shown in Figure B.1b.
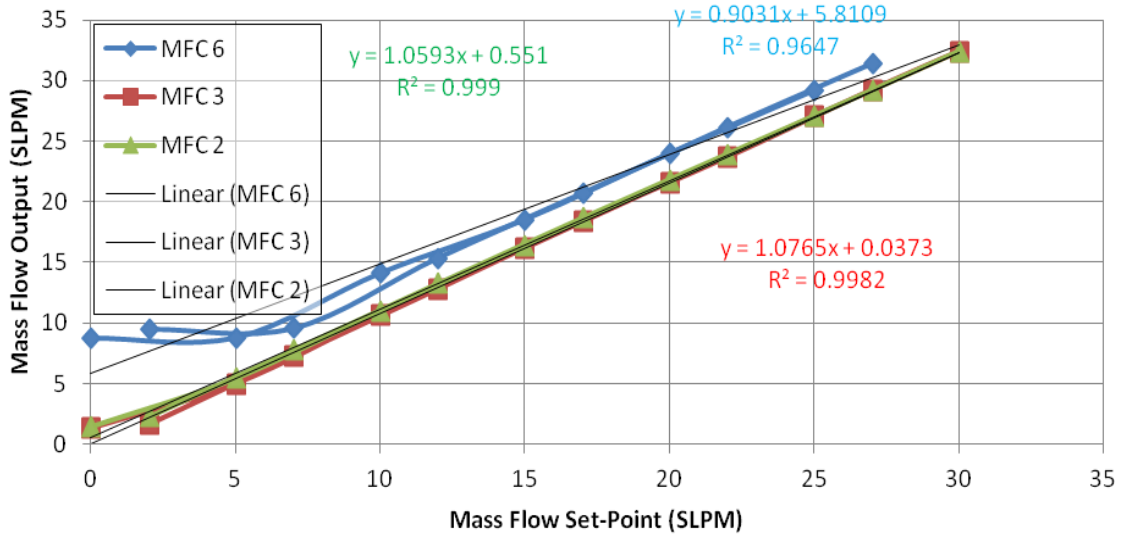
(a)
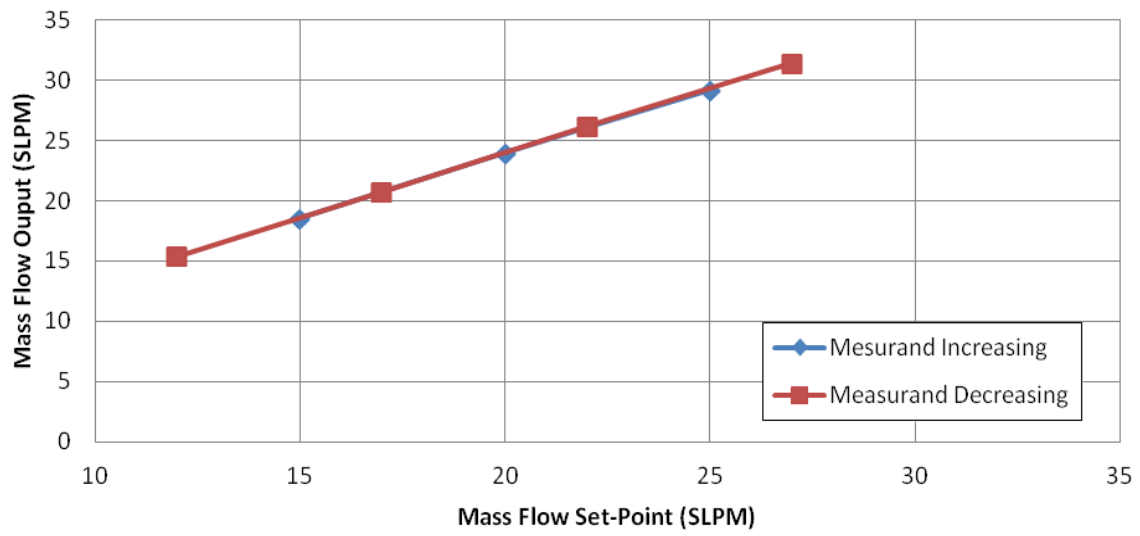
(a)
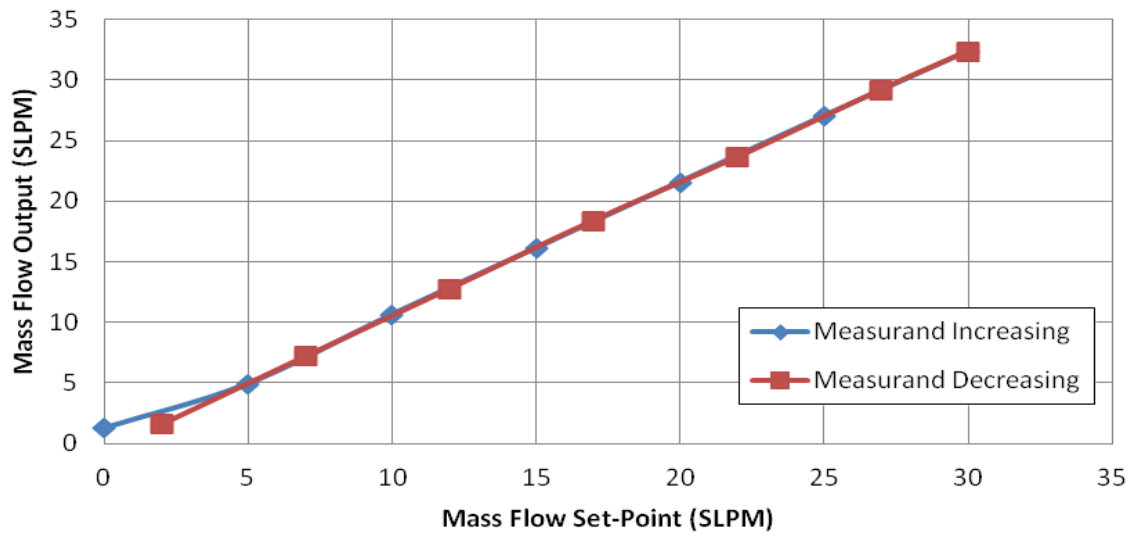
(c)
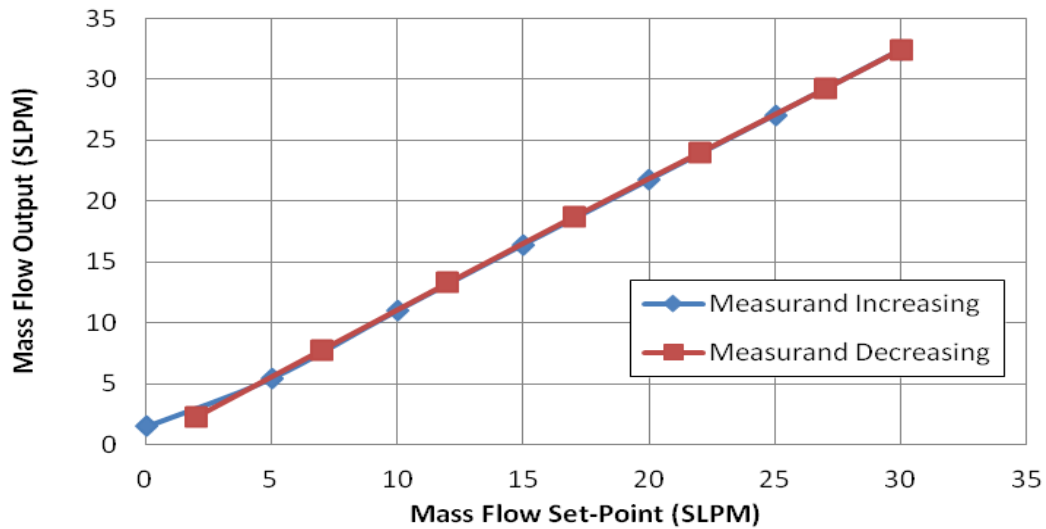
(d)

Figure B.1. Calibration curves for a) all three propane MFCs and individual calibration curves for b) MFC 6, c) MFC 3, and d) MFC 2.

The ESP-32 HD pressure transducer was also calibrated using a linear curve fit to provide better accuracy within the UCC static and total pressure measurement results. The transducer is rated to measure pressures ± 5 psid.
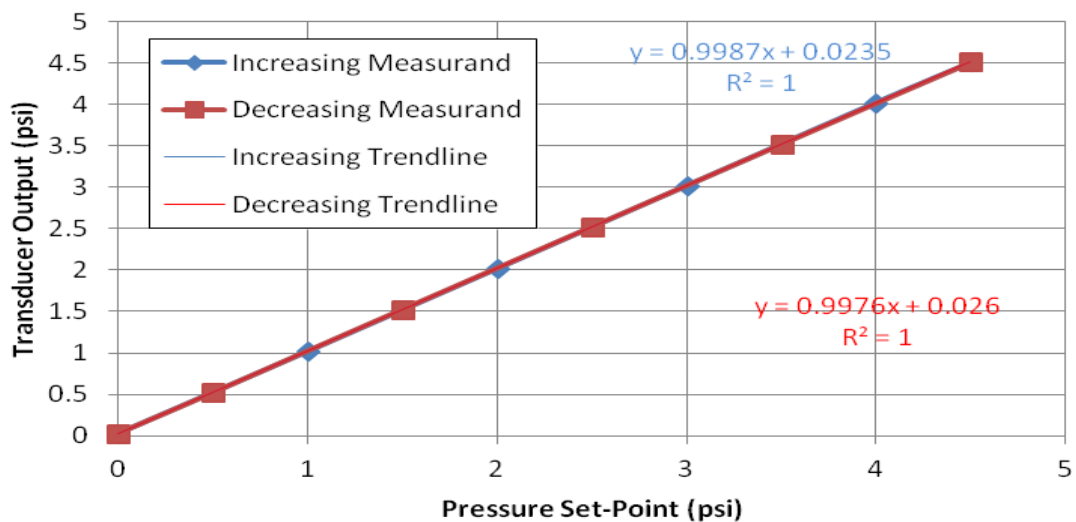
Figure B.2. ESP-32 HD pressure transducer calibration curve

Appendix C

AFIT UCC v3.0

While extremely modular and designed to accommodate multiple size combustion

rings, differing center body designs, and outfitted with the essential instrumentation port

locations, the initial AFIT UCC design by Wilson [5] is not ideal. The teardown and

assembly times associated with changing out combustion rings is approximately 90

minutes given the hardware associated with the design. Instrumentation ports, once

exposed to heat, weld together with the fittings holding various instrumentation set-ups.

To remove these fittings, the instrumentation plates need to be bored out and re-tapped

with the appropriate tap size. In addition and of primary concern, the front and rear

plates of the UCC have endured significant thermal fatigue cracking at the corner of the

plates' viewing windows. Figure 3.24 displays this cracking and shows the direction of

the cracking towards the ID wall.
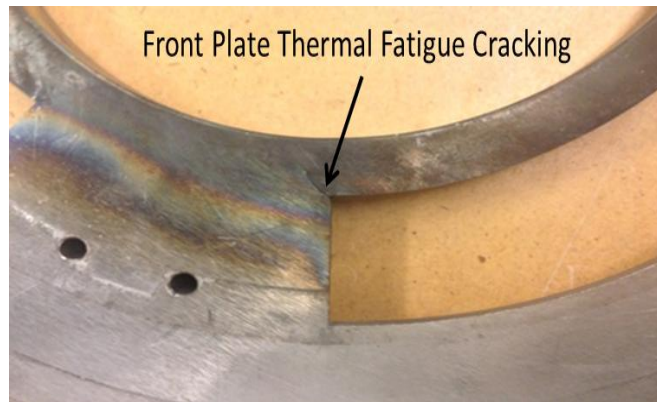
Figure C.1. Thermal fatigue cracking upon AFIT UCC v2.0 front plate.

This cracking was documented and taken into consideration for the design of the AFIT

UCC v3.0 UCC. The cracks shown above did not pose any significant threat to the

continued operation of the UCC as they did not penetrate through the entire width of the front and rear plates.

The evolution of the physical UCC design starts with the straight and curved sectional models used by Parks [17] (v1.0) which then evolved to the full annular design used by Wilson [5] (v2.0). In maintaining the design development, the AFIT UCC v3.0 was designed to address key procedural and fatigue issues associated with Wilson's [5] UCC v2.0 work.

The v3.0 UCC design shown in Figure 3.25 incorporates needed changes as proposed by Wilson [5] following his work which includes rounded edges about viewing window edges and instrumentation port block wedges. This will reduce the amount of corner point stresses experienced by the front and back plates and reduce the likelyhood of repeating the result seen in Figure 3.24. Moving from the center of the v3.0 UCC out, the combustion rings used in combination with the v2.0 UCC are identical to those being used in the v3.0 model. Hence, the shape and size of the radial burning cavity is consistent between the two models. The Fuel/Air Injection ring was increased from a 20.32 cm diameter to a 22.86 cm diameter. This increased ring diameter increases the area of the air plenum associated with the v2.0 UCC however, maintaining consistent air injection volumes between the two designs should not be difficult as the combustion ring hole sizes remain unchanged.
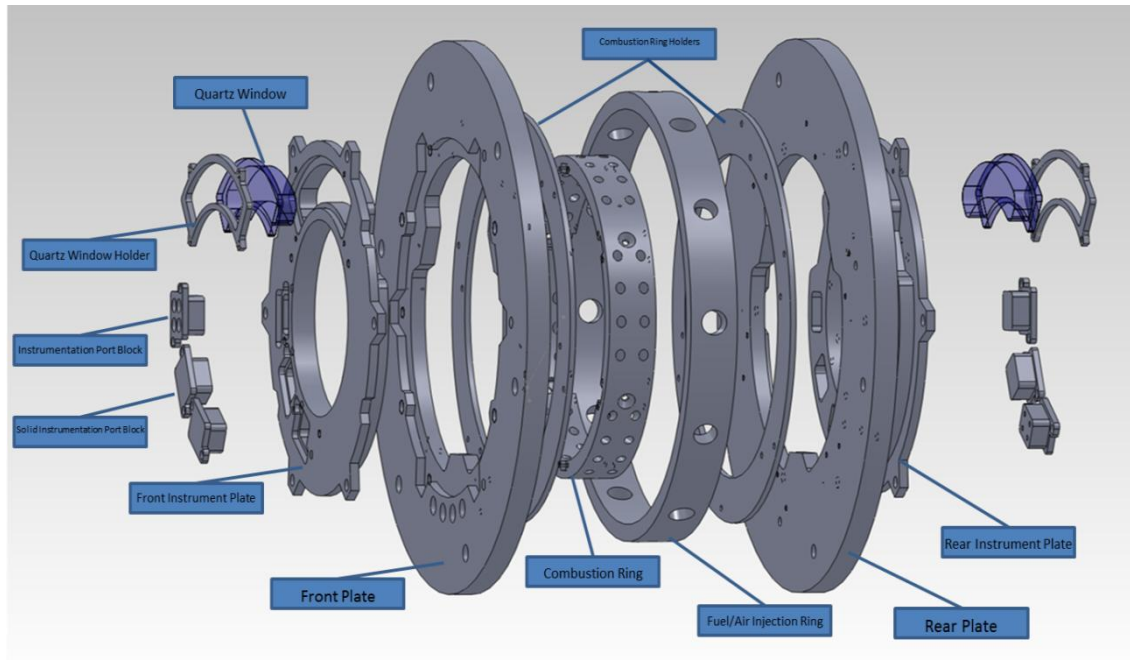
Figure C.2. AFIT UCC v3.0 UCC design in exploded view.

The increased Air/Fuel Injector ring diameter was necessary to allow for a unique UCC v3.0 feature, the Combustion Ring Holders. The 0.304 cm wide rings are intended to hold the combustion ring in place without the need for mounting hardware. The two rings will hold the combustion ring in place as it is sandwiched between the front and rear plates. The lack of hardware will significantly reduce the time required to perform a combustion ring change out.

Attached to the faces of the front and rear plates are front and rear instrumentation plates. The instrumentation plates sit within the front and rear plates and are attached with easily accessible hardware. This upgrade allows for the front and rear viewing windows to be clocked about any injector port for optical access versus the single three o'clock injector port with the v2.0 UCC model. In addition, the front and rear instrumentation plates allow for multiple instrumentation set-ups. The instrumentation

port blocks may be inserted in any of three different locations about the v3.0 faces: prior to the injection port, at the injector port, past the injector port. This gives the operator the ability to better categorize the flame structures existing about individual injection ports.

Finally, the UCC v3.0 will have the ability to perform a complete configuration change moving from combustor to ITB. The front plate of the UCC v3.0 is highly configurable to allow for a diffuser hook-up which allows for both the core and cavity flows to feed the UCC from one single source. The new front plate will also accommodate smaller air injection plates that induce the cavity swirl needed within the ITB circumferential cavity. The development of ITBs and their application is outlined by Conrad [38].

Bibliography

1. Mattingly, Jack D., William H. Heiser, and David T. Pratt. *Aircraft Engine Design*. 2nd. Reston, VA: American Institute of Aeronautics and Astronautics, 2002.

2. Mattingly, Jack D., *Elements of Propulsion: Gas Turbines and Rockets*. Reston, VA: American Institute of Aeronautics and Astronautics, 2006.

3. Zelina, J., Sturgess, G.J., and Shouse, D.T., "The Behavior of An Ultra –Compact Combustor (UCC) Based on Centrifugally-Enhanced Turbulent Burning Rates," *40th AIAA/ASME/SAE/ASEE Joint Propulsion Conference and Exhibit,* Fort Lauderdale, Florida, 2004, AIAA-2004-3541.

4. Bohan, B.T. and Polanka, M.D. "Analysis of Flow Migration in an Ultra-Compact Combustor" *Journal of Engineering for Gas Turbines and Power*, Vol. 135, May 2013, 051502 1-11.

5. Wilson, J.D., "Characterizing G-Loading, Swirl Direction, and Rayleigh Losses in an Ultra Compact Combustor," Master's Thesis, The Air Force Institute of Technology, WPAFB, OH. 2013.

6. Lewis, G.D., Shadowen, J.H., and Thayer, E.B., "Swirling Flow Combustion" Journal of Energy, Vol. 1. 1977.

7. Yonezawa, Y., Toh, H., Goto, S., and Obata, M., "Development of the Jet-Swirl High Loading Combustor," *26th AIAA/SAE/ASME/ASEE Joint Propulsion Conference,* Orlando, FL, AIAA-90-2451 (1990).

8. Sirignano, W. A., Delplanque, J. P., and Liu, F., "Selected Challenges in Jet and Rocket Engine Combustion Research," *33rd AIAA/ASME/SAE/ASEE Joint Propulsion Conference*, Seattle, Washington, 1997, AIAA-97-2701.

9. Anthenien, R. A., Mantz, R. A., Roquemore, W. M., and Sturgess, G. J., "Experimental Results for a Novel, High Swirl, Ultra Compact Combustor for Gas Turbine Engines," 2nd Joint Meeting of the U.S. Sections of the Combustion Institute, Oakland, California, March, 2001.

10. Zelina, J., Shouse, D. T., and Hancock, R. D., "Ultra-Compact Combustors for Advanced Gas Turbine Engines" 49th ASME Internation Gas Turbine and Aeroengine Congress and Exposition, GT2004-53155, Vienna, Austria, June 14-17, 2004.

11. Greenwood, R. T., "Numerical Analysis and Optimization of the Ultra-Compact Combustor," Graduate School of Engineering and Management, Air Force Institute of Technology, WPAFB, Ohio, Master's thesis, 2005.

12. Anisko, J., "Numerical Investigation of Cavity-Vane Interactions Within the Ultra-Compact Combustor," Graduate School of Engineering and Management, Air Force Institute of Technology, WPAFB, Ohio, Master's thesis, 2006.

13. Moenter, D. S., "Design and Numerical Simulation of Two Dimensional Ultracompact Combustor Model Sections for Experimental Observation of Cavity- Vane Flow Interactions," Graduate School of Engineering and Management, Air Force Institute of Technology, WPAFB, Ohio, Master's thesis, 2006.

14. Anderson, W. S., "Design, Construction, and Validation of the AFIT Small Scale Combustion Facility and Sectional Model of the Ultra-compact Combustor," Graduate School of Engineering and Management, Air Force Institute of Technology, WPAFB, Ohio, Master's thesis, 2007.

15. LeBay, K. D., "Characterization of Centrifugally-Loaded Flame Migration for Ultra-Compact Combustors," Graduate School of Engineering and Management, Air Force Institute of Technology, WPAFB, Ohio, Doctoral dissertation, 2011.

16. Blunck, D., Shouse, D., Neuroth, C., Batelle, R., Lynch, A., Balu, S., Zelina, J., Erdman, T., Burrus, D., Howard, R., Briones, A., Richardson, D., and Caswell, A. "Experimental and Computational Studies of an Ultra Compact Combustor." ASME Turbo Expo, GT2013-94372, San Antonio, TX, June 3-7, 2013.

17. Parks, A.K., "Desensitizing Flame Structure and Exhaust Emissions to Flow Parameters in an Ultra Compact Combustor," Master's Thesis, The Air Force Institute of Technology, WPAFB, OH. 2012.

18. Wilson, J.D., Conrad, M.M., and Polanka, M.D., "Flame Structure Effects at High G-Loading" AIAA-2013-3712, AIAA Joint Propulsion Conference, San Jose, CA, July 14-16, 2013.

19. Saad, M. *Compressible Fluid Flow*. Englewood Cliff, NJ: Prentice-Hall, 1985.

20. Anderson, J. D., *Modern Compressible Flow*, 3rd edition, McGraw-Hill, Inc., New York, New York, 2004.

21. Wilson, J.D., and Polanka, M. D., "Reduction of Rayleigh Losses in a High G-Loaded Ultra Compact Combustor." 58th ASME International Gas Turbine Institute Exposition, GT2013-94795, San Antonio, Texas, USA, June 3-7, 2013.

22. Radtke, T. J., "Efficiency and Pressure Loss Characteristics of an Ultra-Compact Combustor with Bulk Swirl," Graduate School of Engineering and Management, Air Force Institute of Technology, WPAFB, Ohio, Master's thesis, 2007.

23. Johnson, D. D., "Cooling Requirements for the Ultra-Compact Combustor," Graduate School of Engineering and Management, Air Force Institute of Technology (AU), WPAFB, Ohio, Master's thesis, 2012.

24. Society of Automotive Engineers. "Procedure *for the Analysis and Evaluation of Gaseous Emissions from Aircraft Engines"*. Aerospace Recommended Practice 1553 A. 2004.

25. Jermakian, V., McDonell, V.G., and Samuelsen, G.S. "*Experimental Study of the Effects of Elevated Pressure and Temperature on Jet Mixing and Emissions in an RQL Combustor for Stable, Efficient and Low Emissions Gas Turbine Applications*" Public Interest Energy Research (PIER) Program. Irvine, CA: 2012.

26. Turns, S. R., *An Introduction to Combustion*, 3rd edition, McGraw-Hill, Inc., New York, 1996.

27. Sturgess, G.J., Zelina, J., Shouse, D.T., and Roquemore, W., "Emissions Reduction Technologies for Military Gas Turbine Engines." *Journal of Propulsion and Power*. 21.2 (2005). Print.

28. Anderson, W., Radtke, J., King, P.I., Thornburg, H., Zelina, J., and Sekar, B., "Effects of Main Swirl Direction on High-g Combustion," *44th AIAA/ASME/SAE/ASEE Joint Propulsion Conference and Exhibit*, Hartford, Connecticut, AIAA-2008-4954, 2008.

29. Zelina, J., Shouse, D. T., Stutrud, J. S., Sturgess, G. J., Roquemore, W. M., "Exploration of Compact Combustors for Reheat Cycle Aero Engine Applications", ASME, 2006, GT2006-90179.

30. Barringer, M.D., Thole, K.A., and Polanka, M.D., "Experimental Evaluation of an Inlet Profile Generator for High Pressure Turbine Tests", Journal of Turbomachinery, Vol. 129, April 2007, pg. 382-393.

31. Samuelsen, S. *CONVENTIONAL TYPE COMBUSTION*. The Gas Turbine Handbook, U.S. Department of Energy, Office of Fossil Energy, National Energy Technology Laboratory, DOE/NETL-2006-1230. 2006.

32. Barringer, M.D., K.A. Thole, and M.D. Polanka. "Effects of Combustor Exit Profiles on High Pressure Turbine Vane Aerodynamics and Heat Transfer", ASME, 2006, GT2006-90277.

33. Barringer, M.D., K.A. Thole, and M.D. Polanka. "Developing a Combustor Simulator for Investigating High Pressure Turbine Aerodynamics and Heat Transfer", ASME, 2004, GT2004-53613

34. Barringer, M.D., K.A. Thole, and M.D. Polanka. "An Experimental Study of Combustor Exit Profile Shapes on Endwall Heat Transfer in High Pressure Turbine Vanes", ASME, 2007, GT2007.
.
35. Mawid, M.A., H. Thornburg, B. Sekar , and J. Zelina. "Performance of an Inter-Turbine Burner (ITB) Concept with Three-Different Vane Cavity Shapes." 42nd AIAA/ASME/SAE/ASEE Joint Propulsion Conference, July, 2006.

36. National Instruments LabVIEW graphical programming code. National Instruments 2012.

37. Personal communications with Dale Shouse, AFRL/RQTC, 2013.

38. Conrad, M. M., "Integration of an Inter-Turbine Burner to a Jet Turbine Engine," Graduate School of Engineering and Management, Air Force Institute of Technology (AU), WPAFB, Ohio, Master's thesis, 2013.

39. Personal communications with Ron Britton, AFRL/RQTC, 2013.

40. Personal communications with Craig Neuroth, AFRL/RQTC, 2013.

41. Moffat, R. J., "Contributions to the Theory of Single-Sample Uncertainty Analysis," Journal of Fluids Engineering, vol. 104, 1982.

42. Reaction Design, "CHEMKIN-PRO", San Diego, CA, 2010, www. reactiondesign.com

<table>
<tr><td colspan="3" align="center">REPORT DOCUMENTATION PAGE</td><td><i>Form Approved</i>
<i>OMB No. 074-0188</i></td></tr>
</table>

REPORT DOCUMENTATION PAGE	*Form Approved* *OMB No. 074-0188*

The public reporting burden for this collection of information is estimated to average 1 hour per response, including the time for reviewing instructions, searching existing data sources, gathering and maintaining the data needed, and completing and reviewing the collection of information. Send comments regarding this burden estimate or any other aspect of the collection of information, including suggestions for reducing this burden to Department of Defense, Washington Headquarters Services, Directorate for Information Operations and Reports (0704-0188), 1215 Jefferson Davis Highway, Suite 1204, Arlington, VA 22202-4302. Respondents should be aware that notwithstanding any other provision of law, no person shall be subject to an penalty for failing to comply with a collection of information if it does not display a currently valid OMB control number.
PLEASE DO NOT RETURN YOUR FORM TO THE ABOVE ADDRESS.

1. REPORT DATE *(DD-MM-YYYY)* 27-03-2014	2. REPORT TYPE Master's Thesis	3. DATES COVERED *(From – To)* Oct 2012 – Mar 2014

TITLE AND SUBTITLE Operational Characteristics of an Ultra Compact Combustor	5a. CONTRACT NUMBER
	5b. GRANT NUMBER
	5c. PROGRAM ELEMENT NUMBER
6. AUTHOR(S) Damele, Christopher J., Captain, USAF	5d. PROJECT NUMBER
	5e. TASK NUMBER
	5f. WORK UNIT NUMBER

7. PERFORMING ORGANIZATION NAMES(S) AND ADDRESS(S) Air Force Institute of Technology Graduate School of Engineering and Management (AFIT/ENY) 2950 Hobson Way, Building 640 WPAFB OH 45433-8865	8. PERFORMING ORGANIZATION REPORT NUMBER AFIT-ENY-14-M-13
9. SPONSORING/MONITORING AGENCY NAME(S) AND ADDRESS(ES) Air Force Office of Scientific Research Dr. Chipping Li 875 N Randolph St Suite 325 Rm 3112 Arlington AFB, VA 22203 chipping.li@us.af.mil	10. SPONSOR/MONITOR'S ACRONYM(S) AFOSR
	11. SPONSOR/MONITOR'S REPORT NUMBER(S)

12. DISTRIBUTION/AVAILABILITY STATEMENT
   DISTRUBTION STATEMENT A. APPROVED FOR PUBLIC RELEASE; DISTRIBUTION UNLIMITED.

13. SUPPLEMENTARY NOTES
This material is declared a work of the U.S. Government and is not subject to copyright protection in the United States.

14. ABSTRACT
Ultra Compact Combustors offer unique solutions to minimize engine size and weight. They accomplish this by reducing the number of components in the engine core and perform the combustion in a circumferential cavity that encircles the core flow. Within this cavity, the fuel is injected rich. Burning continues to occur in the vane passage beneath the circumferential cavity which must be completed in a controlled manner prior to the inlet plane of the turbine rotor. Furthermore, the temperature distribution at the exit of the vane passage must be controlled to generate high work extraction from the turbine. The primary metrics for comparison are the exit temperature and pressure profiles, the emissions characteristics, and the overall system losses.

15. SUBJECT TERMS
   Combustion / Ultra Compact Combustor

16. SECURITY CLASSIFICATION OF:			17. LIMITATION OF ABSTRACT	18. NUMBER OF PAGES	19a. NAME OF RESPONSIBLE PERSON Marc Polanka, AFIT/ENY
a. REPORT U	b. ABSTRACT U	c. THIS PAGE U	UU	169	19b. TELEPHONE NUMBER *(Include area code)* (937) 255-3636, ext 4714 (marc.polanka@afit.edu)

Standard Form 298 (Rev. 8-98)
Prescribed by ANSI Std. Z39-18